Understanding the characteristics of carbides located at grain boundary in crack free Ni-based superalloys fabricated by laser powder bed fusion.

Rafael Mata Garcia

Department of Mining and Materials Engineering

McGill University, Montreal

May 2023

A thesis submitted to McGill University in partial fulfillment of the requirements of the degree of Master of Science

© Rafael Mata Garcia 2023

All Rights Reserved

Abstract

Laser Powder Bed Fusion (LPBF) technology holds great promise as a manufacturing process for printing nickel-based superalloys, thanks to its numerous advantages over traditional methods. These include the availability of novel materials, the ability to create complex and near-to-shape 3D geometries, shortened development and production lead times, and the ability to tailor microstructure. However, current limitations are being intensively studied to ensure that the printed parts can be utilized with complete confidence in critical applications.

A particular case of interest is Hastelloy X (HX), a Ni-based superalloy with excellent oxidation resistance and high-temperature mechanical properties. HX is also known to be non-weldable. The strength of this alloy comes mainly from the additions of solid solution elements and carbides. Mo-rich carbides in their metastable M_6C form and located at grain boundaries (GB) have been identified as a precursor to cracking when HX is additively fabricated.

Despite these challenges, researchers from the Laboratory of Powder Processing and Additive Manufacturing of Advanced Materials ($P^2[AM]^2$) have successfully printed crack-free HX samples via LPBF using a commercially available HX powder.

Using Backscattered Electrons (BSE) and Energy-dispersive X-ray spectroscopy (EDS) techniques, we analyzed crack-free HX samples to gain new insights into the influence of crystal orientation and grain boundary character on the behavior of segregation and precipitation.

Our findings indicate that Cr and Mo preferentially segregate towards the 〈1 0 0〉 directions. We confirmed that the kinetic acceleration of carbides occurs when they appear at angles with a misorientation greater than 5°. Furthermore, we examined the characteristics of carbides and their interactions with the matrix.

These discoveries shed light on the material-process-microstructure-properties paradigm and the potential of the LPBF to control crystal texture and GB character.

.

Résumé

La technologie de fusion laser sélective d'un lit de poudre (LPBF, pour ses sigles en anglais) est très prometteuse en tant que processus de fabrication pour l'impression de superalliages à base de nickel, grâce aux nombreux avantages qu'elle offre par rapport aux méthodes traditionnelles. Ceux-ci comprennent la disponibilité de nouveaux matériaux, la capacité de créer des géométries 3D complexes et proches de la forme, la réduction des délais de développement et de production, et la possibilité d'adapter la microstructure. Toutefois, les limites actuelles font l'objet d'études approfondies afin de garantir que les pièces imprimées puissent être utilisées en toute confiance dans des applications critiques.

L'Hastelloy X (HX), un superalliage à base de nickel doté d'une excellente résistance à l'oxydation et de propriétés mécaniques à haute température, est un cas particulièrement intéressant. Le HX est également connu pour être non soudable. La résistance de cet alliage provient principalement de l'ajout d'éléments en solution solide et de carbures. Les carbures riches en magnésium sous leur forme métastable M_6C et situés aux joints de grains (GB, pour ses sigles en anglais) ont été identifiés comme précurseurs de fissures lors de la fabrication additive du HX.

Malgré ces difficultés, des chercheurs du Laboratoire de traitement des poudres et de fabrication additive de matériaux avancés ($P^2[AM]^2$) ont réussi à imprimer des échantillons de HX sans fissures par LPBF en utilisant une poudre de HX disponible dans le commerce.

En utilisant des électrons rétrodiffusés (BSE, pour ses sigles en anglais) et des techniques de spectroscopie de rayons X à dispersion d'énergie (EDS, pour ses sigles en anglais), nous avons analysé des échantillons de HX sans fissures afin de mieux comprendre l'influence de l'orientation cristalline et des caractéristiques des joints de grains sur le comportement de la ségrégation et de la précipitation.

Nos résultats indiquent que le Cr et le Mo ségrègent préférentiellement vers la direction 〈1 0 0〉. Nous avons confirmé que l'accélération cinétique des carbures se produit lorsqu'ils apparaissent à des angles dont la désorientation est supérieure à 5°. De plus, nous avons examiné les caractéristiques des carbures et leurs interactions avec la matrice.

Ces découvertes mettent en lumière le paradigme matériau-processus-microstructure-propriétés et le potentiel du LPBF pour contrôler la texture cristalline et le caractère GB.

Acknowledgments

I am deeply indebted to my supervisor Prof. Mathieu Brochu Ph.D., and my co-supervisor Prof. Raynald Gauvin Ph. D. Firstly, for allowing me to be a part of one of the most renowned research groups in Materials Engineering and Characterization worldwide. Additionally, I sincerely appreciate their support, patience, guidance, and trust during my study process. Their mentorship helped me grow as a researcher and as an individual.

Words are not enough to express my gratitude to my family -Judith, Khalil, and Victoria. They not only believed in me, but also took the courageous step of embarking on an uncertain journey, leaving a part of their own lives behind, all to support me in this process. We accomplished this together.

I am immensely grateful to the exceptional team of the Laboratory of Powder Processing and Additive Manufacturing of Advanced Materials ($P^2[AM]^2$), who have always been willing to lend their support, not just in academic matters. I extend my heartfelt thanks to each and every one of them: Amit, An, Anne, Anubhav, Corina, Edem (RIP), Eileen, Guohong, Ivonne, Jaskaranpal, Mahmoud, Mohamad, Murali, Omar, Pablo, Pierre, Qi, Satish, Shipei, Srikanta, and Tejas. I want to give a special mention to Ashutosh, and Oscar who played a fundamental role in my project.

I would also like to express my special thanks to Nicolas Brodusch, Ph. D., for helping me scan samples in EBSD and ECCI techniques and for the fruitful discussions to increase my understanding of electron microscopy.

I am grateful to the Ávila Cerda family, who believed in my academic project and supported me in obtaining financing and scholarships.

Acknowledgment is given to McGill University and the Materials and Mining Engineering department for their funding.

Por último, pero no por ello menos importante, agradezco enormemente a mis padres Rafael Mata Torres y María Victoría García Gomez por su apoyo incondicional y esfuerzo en formarme. A mis hermanos José Ramón, María Guadalupe, Víctor Manuel, Claudia Alejandra y Ana Catalina, así como a sus respectivas familias. Solo quiero que sepan que siempre los tuve en mis pensamientos durante todo este proceso.

Table of Contents

List of Figures

List of Tables

Abbreviations

ΔT	Equilibrium freezing range
AB	As-built
AES	Auger electron spectroscopy
AM	Additive manufacturing
AP	Atom probe
BD	Building direction
BSE	Backscattered electrons
BSE-COMP	Backscattered electrons compositional
CCD	Charge-coupled device
cECCI	ECCI under controlled diffraction conditions
CET	Columnar-to-equiaxed transformation
C_L	Liquid composition during solidification
CS	Constitutional supercooling
C_S	Solid composition during solidification
DED	Directed energy deposition
D_L	Liquid diffusion coefficient
EBSD	Electron backscattered diffraction
ECCI	Electron channeling contrast imaging
ECP	Electron channeling patterns
ED	Energy density
EDS	Energy-dispersive X-ray spectrometry
FCC	Face-centered cubic
FE-SEM	Field emission scanning electron microscope.
FET	Field effect transistor
G	Temperature gradient
GB	Grain boundary
GBCD	Grain boundary character distribution
GBE	Grain boundary engineering
GBE	Grain boundary engineering
HAADF	High-angle annular dark-field.
HAGB	High angle grain boundaries
HIP	Hot isostatic pressing
HR-TEM	High-resolution transmission electron microscope.

HT	Heat treatment
HX	Hastelloy X
HX-LPBF	Hastelloy X manufactured by laser powder bed fusion
IQ_E	Image quality map average Hough transform intensity peaks
IQ_{HT}	Image quality map entropy
IQ_M	Image quality map intensity mean
IQ_σ	Image quality map intensity deviation
k	Segregation coefficient
KPC	Kikuchi patterns
LAGB	Low angle grain boundaries
LPBF	Laser powder bed fusion
OIM	Orientation imaging microscopy
OR	Orientation relationship
PBF	Powder bed fusion
PD-BSE	Photodiode backscattered electrons
PF	Polar figure
PS	Precipitation strengthened
R	Solidification growth
r^*	Nucleation critical radius
RGB	Random grain boundary
S/L	Solid – Liquid interface
SAED	Selected-area electron diffraction
SDD	Silicon drift detector
SEDP	Selected area electron diffraction pattern
SEM	Scanning electron microscope
SLM	Selective laser melting
SSS	Solid-solution strengthened
ST	Solution-treated
S-TEM	Scanning transmission electron microscope
TEM	Transmission electron microscopy
TMP	Thermal mechanical processing
TSR	Thermal shock resistance
WQ	Water quenching
XCF	Cross-correlation function
XRD	X-ray diffraction
γ_0	Grain boundary energy
Γ_A	Excess energy amount of grain A at the boundary

Chapter 1 Introduction

1.1 Background

With the advent of additive manufacturing (AM) as a reliable process for manufacturing metal alloy components, we must reassess our understanding of microstructure and microtexture. This is because of differences in conditions during melting and solidification cycles, which translates into variations at all scales of the hierarchical structure. Compared to their conventional manufacturing processes counterparts, crystallographic texture, cellular structure, and grain configuration exhibit significant variations. These variations grant additively manufactured parts unique characteristics and properties, as well as flaws that must be understood to gain complete control during metal deposition.

This approach is exemplified in the fabrication of superalloys. The growing demand for these materials creates new opportunities to expand AM to more critical aerospace, chemical, and nuclear power applications, among others [33]. Metal AM offers fundamental advantages for these kinds of applications, including access to novel materials that can only be processed using AM, reduced costs for tooling, minimized material waste, shorter development and production lead times, and highly efficient and lightweight design solutions. [26]. But one of the most outstanding possibilities the AM provides is to tailor the microstructure architecture, which is achieved with less effort than traditional manufacturing processes.

Ni-based superalloy parts have been successfully printed via several routes within the spectrum of additive manufacturing processes, including directed energy deposition (DED) and powder bed fusion (PBF), both allowing the fabrication of metal components with near full density. However, during AM manufacturing, some superalloys are highly prone to cracking.

Hastelloy X (HX) is a nickel-chromium-iron-molybdenum alloy. It has gained significant attention from materials scientists and engineers due to its exceptional resistance to creep and oxidation at high temperatures. In addition, HX possesses superior fabricability, which not all Ni-based superalloys share [34].

One of the critical characteristics of HX is that its strength is primarily achieved by adding solid solution elements and forming carbides [35]. Carbides are well-known to play a significant role in the properties of alloys, affecting characteristics such as hardening [36], yield strength [37], anisotropy, oxidation resistance [38], and creep, among others.

However, when HX is manufactured through laser powder bed fusion (HX-LPBF), the presence of carbides located at GBs has been found to have a detrimental effect, resulting in the formation of cracks in samples in the as-built (AB) condition. This fracture propensity has also been reported in casting and welding processes, as well as in various alloys such as SS 316 [39], Aluminum, Titanium [40], and other Ni-based superalloys [41-43].

Despite extensive theoretical literature on GB segregation and precipitation, the emergence of new manufacturing technologies poses fresh challenges in comprehending the formation and evolution of GBs, as well as the interplay between GB segregation and carbide formation. Understanding these phenomena is crucial as they greatly influence the mechanical properties of solidified systems.

Various strategies have been implemented to mitigate cracking in HX-LPBF. These include altering the chemical composition of the raw material [44], preheating the baseplate [39, 45], and with secondary processes such as heat treatments (HT) or hot isostatic pressing (HIP) [46, 47], among others. However, it is important to note that these solutions incur additional costs, may only be applicable to certain materials, and do not ensure long-term part integrity due to carbide evolution. Hence, a thorough comprehension of these phenomena is imperative.

AM offers an additional approach to prevent cracking by allowing for the customization of the microstructure and microtexture during the manufacturing process. Ongoing research worldwide is devoted to improving the quality of the deposited metal by manipulating the input parameters of the LPBF process [40, 48-53]. To take full advantage of this resource, a detailed understanding of the physical metallurgy of the alloy being used is essential.

In this order of ideas, the members of the Laboratory of Powder Processing and Additive Manufacturing of Advanced Materials $P^2[AM]^2$ of McGill University were able to print crack-free Hastelloy X through laser powder bed fusion (HX-LPBF), considered non-weldable and using standard commercial HX powder. The characteristics and properties of these results have been reported elsewhere [42, 54]. It is possible to complement the work carried out by the $P^2[AM]^2$ team, analyzing the carbides at the GB and elaborating on why they are not acting as the cracking source.

Electron Backscattered (BSE) techniques and Energy-dispersive X-ray Spectrometry (EDS) are commonly used to characterize carbides and have shown promise in furthering our understanding of these microstructural features. These techniques are typically performed

using scanning electron microscopy (SEM). The SEM is a powerful tool that helps researchers characterize qualitatively and quantitatively phenomena that occur at reduced scales far beyond the capabilities of the naked eye. At the macroscale level, the spatial location and organization of the microstructure are deeply linked with the response of the material to the environment and external stimuli.

The versatility of the SEM derives from the variety of signals that it is possible to obtain and question from the electron beam-specimen interaction, by adding or changing detectors and setting parameters as required, all in a single workstation [55-57]. The latter, thanks to improvements in the SE microscope capabilities [58, 59] and the incorporation of modern software to index the signals accurately obtained [47].

1.2 Research Objectives

An aspect that has yet to be fully explored in terms of image characterization in Ni-based alloys manufactured by LPBF, is the spatial location, microstructural assessment, texture recognition, and elemental composition of the carbides located along and within the GBs. The use of SEM poses several challenges, starting with the fact that in LPBF pieces, there is a refinement in the size of the entire hierarchical structure including, precipitates [35], so higher resolution, therefore brighter filaments are required.

Besides, due to the nature of GBs related to the energy of the defects and the limits of the structures, the diffracted electrons contain signals from different orientations of the crystal lattice [60], which could lead to misinterpretations or hide particles of interest in the micrograph, especially those with a sub-micron size. To overcome these drawbacks, the electron channeling contrast image (ECCI) and backscattered electron diffraction (EBSD) were used to complement each other in terms of imaging descriptors, as well as EDS, to gain a qualitative insight into the chemical composition distribution, particularly along the GBs.

The motivation behind this research is to gain a better understanding of the carbides located at GBs, with an emphasis on Cr-rich and Mo-rich carbides, the latter identified as a precursor of cracking in HX-LPBF. The selected characterization techniques aim to achieve the following objectives:

1. Characterize the morphology, distribution, and density, of the carbides and GBs.
2. Qualitatively analyze the elemental distribution along GBs.
3. Correlate the information from the previous points with any preferential aspect for the carbides to nucleate and grow.

Chapter 2 Literature Review.

This work covers fundamental aspects that will allow the reader to acquire general knowledge about what is known so far in the characteristics of carbides located at GB in Ni-based superalloys. To make this text more digestible, it is divided into four sub-sections: (Section 2.1) Additive Manufacturing (AM); (Section 2.2) Nickel-based superalloys; (Section 2.3) Hastelloy X; (Section 2.4) Scanning Electron Microscope (SEM) based techniques principles and theory; and a final (Section 2.5) Summary.

2.1 Additive Manufacturing (AM)

Recently, AM processes have gained significant attention and adoption. The advantages of AM over traditional manufacturing processes have been widely discussed in numerous scientific articles. These advantages include the availability of novel materials that can only be used with AM, a tool-free digital approach to manufacturing, the ability to create complex and near-to-shape 3D geometries, shortened development and production lead times, highly efficient and lightweight design solutions, the ability to produce low volumes, and mass personalization, to name a few of the most relevant benefits [26, 61].

The definition of AM given by ISO/ASTM 5900:2021 [62] is the "*process of joining materials to make parts from 3D model data, usually layer upon layer, as opposed to subtractive manufacturing and formative manufacturing methodologies*" There are several processing routes in the AM spectrum. Still, they all have in common the local binding or melting of raw material (powder layer, wire, rod, or metal strip) in consecutive layers [61, 63].

Two AM processes have seen rapid adoption for the fabrication of Ni-based superalloys, these are the powder bed fusion (PBF) and directed energy deposition (DED) processes [35]. Despite the significant progress that has been made, there are still some critical gaps that must be addressed before AM can be considered a completely reliable process for producing components with consistently high quality.

PBF can produce parts with better part complexity, precision, and surface polish than DED, so it is an excellent candidate to move its use for more critical applications such as aerospace, medical, and nuclear power energy industries.

Within PBF processes, two sub-division are based on the heat source[1] laser (LPBF) and electron (EPBF). The cooling rates, besides the heat source, are the main difference between these two processes. The LPBF experiences cooling rates about two orders greater than EPBF, and it has been observed that the LPBF method has more control over the microstructure [65].

2.1.1 Laser Powder Bed Fusion Process (LPBF)

The Laser Powder Bed Fusion (LPBF) is widely used for rapid prototyping due to its ability to fabricate reliable and dense parts, even with superior mechanical characteristics to their wrought counterparts. This technology is used for research activity in several materials, including steels, nickel-based alloys, titanium-based alloys, and metal-matrix composites [35, 66].

The routine is as follows: a layer of metallic feedstock (already mixed with alloying, additives, seeds, etc.) is spread on the build plate, and a roller or a wiper blade distributes a uniform layer of powder on the surface. Then, the heat source selectively melts or sinters the dropped powder. Once a cycle of a layer is completed, the build table is lowered, and the powder table rises so the powder can be deposited on the preceding layer. This procedure is repeated layer after layer until the 3D piece is built [18, 35, 66, 67].

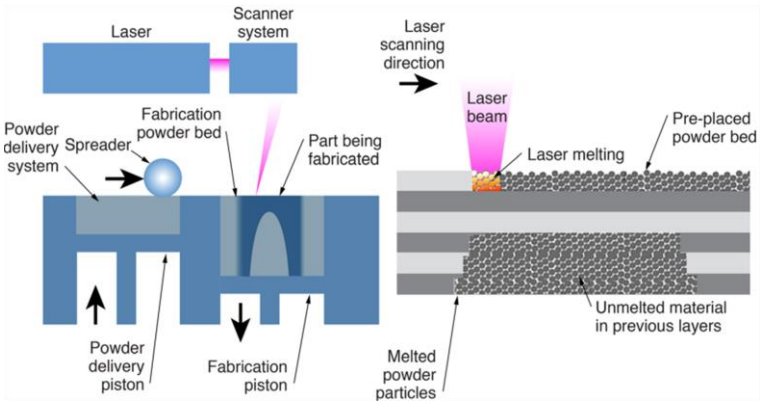

Figure 2.1. Schematic overview of the select laser melt process both at the machine and powder scales [18].

2.1.2 Texture evolution during solidification

The AM solidification processes are like casting solidification in aspects such as the driving forces and tracking metrics. However, due to the speed at which events happen during

[1] This classification is not widely adopted, and the categories could even be in function of heat source, with sub-categories based on the feedstock [64] T. DebRoy *et al.*, "Additive manufacturing of metallic components – Process, structure and properties," *Progress in Materials Science*, vol. 92, pp. 112-224, 2018/03/01/ 2018, doi: https://doi.org/10.1016/j.pmatsci.2017.10.001.

AM processes, linked to continuous and repetitive thermal cycles inherent to the process itself, sharp differences are evident in metal solidification behavior, thus microstructure and properties of products.

Starting with the fundamentals of solidification in casting and welding is useful. S*olidification* begins when the temperature of the interface solid-liquid is lowered just below the equilibrium freezing temperature [68], and this beginning may be broken down into two distinct stages, nucleation, and growth.

Nucleation is the process of forming and consolidating tiny particles, known as nuclei. Suppose these particles reach a critical state, on the function of temperature and radius (assuming a spherical form, but this approach can be applied to several shapes), then the particle or embryo will continue its growth absorbing atoms until it reaches a crystalline structure and only is delimited by other particles. If the nuclei do not reach a critical state, they will disintegrate and re-melt.

When the temperature at the solid-liquid interface is slightly below the real freezing temperature, more atoms will join to form the solid particles than atoms leaving the liquid side, which is the moment when *growth* occurs [68]. This step begins once a critical size (r^*) has been reached, and the particle becomes a stable nucleus.

Hereafter, the focus is on the *solid-liquid (S/L) interface* and its morphological evolution during solidification, particularly on the dendritic microstructure. The morphology of the S/L interface is given by several events that may or may not produce instabilities and propitiate the growth of a specific morphology and crystallographic direction. With the aid of casting and welding solidification knowledge, it is possible to enumerate many phenomena at the S/L interface involved in its evolution.

Nucleus growth is limited by (1) the kinetics of atom attachment to the interface, (2) capillarity, and (3) diffusion of heat and mass. These factors have different predominance depending on the chemical composition and solidification conditions. Solidification growth morphology can be divided into faceted, typical of non-metal and intermetallic materials, and non-faceted, mainly present in metals. During the solidification of a non-faceted material, such as metal, atoms can be added easily to any surface point. The crystal shape is dictated mainly by the form of the heat and solute diffusion fields. Non-faceted growth reflects the independence of the atomic attachment kinetics with respect to the crystal plane involved [69].

Nevertheless, a remaining slight anisotropy in properties such as the interface energy and atomic attachment kinetics leads to the appearance of dendrite arms along with specific crystallographic directions. When formed from a solution or vapor, a material that produces non-faceted crystals can produce faceted crystals.

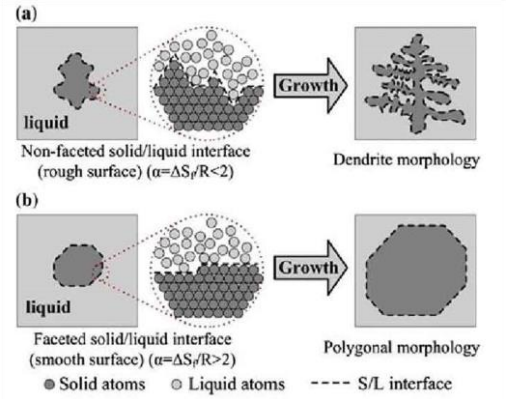

Figure 2.2 The interfacial form between liquid and solid: (a) Non-faceted growth; (b) Faceted growth [9].

Solute redistribution plays a crucial role in the solidification process as it influences various aspects such as grain length scale, morphologies, phase distribution, and microsegregation [70]. For instance, the process of diffusion can significantly impact the solute balance within the alloy, depending on whether it occurs during the solid or liquid phase. [71]. Furthermore, during undercooling events, the redistribution of solutes noticeably affects the shape of the dendrite tips, resulting in varying degrees of microsegregation along the entire dendrite structure. [72]. The solute distribution is dependent on thermodynamic and kinetic parameters, highlighting the complex interplay between these factors. During the solidification of metallic alloys, solute redistribution appears when there are differences in solubility in liquid and solid phases. This redistribution is influenced by factors such as the composition content percentage and temperature at a constant pressure. [73].

In a solidified body, these gradients in chemical and phase compositions are evident on the first solid germs (the dendrite core) and the last drops of liquid (interdendritic regions) [19, 73, 74]. Depending on the material and final application, the effects of this redistribution, such as enrichment of certain alloys in the intercellular regions, precipitates, and refinement of morphology and size of microstructures, can have a beneficial or a detrimental influence on the final properties.

In practice, metal alloys rarely solidify with a flat liquid-solid interface. The interface is usually bumpy or treelike. These interfaces, along with the flat interface, present a non-

uniform in composition in solidified metal alloys, which also leads to microsegregation [30, 75-79].

The events that are part of this phenomenon are better understood when plotted in a phase diagram. Suppose an ideal transformation phase diagram, where the solid and liquid equilibrium is maintained at the solid-liquid (S/L) interface throughout solidification. The composition of C_S and C_L follows the slope at any temperature T. In that case, we can define the *equilibrium segregation coefficient*, k as follows:

$$k = \frac{C_S}{C_L}$$

Equation 2-1

C_S and C_L are the solid and liquid compositions at the *S/L* interface, respectively. Segregation coefficient is assumed constant, that provides a good approximation for many practical applications.

Basically, the phase diagram tells us how much solute can be placed in each phase (S, S+L, L). Figure 2.3 shows two different situations (a) if $k < 1$, C_S and C_L both increase as temperature T of the *S/L* interface drops during solidification, (b) for $k > 1$, C_S and C_L both decrease as temperature T of the *S/L* interface drops during solidification.

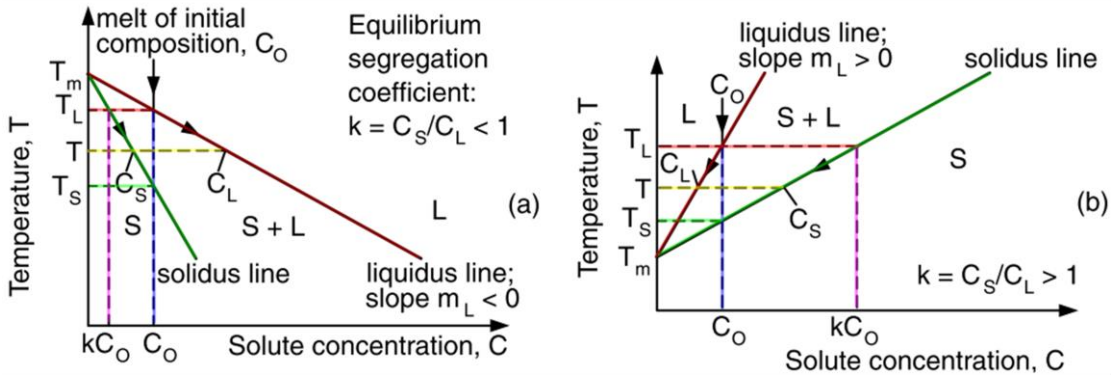

*Figure 2.3. The phase diagram shows the behavior of the equilibrium partition ratio **k** in an ideal binary phase diagram [19].*

Constitutional supercooling: Microstructures formed during solidification are divided into four basic types, namely planar, cellular, columnar dendritic, or equiaxed dendritic. The formation of these structures is closely related to the changes in constitutional supercooling (CS). That, in simple terms, is the process of lowering the temperature of the melt below its freezing point just after it becomes a solid. As it increases (temperature decreases), the modes passing from planar to cellular, columnar dendritic, and equiaxed-dendritic.

The conditions necessary to define the morphology of the interface can be estimated from the following inequality. This expression is defined to promote planar coupled growth.

$$\frac{G}{R} \geq \frac{\Delta T}{D_L}$$

Equation 2-2

where G is the liquid temperature gradient, R is the interface speed or solidification growth rate, ΔT is the equilibrium freezing range of the alloy in K [temperature difference between liquidus and solidus for the original alloy composition (T_L-T_S)], and D_L is the liquid diffusion coefficient [19, 78] Figure 2.4.

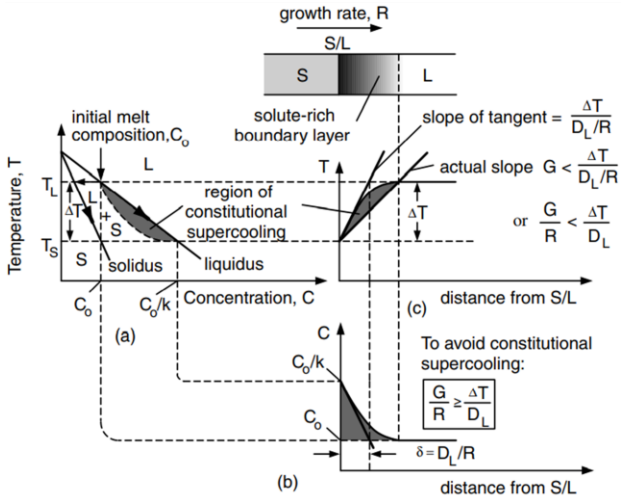

Figure 2.4 Constitutional supercooling: (a) phase diagram; (b) composition profile in liquid; (c) liquidus temperature profile in liquid [19].

When constitutional supercooling is present, the interface between the liquid and solid takes on cellular or dendritic morphology. For conditions of growth where the ratio G/R is only slightly smaller than the ratio $\Delta T/D_L$, the interface is cellular. For conditions of growth where the ratio G/R is much smaller than the ratio $\Delta T/D_L$, the interface becomes treelike or dendritic [19, 78].

2.1.3 Texture evolution in additive manufacturing

S. Suwas and R. J. Vikram [12] studied the texture evolution in metallic materials during AM processes and tried to extract generalities from PBF and DED processes. However, each discovery must be dealt exclusively with the process parameters and family of alloys for which the research was carried out.

As mentioned above, temperature gradient (G) and solidification growth rate (R) are the main indicators for modeling and tracking, microstructure, and texture. The ratio of (G/R) determines the solidification mode (morphology of the solidification microstructure [30]), and

the product ($G \times R$) is the scale of solidification (cooling rate $\dot{T}$ [30], thus the size of the microstructure). The physical representation of G and R metrics in the AM process is the melt pool, and the input parameters of the system, such as scanning speed, beam power, particle size distribution, powder layer thickness, and the overlapped distance between laser raster (hatch distance) [66] influence the melt pool dynamics solidification (R) and cooling rate (G).

Usually, the parameters described above are encompassed in a single metric called energy density (ED) [J/mm^3] [30, 80, 81]. It is typically used to determine the energy threshold beyond which the material achieves almost full consolidation, but just in a semi-quantitative manner.

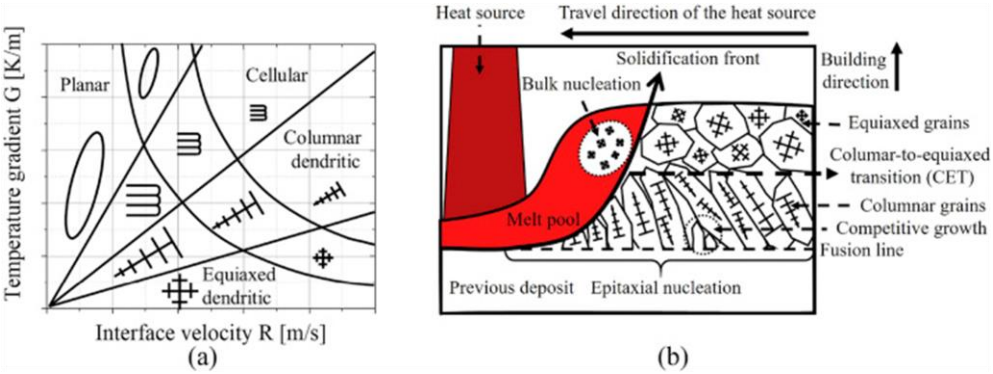

Figure 2.5. (a) Effect of temperature gradient G and growth rate R on the morphology and size of solidification microstructure; (b) Summary of possible nucleation and growth mechanisms and their effects on the grain structure [27].

By varying ED is possible to shape the growth direction and grain morphology (Figure 2.5), therefore, in theory, it is feasible to produce almost any desired microstructure i.e., planar, cellular, columnar dendritic, or equiaxed dendritic. The melt pool boundary mainly influences the structure of the base metal during solidification. Competitive growth dominates the microstructure as one moves farther away from the melt pool, and this is mainly regulated by cooling rates [82]. Competitive growth is the other condition in the structure morphology and crystallographic direction formation. In FCC structures, cellular/dendritic structures tend to grow preferentially along the ⟨0 0 1⟩ direction due to the lowest atomic planar density of the {0 0 1} plane [69, 83]. This means that during growth, atoms are more likely to deposit on this plane, resulting in faster solidification along the ⟨0 0 1⟩ || BD direction compared to other crystallographic directions. Grains exhibiting this texture can effectively hinder the growth of grains aligned with less favorable heat flux directions. [84, 85].

For LPBF processes, the columnar grain aligned to the building direction is the most reported solidified microstructure, this is derived from the dissipation of heat flux from the top of the material towards the building platform [86].

The final lattice orientation is mainly determined by the size and shape of the melt pool and the scanning strategy. The intensity and scanning speed of the beam defines melt pool geometry, depending on the intensity of the laser source the melt pool can have an oval, tear-dropped, or semicircular shape. The scanning strategy correlates to the easy growth and maximum heat flow directions, Figure 2.6 shows the results over texture by using two different scanning strategies.

As mentioned, for a FCC structure in the PBF process, the grain growth aligns with ⟨1 0 0⟩ in the build direction (BD), again, determined by the local curvature of the melt pool boundary. If the pool has a high length-to-depth ratio, grains will take vertical orientation, solidification will occur at the melt pool boundary, and competitive growth will dominate away from the high-temperature concentration. What is important to highlight is the heat flow direction, owing to the dendrites aligning themselves closely with the maximum heat flow direction at the solid-liquid interface Figure 2.5(b).

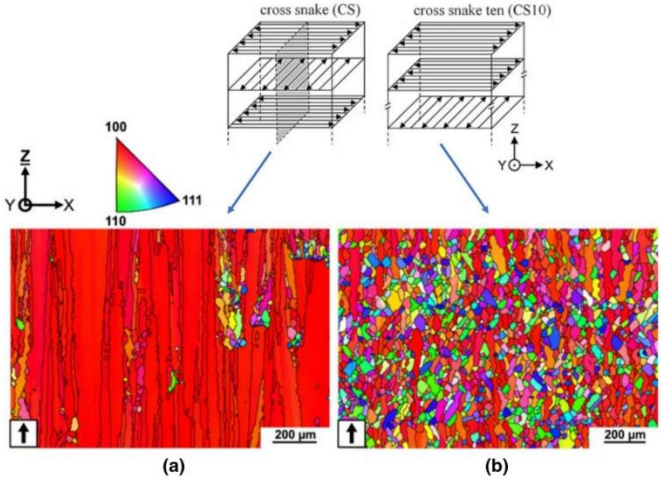

Figure 2.6 EBSD grain orientation maps (a) columnar grains— strong texture, (b) equiaxed grains—random texture upon changing the scan strategy [12]

Among the final properties that can be affected by the texture on pieces additively manufactured are g*rain size, anisotropic microstructures, the shape of the grains (columnar, equiaxed), densification, and non-equilibrium microstructures (metastable phases, solute*

trapping, non-equilibrium compositions), residual stresses, metallurgical defects, Young´s Modulus [48, 50, 52, 61, 87].

2.2 Nickel-based superalloys

2.2.1 Superalloys

Superalloys are materials that possess a combination of strength, toughness, creep, and oxidation/corrosion resistance at high temperatures, beyond about 800 °C. Even though various compositions of alloys can be denominated "Superalloys" (iron-nickel, nickel, and cobalt base), the most common and important are those based on Nickel [88, 89].

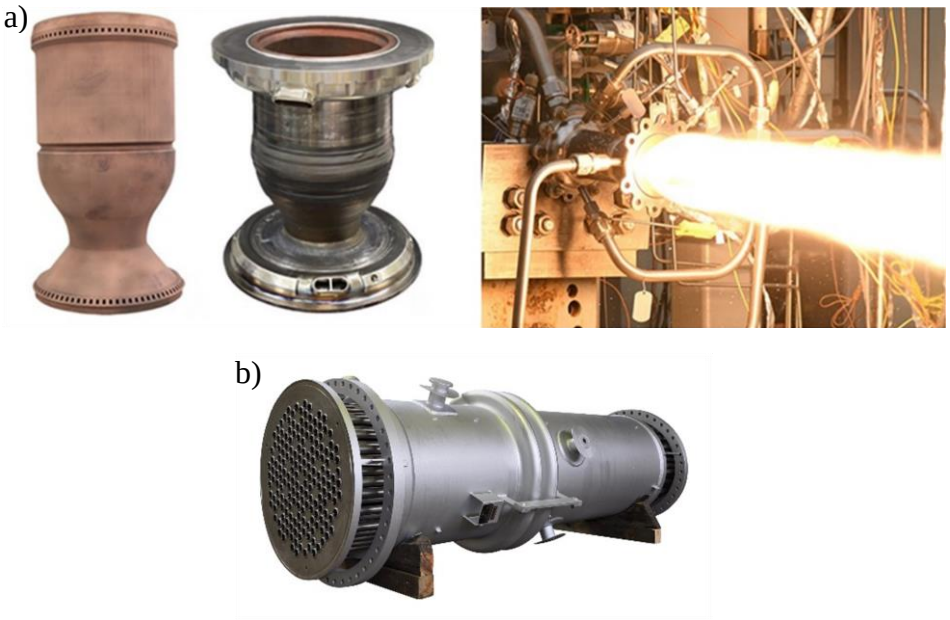

Figure 2.7 a) Fully AM thrust chamber assemblies hot-fire tested at NASA MSFC [26]; b) Heat exchanger made of Hastelloy 2.4605 [32]

The evolution of these alloys was linked to the development of the gas turbine engine (Figure 2.7 *a)*), particularly for components such as combustor cans, exhaust nozzles, and turbine sections, in short, where high-pressure, high-temperature, and harsh environments are combined [90]. Currently, Ni-based alloys can be found in reactors and heat exchangers Figure 2.7 *b)* for the chemical, petrochemical, and nuclear power industries.

Nickel possesses several characteristics that make it an excellent choice for materials requiring resistance to high temperatures and harsh environments. These characteristics include a high melting point, the ability to form alloys, high temperature strength, and resistance to corrosion and oxidation. Starting from its Face Centered Cubic (FCC) structure, which maintains its lattice arrangement the entire range of temperatures up to the melting point [13]. The capability of nickel of dissolving large concentrations of alloying elements is higher

compared to other metals, it also develops a superior corrosion resistance with the addition of Cr and/or Al. These attributes allow it to interact with a wide range of elements to develop alloys for applications where protection from different forms of degradation such as aqueous corrosion, oxidation, and sulfidation is required.

There is no canonical classification for nickel alloys, however, they are generally categorized based on their composition. The two primary classifications are Solid-Solution Strengthened (SSS) alloys and Precipitation Strengthened (PS) alloys, which are considered the most significant divisions. [91].

2.2.2 Physical metallurgy of nickel-base superalloys

For SSS Ni-alloys, elements such as Co, Fe, Cr, Ru, Mo, Rh, and W, (elements with similar atomic radii to Nickel no larger than 15%) are added in a low concentration, they prefer to partition to the primordial austenitic γ phase and thereby stabilize it [92]. By substitution mechanisms, the Ni atoms are replaced at random sites in the lattice arrangement by the alloying elements, these have high melting points which provide the γ matrix with a reduction in atom diffusion and good lattice cohesion at elevated temperatures [93].

With higher concentrations of elements such as Al, Ti Nb, Ta, and V, precipitation of coherent intermetallic secondary γ' and γ'' phases happen and provide the alloy with different properties. This increment in the concentration of the solute makes the alloys arrange themselves in an ordered manner, occupying the corners of the elementary unit cell. This arrangement makes dislocation movement and diffusion harder, allowing different mechanisms for hardening to act.

The γ' - $Ni_3(Ti, Al)$ is an ordered L_{12} structure phase that has a crystallographic mismatching lower than 1% with the γ matrix, and one of its most remarkable effects is the increase of yield strength with increasing temperature up to ~ 800 °C. The γ'' - Ni_3Nb phase can form in alloys with sufficient Nb additions, but this phase is less stable than the γ′ and can cause orthorhombic δ phase after prolonged exposure to elevated temperatures, this phase is associated with embrittlement and loss of ductility [94].

The effects of alloying on Ni-based materials are vast and its study is of great interest to academia and industry. Table 2.1 and Figure 2.8 contains a quick guide to the known effects of each element and how they are present in the solid solution, so far.

Many Ni-based alloys with appreciable carbon levels can form various types of carbides. Carbon is often present at concentrations up to 0.2 wt. %, it combines with reactive

elements such as Ti, Ta, and Hf to form MC carbides, where M stands for a metal atom such as Cr, Mo, Ti, Ta, or Hf [92]. But also B, C, and Zr tend to segregate to GBs of the γ phase, because of their marked difference in their atomic size with nickel, which in turn can promote the appearance of carbides and borides at GBs. [44].

Table 2.1 Summary of the role of alloying elements in Ni-based superalloys [94].

Effect[2]	**Element**
Solid Solution Strengthener	Co, Cr, Fe, Mo, W, Ta
γ′ - Ni_3(Al,Ti) Former	Al, Ti
Solid Solution Strengthening of γ′	Cr, Mo, Ti, Si, Nb
γ″ - Ni_3Nb Former	Nb
Carbide Formers:	
MC and M(C,N)	W, Ta, Ti, Mo, Nb
M_7C_3	Cr
$M_{23}C_6$	Cr, Mo, W
M_6C	Mo, W
TCP Phase (σ, P, μ, Laves)	Ti, V, Zr, Nb, Ta, Al, Si
Surface Oxide (Cr_2O_3/Al_2O_3) Former	Cr, Al

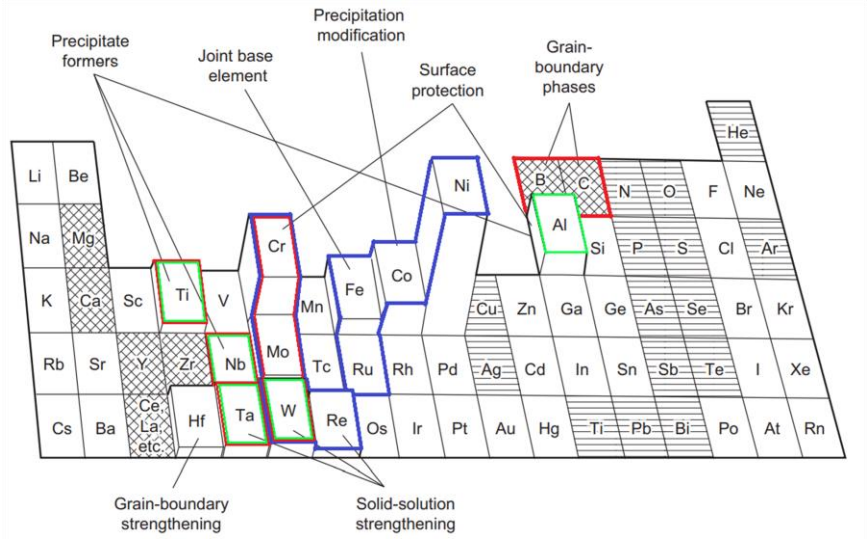

Figure 2.8 Known effects of the elements in Ni-based superalloys, the height represents the relative amount that can be present in a system. Beneficial and harmful trace elements are marked with cross hatching and horizontal line hatching respectively [13]. Colored frames indicate blue γ strengtheners, green γ′ and γ″ formers and red carbides and borides formers.

[2] Not all these effects necessarily occur in a given alloy.

2.2.3 GB segregation and precipitation in Ni-based alloys processed by traditional methods

Some properties of polycrystalline materials like grain growth, hardening, corrosion, and fracture are deeply influenced by intergranular segregation [95]. Precipitates and dislocations interact to greatly influence the mechanical characteristics of Ni-based superalloys. Defects in two and three dimensions of polycrystalline materials are closely linked to grain boundaries. Atoms at the boundary interface with a different orientation create pileups, which form concentrated two-dimensional disordered faults. These faults can increase the free energy of the substrate, promoting precipitation of second phases [96]. Moreover, it has been demonstrated that solute segregation reduces this free energy [97].

On the other hand, GBs represent a transition region where the regular and periodic arrangement of the lattice of two adjoining grains of the same phase is lost. The atomic structure at this region is crystal-like and can present different arrangements that are commonly defined as Low-Angle grain boundaries (LAGB), High-Angle grain boundaries (HAGB), and particular arrangements of HAGB with a Coincidence Site Lattice (CSL) structure [98]; further details are in Section 2.4.8. GBs have more free energy than the crystal nucleus due to differences in the atomic arrangement between the bulk of the crystal and the GB.

Like all metal alloy systems, the arrangement of the atoms looks for a minimization of the Gibbs free energy. Segregation is a thermodynamically preferred process that reduces energy, specifically *interfacial segregation*. This phenomenon involves the interaction of grain boundaries with crystal defects of foreign atoms. As energy decreases, foreign atoms accumulate at the limit of solubility in the base material, leading to the precipitation of secondary phases. [99].

There are two classifications in GB segregation *(a)* equilibrium and *(b)* non-equilibrium [100]. *Equilibrium* is a phenomenon of a very local redistribution of solutes that results in an enrichment of GBs. Inhomogeneities in the material lead to sites where solute atoms have a lower Gibbs energy, giving as a result of *equilibrium* segregation. These places can be found at interfaces such as the free surface, GBs, and phase interfaces as well as defect locations, dislocations, and stacking faults. On the other hand, *non-equilibrium* GB segregation takes place through the replacement of solutes in a system with excess vacancies, this occurs as a consequence of metallurgical operations and it expands over several micrometers beyond GBs [99].

In the case of precipitation, it follows a similar path as the solidification process with a spontaneous growth of solute clusters, nucleation, growth, and coarsening stages Section 2.1.2.

The driving forces for nucleation are the degree of supercooling (enough time and activation energy) and supersaturation. But, in contrast to the traditional theory, the diffusivity of light elements (i.e. C and O) gives the possibility that the composition of the precipitate varies during nucleation consolidation [36]. This situation provides different properties when there is a cluster of solutes than when they become precipitates. The interesting thing is that these precipitates and/or clusters can appear at any time from manufacturing to during the service life of the metal alloy.

The second phase formed immediately after nucleation may not necessarily be the most stable phase. These fine precipitates emerge during solidification at GBs, driven by processes such as diffusion, phase chemistry, interface constraints, permeability, and lattice defects [30, 101] The Gibbsian free energy (Gg) is determined by the volumetric free energy, surface free energy, and chemical potential [6, 102]. But also, when the solidification occurs at GB, it is influenced by the energy contribution of each grain and the energy at the interface. If the solute concentration of atoms reaches a lower minimum of this G_g, precipitation instead of grain boundary formation and/or segregation will occur. In accordance with Kirchheim [102] this event is expressed in accordance to the following inequality:

$$(10{,}000 \pm 6{,}000)\Gamma_A < \gamma_0$$

Equation 2-3

Where Γ_A is the excess energy amount of A at the boundary in mol/m^2 and γ_0 is the GB energy in J/m^2.

However, it is important to note that multiple transformations can occur from one metastable phase to another in a step-by-step manner [99]. When an area of the GB reaches equilibrium, a direct consequence is the cessation of grain growth [102]. The growth, coarsening, and stabilization of precipitates is a continuous and multi-component process, that leads to the evolution, transformation, and replacement of precipitates within the solid solution, due to thermomechanical processes [21].

2.2.4 GB carbides in traditional manufacturing of Ni-based superalloys

In Ni-based alloys, the type of carbides depends on the alloy composition and the processing conditions employed, some of the most important are MC, M_6C, and $M_{23}C_6$ [94]. The $M_{23}C_6$ and M_6C carbides have traditionally been linked to carbide strengthening [103]. Ni-based superalloys which contain carbides have superior creep resistance compared with those that are strengthened by PS γ' and γ'' intermetallic phases, and it is documented that the existence of organized chains of uniformly distributed discrete carbide particles along the GBs

prevents GBs sliding and migration, in particular $M_{23}C_6$ [104]. There is an interest in finding the appropriate distribution, structure, and morphology that optimize the properties of a Ni-based solid solution.

It was established in section 2.2.2, that some elements promote the precipitation of carbides and borides, but also, other elements influence their structure and morphology. A. K. Jena et al. [104], have a comprehensive review of these effects. Increasing the concentration of elements that promote carbide formation leads to the precipitation of carbides in the following general order:

$$MC \rightarrow M_6C \rightarrow M_{23}C_6$$

The MC form is the most stable, and usually, it is formed during solidification, and may also precipitate in the solid state when the M fraction is Ti, V, Cr, Nb, Ta, Mo, or W. Among the shapes that the MC carbides can adopt are generally angular, cubic- or diamond-shaped blocky particles present at GBs and in the matrix.

Moderate and high concentrations of Cr ≥ 18 wt. % lead to the formation of $M_{23}C_6$ at any stage of solidification, low-temperature HT, as well as after prolonged exposure to heat and pressure during service. The elements that may become part of the $M_{23}C_6$ on the M metallic radical are (Ni, Co, Fe, Cr)$_{21}$(Mo, W)$_2$C$_6$. $M_{23}C_6$ located at GBs, with forms such as films, plates, or discontinuous irregular particles are associated with harmful effects like poor ductility and an increased cracking tendency, also cellular morphology or eutectic colonies reduce ductility, strength, and notch rupture strength. These carbides can form in two different ways, by decomposition of M_6C and MC carbides, and by direct precipitation from the γ matrix [105].

Table 2.2. Lattice parameters of different phases in Ni-based superalloys.

Component of the system	**Crystal Structure**	**Lattice Parameter Å ($1x10^{-10}$ m)**	**Source**
γ phase	FCC	3.58 ± 0.02	H. M. Tawancy [106] S. Pourbabak et al. [47]
M_6C, Mo-rich carbide	FCC	11.05 ± 0.02	H. M. Tawancy [106] G. Marchese et al. [107]
$M_{12}C$, Mo-rich carbide	FCC	10.87 ± 0.01	H. M. Tawancy [106] G. Marchese et al. [107]
$M_{23}C_6$, Cr-rich carbide	FCC	11.12 ± 0.22	X. Dong et al. [21]
M_mC_n, Mo-rich carbide	FCC	10.58 ± 0.07	G. Marchese et al. [107]

Both M_6C and $M_{23}C_6$ carbides exhibit a similar structure, with a lattice parameter of approximately 1.1 nm in their FCC structure variants (Table 2.2). It is worth noting that according to Vergard's law [108], the lattice parameter of γ-phase is dependent on the solute concentration. This principle also applies to secondary phases with similar stoichiometry, as indicated in Table 2.2. Consequently, the spacing between atoms in the crystalline arrangement of the solid solution can either increase or decrease depending on the chemical composition.

But, M_6C carbide is more unstable than Cr-rich $M_{23}C_6$ carbide during aging at intermediate temperatures, particularly documented in HX materials [109]. Content greater than 6 – 8 wt. % of refractory metals such as Mo and W leads to precipitation of M_6C type carbides [110], with a stoichiometry of $(Ni, Co, Cr)_4(Mo, W)_2C$. The forms reported for this type of carbide are blocky particles and the undesirable Widmanstatten morphology that degrades mechanical properties. The likelihood of the formation of this carbide increases with the addition of Si.

Even though carbides have been described as stable or meta-stable particles, in reality, these can be found in different stages of consolidation or transformation. X. Dong [21] correlates misorientation angle with carbide-type formation, based on the relationship of the different types of carbides with the γ/γ' prime phases in the superalloy SRR99. The main findings of the study reveal the presence of (Ta, Ti)C carbides, which exhibit a blocky or needle-like form and are sparsely distributed at GBs. Additionally, $(Cr, W)_6C$ carbides with a blocky morphology are observed, although they are smaller compared to the MC type carbides and appear in higher concentrations. Furthermore, finer $(Cr, W)_{23}C_6$ particles are also identified in the microstructure. Another important highlight is that MC carbides are decorated by M_6C and $M_{23}C_6$ which suggests that metallic compounds (Cr) tend to segregate out of the carbide in certain areas Figure 2.9. Regarding the $M_{23}C_6$, evidence implies that it precipitates easier at 4˚ than at 13˚.

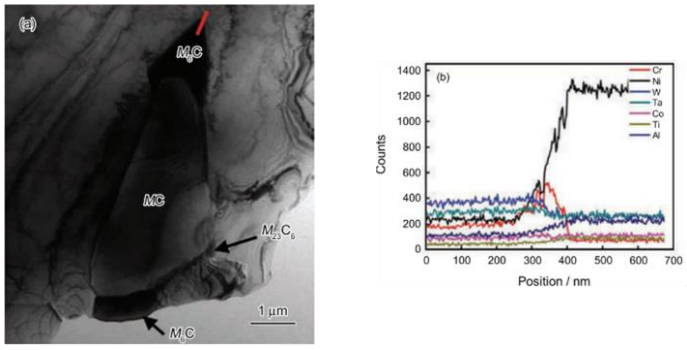

Figure 2.9 a) SRR99 Ni-base alloy with MC carbides decorated by discrete M_6C and $M_{23}C_6$ particles, b) and EDS line scan profile red line [21].

In the sense of the relationship between the preference of carbides to nucleate and the GB character, it has been found that in HX after a long-thermal exposure of 850˚ C [58], there is a strong correlation with the behavior of the precipitation M_6C carbides, and highly ordered CSL Σ3 GB, as well as Mo segregation in the first instance at random grain boundaries (RGB) in the vicinity of Σ3 GB, which in turn can cause the appearance of mu (μ) phase on GBs.

2.3 Hastelloy X

Hastelloy X (HX) is a SSS Ni-Cr-Fe-Mo alloy that is resistant to creep and oxidation at high temperatures with the additional advantage of superior fabricability and weldability, which not all Ni-based superalloys possess. HX is a Haines proprietary composition that was formulated in 1952 and first used for a Boeing 707 JT-3 engine [34]. This alloy is currently used in a variety of applications, including gas turbine engine parts such as combustors, transition parts, and exhaust end components. [17].

HX does not contain any form of γ' or γ'' phases. The strength developed by this Ni-based alloy is due to the addition of solid solution elements and carbide formation, the latter is highly dependent on the composition of the alloy, which in turn will affect the kinetic behavior and morphology of precipitating phases [108].

The nominal composition for HX in accordance with the Haynes International datasheet [111] and ASTM international [112] is given in Table 2.3. The presence of this amount of C coupled with other elements like Mo, Cr, and W (Figure 2.8 blue frame) can promote the appearance of carbides. Some of these particles nucleate and grow, at the end of the solidification and in short periods of thermal regimes, J-C Zhao et al. [17] developed a time-temperature-transformation (TTT) diagram, which gathers the known information regarding the phase transformation of HX and elaborated C-curves for the behavior of the M_6C and $M_{23}C_6$ carbides, and μ and sigma (σ) phases (Figure 2.10).

Table 2.3. The composition limits, as specified by Haynes and the chemical requirements outlined in ASTM B 572–06 (2016), are expressed in weight percentage (wt.%).

	Ni	**Cr**	**Fe**	**Mo**	**Co**	**W**	**Si**	**Mn**	**C**	**O**	**P**	**S**	**B**	**Nb**	**Al**	**Ti**
Haynes Int™	Bal.	22	18	9	1.5	0.6	1.0 max	1.0 max	0.1	-	-	-	0.008	0.5 max	0.5 max	0.15 max
UNS N06002	Bal.	20.5 ~ 23.0	17.0 ~ 20.0	8.0 ~ 10.0	0.5 ~ 2.5	0.2 ~ 1.0	1.0 max	1.0 max	0.05 ~ 0.15	-	0.04	0.03	-	-	-	-

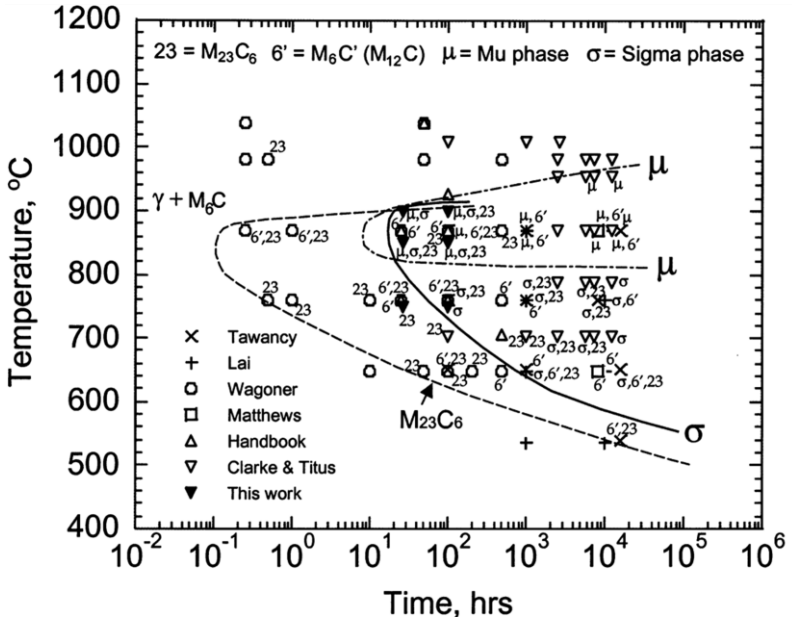

Figure 2.10 Hastelloy X TTT diagram [17].

This work also offers evidence that M_nC_m carbides precipitate primarily on GBs, as well as that μ and σ phases. The μ (A_6B_7) and σ (A_2B) phases are recognized as topologically close-packed (TCP) phases, generally formed during thermal processing and/or during long-term service, these phases are not desirable since they can promote premature failure. TCP phases can have a wide variety of stoichiometries, generally speaking, they have a base chemical formulae A_xB_y, where A and B are transition metals, such that A falls to one side of the group VIIB column defined by Mn, Tc, and Re and B falls to the other.

2.3.1 Hastelloy X manufactured by LPBF and GBs carbides behavior

Segregation kinetics in AM work differently than their wrought counterparts, as mentioned earlier in this text, the main differences come from the speed at which melting and solidification happen, as well as the intrinsic thermal cycles imposed on the system, caused by the continuous melting and reheating inherent to the process itself, and the flow heat through the previously deposited layers [113]. This aspect, linked to the chemical composition of the HX results in the presence of complex carbides not seen in other PBF-processed Ni-based superalloys, even with evidence that does not agree between similar conditions.

Almost all the study of the evolution of carbides in HX has been inextricably linked to the performance of HT, particularly aging. The above is due to the HT suggested by the manufacturer to homogenize the microstructure or the anticipated service conditions where HX

is commonly exposed to high temperatures. However, this study primarily reports on the microstructure observed in the AB condition, unless explicitly stated otherwise.

For instance in the work of Harrison et al. [114], with the aim to reduce the micro-cracking density, the group optimized the LPBF scan strategy, and modified the base chemical composition of HX, reducing tramp elements (O, N, Cu, Pd, and P) and increasing small amounts of substitutional solid solution strengthening atoms (Cr, Mo, Co, and W). The main result was about a 65% reduction in micro-cracking density in the compositionally modified sample in AB condition, due to the increasing Thermal Shock Resistance (TSR). But they also reported that there was no segregation or secondary phase precipitation at GB in both the unmodified reference sample and the compositional modified sample, just by optimizing the scanning strategy. The explanation they provided is that the solute trapping had occurred by imposed rapid solidification conditions, and thus secondary precipitate formation was suppressed.

D. Tomus [44], on the other hand, proposed the reduction of minor alloying of Si $\leq$ 0.11 wt. % and C $\leq$ 0.01 wt. % in the HX composition, in order to reduce the hot tearing propensity. This detrimental propensity is attributed to the presence of Mo-rich M_6C carbides linked to the enrichment of GB with Si. The main finding in the control sample without compositional modification (C~0.006 wt. %) is the observation of MC carbides decorated with traces of σ phase, which is associated with the formation of micro-cracking. Q. Han et al. [115], with the same approach as Tomus, printed lattice structures with limited wt. % in Si, Mn, and C in HX composition, with a combined amount of these three elements of 0.2 wt. %, and confirmed the presence of Mo-rich carbides, on micro-crack areas at GB, confirming that element segregation occurs at the GBs during the rapid solidification process. No traces of Cr-rich carbides were found, maybe because parameter processes did not give time for $M_{23}C_6$ carbides to precipitate.

Marchese et al. [107] in their study of LPBF-HX-AB found the presence of M_6C, $M_{12}C$, and M_nC_m carbides type with a size up to 500 nm and globular and elongated shapes, they detailed the rejection of elements with high susceptibility to segregation (i.e., Mo, W, C, Si) from the bulk to interdendritic regions and GBs, this rejection as a result of continuous heating and cooling cycles from the deposition of new layers the that promotes the formation and coarsening of carbides. The formation of Mo-rich M_6C carbides occurs during the last stages of solidification, while both Mo-rich M_6C and Mo-rich $M_{12}C$ are typically found in heat-treated HX alloys Figure 2.11.

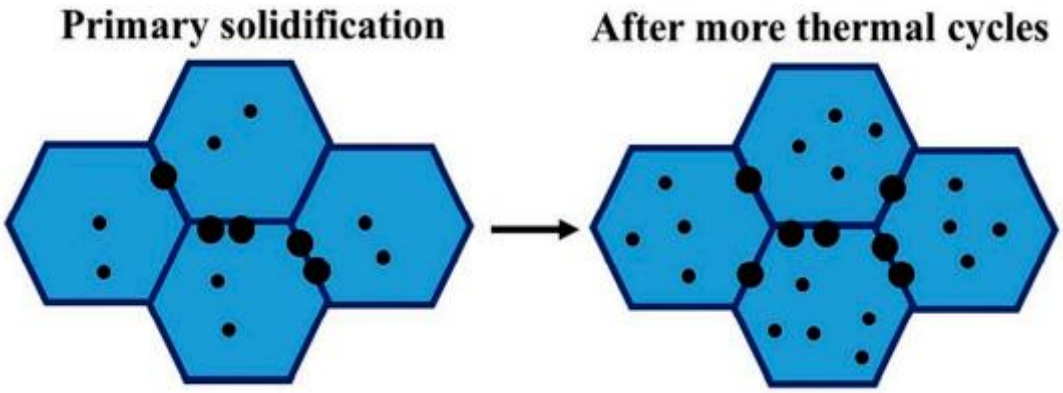

Figure 2.11. Marchese's schematic dendritic structure behavior of carbides in AB-condition, and subsequent thermal cycles.

O. Mata-Sanchez et al. [42], produced crack-free HX-LPBF-AB samples, by manipulating the LPBF process parameters, with this strategy they achieved sound samples that withstood the recommended aging treatment without cracks. An important characteristic of the Mo-rich carbides found along GB was their nanometric size of ~55 nm average, which is one order smaller than those reported in other studies.

Haines et al. [35] pointed out that elemental partitioning is affected by parameters other than cooling rates such as solidification velocity, thermal gradient, and undercooling, which could have provided more information in initial studies, and by reviewing the findings on HX so far they conclude that during LPBF manufacturing of HX predominantly spherical Mo-enriched M_6C, $M_{12}C$, and M_nC_m appears, and cooling rate is not a determining factor for the type of carbide.

As can be seen, by the available literature, there is still no conclusive evidence, of the exact impact of the process parameters on the final characteristics of the secondary phases. A large amount of research focuses on the change of one or two processing parameters at most, and keeping the rest fixed, making it challenging to understand how changing processing conditions may impact the partition coefficient during the PBF process.

One last aspect that is worth noting, some mechanisms are involved in this process, firstly the partitioning of elements occurs due to differences in equilibrium composition between the solid and the liquid phases. The supercooling rates in LPBF do not permit complete solute trapping, as in the casting process, however, they lead to a non-equilibrium solidification of elements where certain solutes can be found partitioned into the matrix.

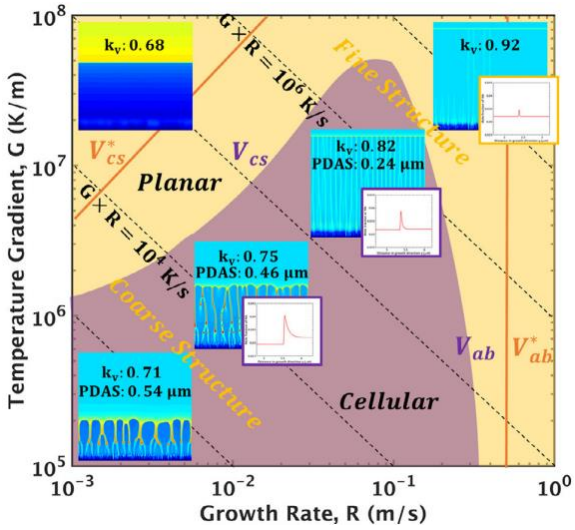

Figure 2.12. The variation in morphology, size of cellular segregation structure, and microsegregation as a function of growth rate and temperature gradient. Variation from Figure 2.5(a) [30].

It was mentioned that it is possible to achieve almost any microstructure with the correct scanning strategy (planar, cellular, equiaxed, and dendritic). Moreover, it has been shown that certain preferred crystallographic orientations exist depending on the values of G/R and $G \times R$ parameters, as well as the chemical composition of the alloy. Finally, another aspect arising from these factors is the tendency to segregate elements and form secondary phases.

K. Karayagiz et al. [30] raise the fact that the segregation coefficient (k_v) increases with certain solidified microstructures. Figure 2.12, shows a fraction of the diagram of the relation of the columnar-to-equiaxed transformation (CET) and the variation of G and R, where the behavior of the microsegregation is depicted graphically as a function of the microstructure.

The kinetics of phase transformation must take into consideration the role that α/β [new phase (β) in a parent phase (α)] interface plays [116]. The atomic structure relationship of the second phase precipitate changes if this appears within a grain, or if this nucleates at the GB. Generally, the continuity in the arrangement and the parameters matching the crystal lattice are denoted in terms of coherency. Precipitates on GBs usually fall in the category of incoherent or semi-coherent, fully, or partially along all the n-sides interactions of the number of grains in the intergranular surface.

2.3.2 Defect formation in HX-LPBF-AB

Porosity and cracking are common defects that can be found in HX-LPBF, but they are not exclusive to the LPBF process or the HX alloy. These issues are commonly encountered in

AM fabrication as a whole. [48, 117-119]. Due to this reason, both academia and industry are investing significant efforts in enhancing the LPBF process to ensure greater reliability. The following is a brief description of the findings regarding the main mechanisms believed to contribute to cracking, as identified in the aforementioned investigations.

The work of Harrison et al. [114] addresses two processable indicators that lead to micro-crack formation, namely thermal stability and Thermal Shock Resistance (TSR). Thermal stability refers to the degree to which a material will deform or deflect for a given heat input and geometry while TSR refers to the capacity of the material to resist crack development as a result of a change in temperature for a given heat input and geometry.

D. Tomus et al. [44] elaborated on two primary factors that are drivers of crack formation and propagation: (i) internal strain accumulation due to thermal cycling and (ii) hot tearing, a multifactorial phenomenon that can include alloying elements, freezing range, amount of eutectic phases, and solidification rates.

Q. Hang [115], confirmed the apparition of micro-cracking in HX printed samples, with limited content of Si, Mn, and C, and also highlighted its preponderance on HAGB Figure 2.13 *c)*. Also, by changing the composition of the HX, was observed an increment of LAGB content fraction, and also a reduction in yield strength.

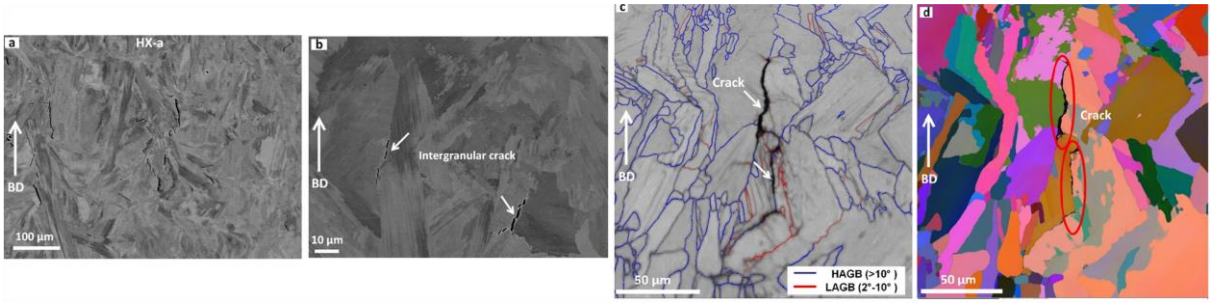

Figure 2.13. Different ways to question descriptors by SEM based techniques in cracking appearance HX, (a)-(b) BSD-SEM micrographs, (c) GB character map (d) EBSD grains colored [29].

What could be considered the principal theory of Marchese et al. [107] regarding cracking causes and propagation in HX-AB, is the presence of carbides in conjunction with the high thermal residual stresses inherent to the LPBF process.

O. Sanchez-Mata et al. [42], recognize that the cracking susceptibility of HX is influenced by a mechanism similar to that observed in welding processes. This mechanism involves the formation of a liquid film over an intergranular region containing low melting point eutectics.

As has been stated in the paragraphs above, the main solutions currently used are tailoring the base chemical composition of HX [29, 44, 114] and adding ultra-fine equiaxed inclusions [120]; secondary post-fabrication routes, like hot isostatic pressing (HIP) and heat treatments (HT) [29, 46, 47, 54, 121-123]; and by manipulation of input parameters during the AM process [53, 81, 114, 124].

Each of these solutions has its own advantages and disadvantages. It has been documented that altering the chemical composition and introducing additional elements to the base elemental composition can potentially degrade mechanical properties. This presents a challenge for materials scientists and engineers who need to determine the optimal amounts of these additives to avoid negatively impact the established composition that has proven effective. With HIP porosity can be closed, however, surface cracks and open porosity remain, in addition to this low cooling rates could produce potentially negative effects on tensile properties, due to carbide formation [122], not to mention the additional cost.

Manipulating LPBF parameters has a promising future to control microstructure and mechanical properties. Since the inception of the process, there have been successful attempts to fabricate single crystal components in various materials by carefully adjusting the process parameters. This highlights the potential for achieving desired microstructural characteristics and mechanical behavior through parameter control in LPBF. [125]. In this sense, the acquired knowledge can be transferred to control the GB Character Distribution (GBCD) and to some extent, the formation of carbides. This means that it is possible to connect AM capabilities with grain boundary engineering (GBE), allowing for better control over the microstructural features in the printed components.

2.4 Scanning Electron Microscope (SEM) based techniques principles and theory

Three primary radiation sources are used for different diffraction techniques in texture analysis: Neutrons, X-Rays, and electrons. These signals interact with matter in different ways [126]. The principle behind the SEM is based on the interaction between an electron beam and a sample. By utilizing various detectors and configurations, the user can examine different signals and obtain diverse microscopic descriptions. This versatility enables detailed exploration of samples at the microscopic scale.

The signals coming from the Backscattered Electrons (BSE) have been demonstrated to provide valuable information on the surface in different ways. Two methods of processing this

electron-specimen interaction are Electron Channeling Contrast Image (ECCI) and Electron Backscattered Diffraction (EBSD).

Roughly the principle of SEM is to accelerate a beam current from an electron source and reduce its cross-sectional diameter or "spot size" through a series of Magnetic Lenses. The reduction of the spot size must be sufficient so that at the moment of hitting the coupon, the electron beam interacts only with the features of interest (resolution) and at a certain depth to emit different signals of each layer, such as electrons with different levels of velocity and energy, photons, X-ray, Auger electron, radiation, phonon, plasmons, to name the most used.

One of the most useful signals for microstructure characterization, produced by SEM is the so-called Backscatter electrons (BSE). These are electrons subject to Elastic Scattering events that interact mainly at the specimen surface. Some characteristics of these signals are their negligible loss of kinetic energy and change in the trajectory with respect to the normal of the beam in the range 0-2π radians (0°-180°) with an average of about 2° to 5°, rigorously, the cumulative effect of numerous small changes in the trajectory gives the final angle (>90°) to scape of the specimen.

BSE provides information sensitive to the surface, data such as composition (atomic number or compositional contrast), local specimen surface inclination (topographic or shape contrast), crystallography (electron channeling), internal magnetic fields (magnetic contrast), texture (single crystallite orientation), among others, can be resolved from these signals [127].

The remaining electron interactions that exit the sample and result in a significant loss of energy are referred to as inelastic events. These interactions can generate X-ray emissions that can be utilized for chemical analysis using a technique called Energy-dispersive X-ray spectroscopy (EDS) [127].

ECCI offers excellent spatial resolution, comparable to EBSD. In fact, depending on the electron source, the spatial resolution can be similar to that of Transmission Electron Microscopy (TEM) [128]. ECCI operates based on electron contrast mechanisms, and with careful setup, it becomes possible to discern small features such as dislocations.

The EBSD technique has been popularized because it characterizes and localizes individual grain orientations, local micro and macro texture, point-to-point orientation correlations, phase identification, and spatial distribution [129]. Also, the advantages of its performance, like concurrent rapid scanning, automatic signal indexing, and visual mapping interface, place it as the backbone of most microtexture research [126].

EDS (also known as EDX and EDAX), broadly, measures the energy of the displacement of electrons from an outer to an inner shell in an atom. The vacancy of electrons is promoted when the SEM electron beam impinges on any orbiting electron in the atom, the energy difference of the transition is unique in each element and shell, so the intensity of the signal gives a fingerprint of the element in question [130].

2.4.1 Electron Channeling Contrast Imaging (ECCI)

Electron Channeling Contrast Imaging (ECCI) is recognized as a forerunner of the EBSD technique. Nowadays, ECCI has been developed as an independent characterization method that complements EBSD imaging since it is used to take advantage of the BSEs. These signals are known as “Kikuchi-like” bands or Electron channeling patterns (ECPs). The term channeling comes from the description of the motion of charged particles inside a crystalline lattice [131-133].

In crystalline materials, the contrast is modulated by acceleration voltage, the atomic density of the material, surface inclination, angle of recording, and more important by the orientation of the crystal lattice with respect to the primary beam direction. When SEM is used, what the backscatter detector measures, is the density of electrons that are incoherently backscattered out of the primary Bloch wave field by the atomic nuclei in the crystal. As a result, specific crystal orientations backscatter more electrons than others, resulting in orientation contrast [20].

The primary beam electrons are Bragg scattered within the crystal lattice and form a lattice-coherent electron wave field that can be treated mathematically as Bloch waves, which describes the high-energy electron density distribution that is present in a crystal Figure 2.14. Bloch waves have different spatial distributions, additionally, this approach bears into consideration two types of beams; (1) waves have higher kinetic energy, and (2) waves have higher potential energy, these waves have different characteristics depending on their location inside the lattice.

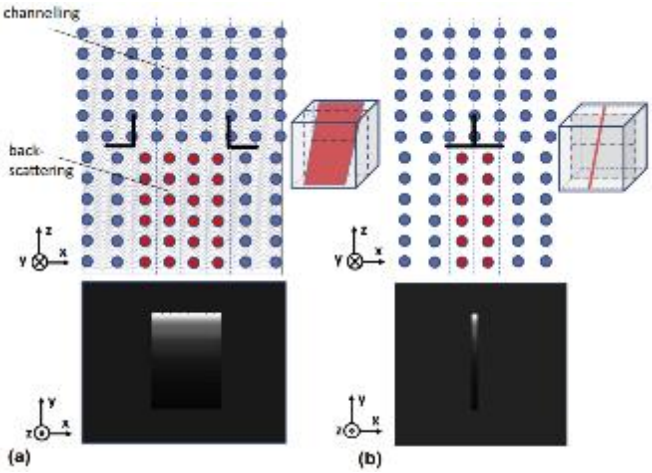

Figure 2.14. Schematic representation of the Bloch wave theory for the formation of defect contrast for (a) a SF bound by two Shockley partial dislocations and (b) for an edge dislocation [20].

It is assumed that the effect of a crystal lattice may be represented in terms of channels or paths where the particle can ideally penetrate to a higher depth before scattering. The misalignment between columns of the lattice will be visualized as a contrast in the image. Depending on the depth of the defect below the surface, backscattering is stronger or weaker, leading to intensity oscillations in the image in terms of brightness degradation. The mathematical development can be found elsewhere [20].

Electron channeling can be carried out in both high-tilt and low-tilt configurations, preferably using EBSD (ECCI under controlled diffraction conditions or cECCI) to find the most suitable crystal orientation to perform the ECCI scanning. Use any suitable backscatter electron detection apparatus, such as forecaster diode detectors mounted on commercial EBSD systems or polepiece-mounted backscatter detectors. This method is primarily used to identify dislocations within the system, and a comparable method is TEM. Application over bulk samples and a larger scanning area are the advantages of ECCI over TEM, and the main constraint may be the high-quality surface preparation required.

ECCI has mainly been used to characterize small defects such as nano-twins and dislocations, but also several works have used it to confirm the presence of nano-precipitates [134-136], and GB delineation is always a feature to denote via this technique.

2.4.2 Electron Backscattered Diffraction (EBSD)

The EBSD technique is performed with the SEM simply by tilting the specimen at an angle of 70° to the incident beam and using some additional attachments to detect the elastic

scattering events or Backscattered signals that produce the Kikuchi Bands, the latter are the ones used to identify position and orientation of the grains in the specimen.

The main effect of tilting the specimen is to maximize the number of electrons to undergo diffraction and escape from the specimen (having lost virtually none of their energy) before being absorbed [23, 126].

As mentioned, the radiation diffracted by a crystal lattice is the foundation of the vast majority of texture analysis techniques. The essential aspects to be acquired are the symmetric relationships of the trajectories of the electrons ejected from the sample. With this information, it is possible to resolve the lattice arrangement and the crystal orientation of a defined volume for some frame reference.

From the bulk of electrons coming from the beam, only those BSEs' fractions that meet Bragg's law (Equation 2-4) are the most useful for generating distinguishable Kossel cones derived from Kikuchi patterns Figure 2.15*(b)*.

$$n\lambda = 2d_{hkl}\sin\theta$$

Equation 2-4. Bragg's Law

Where n is the reflection order, λ is the wavelength, d_{hkl} is the interplanar spacing, and θ is the angle at which diffraction occurs, Figure 2.15*(a)* depicts the physical interaction among these parameters.

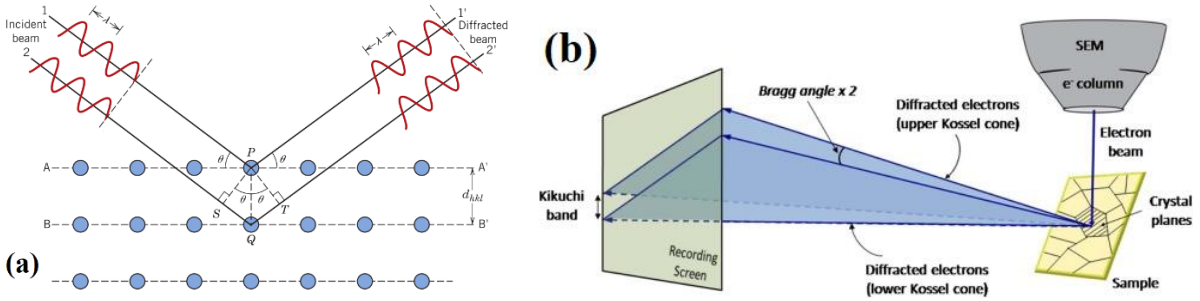

Figure 2.15 (a) Diffraction of radiation and relations with Bragg's law[6] . (b) Schematic Kikuchi patterns obtained by EBSD and its relationship with projected Kossel cones [31].

Kikuchi patterns are the data generated after a phosphor screen detects electrons (Figure 2.16 *(b)*). They have a regular arrangement of bright parallel bands (Figure 2.15 *(b)*), and their intersections form clearly identifiable zone axes. This regular geometry can be interpreted as a gnomonic projection of the crystal lattice.

It is worth noting that clear and high-intensity Kikuchi bands are observed for undeformed and perfect crystals, just with a slight curvature. On the other hand, in a deformed microstructure, crystals become distorted; thus, Kikuchi bands lose their sharpness and contrast. This fact will allow us to understand the study of strain with the EBSD technique later.

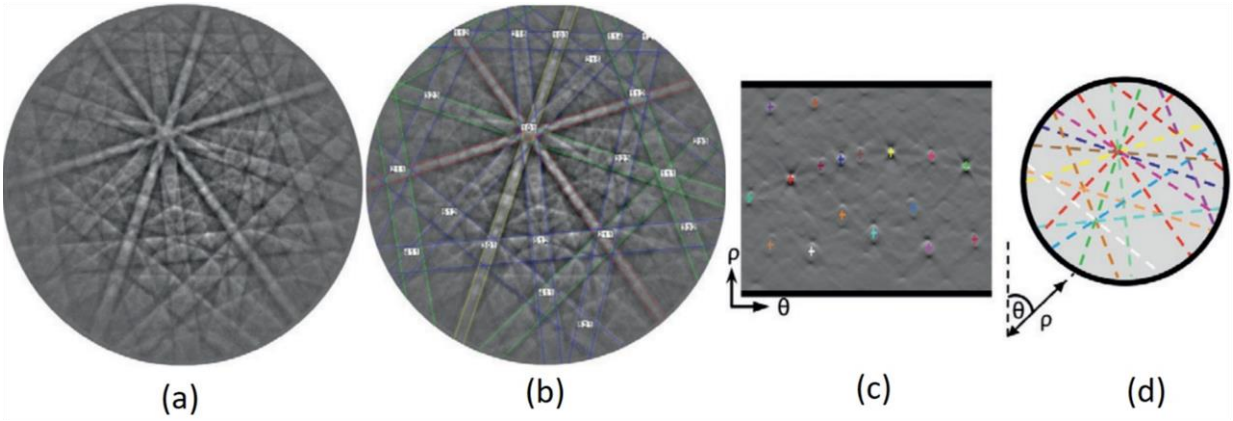

Figure 2.16: EBSD indexing procedure (a) Raw copper Kikuchi pattern, (b) Indexed pattern, (c) Hough transform, with peaks identified and (d) convolution of pattern in the original image [14].

Raw Kikuchi patterns can be indexed, generally by lookup in databases containing hundreds of Kikuchi maps, but this manual indexing work is tedious. It should also be noted that patterns are not perfect and lead to errors; for that reason, an automated evaluation is preferred.

2.4.3 Hough transformation

It is preferable to convert the acquired signals into data that can be processed and visualized more efficiently. Although there are several algorithms to detect the positions of the bands rather than the zone axes, the most preferred is the Hough mathematic procedure which permits precise localization of a large number of bands in digital Electron backscattered patterns (EBSPs).

Each crystallographic plane from the sample scanned is represented by a band of the Kikuchi pattern. The Hough transform algorithm converts the linear bands from the Kikuchi pattern to points or peaks of the Hough space. With this process, the location of the points is determined more accurately than the location of the lines Figure 2.16 *(c)* [23, 57].

The mathematical description of the transform from the coordinate (x, y) of the diffraction pattern to the coordinate (ρ, θ) of the corresponding bright point in Hough space is given by

$$\rho(\theta) = x_i \cos\theta + y_i \sin\theta$$

Equation 2-5.

$$\theta\epsilon[0,\pi];\ \rho\epsilon[-R,R]$$

Where the direction of the normal vector θ is restricted to the interval [0, π] so every line will correspond to a unique point in the θ-ρ plane, i corresponds to each pixel of a digitalized band from EBSP, R is the restricted distance from X-Y origin to the corners of an EBSP, and ρ is the length of a vector perpendicular (normal) to a line passing through a pixel i (distance from the X-V origin and pixel) Figure 2.17. Additionally to the transformation from (x, y) axes to (ρ, θ) Hough space, there is a third dimension that represents the intensity of each pixel I(X_i, Y_i) [57, 126, 129, 137].

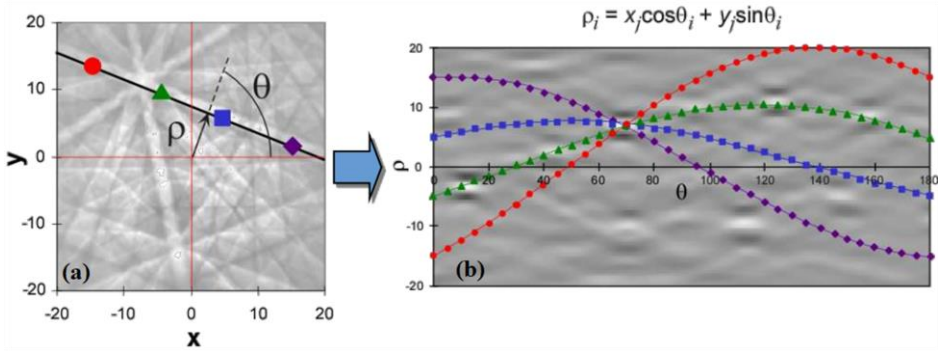

Figure 2.17. Correlations between (a) straight line described in a cartesian coordinated system that may be a Kikuchi band and (b) its transformation to a point in a Hough space.

The next step is to identify the Radon space peaks to convolute the original pattern into one that can be detected with high accuracy Figure 2.16*(d)*. The Original bands have been converted into a single line, running exactly through the midpoint of the original pair bands, with different intensities, and the background noise has been removed. This process allows a reliable and robust mapping of the scanned surface.

2.4.4 Data storage, display, and descriptors

A large amount of data can be characterized and described with the patterns acquired from the scanned sample. After processing the raw Kikuchi pattern to make it more manageable in a computing environment, one or more descriptors can be chosen to best represent and measure the desired features. Among the great variety of descriptors available, this work will focus on those that represent a crystallographic orientation, misorientation between adjoining grains, and local misorientation within predefined kernels.

There are two ways to locate the sampling points on a specimen surface (1) the movement of the entire stage sample holder with respect to the stationary incident electron

beam and (2) deflecting the electron beam across the stationary sample surface. Measurements rates can be up to $1s^{-1}$ and $5s^{-1}$, respectively [126].

A rule of thumb to get an outlook of microtexture, microstructure, and grain misorientation measurements is to use a step size of one-tenth of the average grain size [138]. More details of subtle orientation shifts within a grain require a smaller step size, therefore more time-consuming post-processing labor and computer storage.

Each digital sample point is stored in the computer memory with a regular pixel-based grid of the Kikuchi patterns indexation with its orientation, spatial coordinates, intensity, and often a pattern quality index. While the sampling area is scanned, the orientation map is built up pixel by pixel as each of them stores the information mentioned above.

The pixel map can be constructed using two grid patterns, either square or hexagonal, as shown in Figure 2.18 This enables the software to deconvolute the misorientation measures for the set of pixels within the grain and determine the mean orientation. The hexagonal grid offers an advantage as it provides more nearest neighbors, making it easier to delineate interfaces. [126, 127, 139].

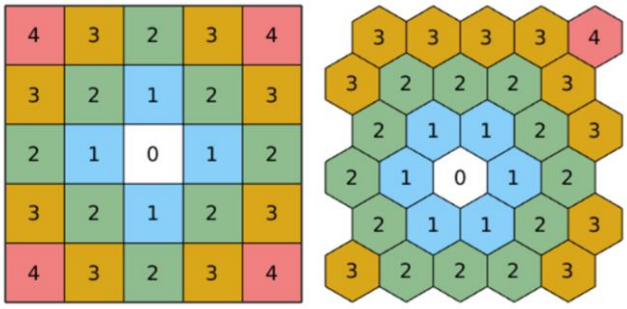

Figure 2.18. Square and hexagonal grid and their respective order of neighbors [8] .

2.4.5 Pole Figures

Pole figure (PF) is one of the conventional methods to depict texture, especially in the metallurgy field, it is relatively simple to interpret the information displayed, and several textures have a relation with a particular property of interest well known among the scientific community [129]. The PF is a two-dimensional stereographic projection in which the position and density of a particular crystallographic plane are plotted in relation to a specific frame of reference, generally to the specimen geometry [140].

The description of the crystallographic system and directions involves the Miller-Bravais indices notation (*hkl*) [*uvw*], [5, 11] and this will be displayed to denote the reference frame and the position of the crystallographic orientation in the circle.

The representation of the reference plane depicts the symmetry of the crystal itself, which means that the reference sphere is divided into spherical triangles by the crystal symmetry planes, which is the base of the inverse pole figures (IPF). Giving the coordinates of the spherical reference surface to correctly interpret the PF.

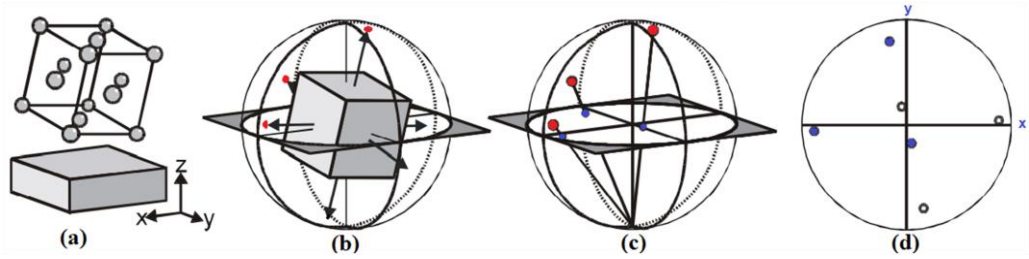

Figure 2.19. Process to elaborate a Pole Figure, (a) imaginary single crystal cell; (b) normal projection of crystallographic planes onto circumscribed sphere; (c) pole point location on the sphere surface (d) Pole figure projection [11].

Usually, it is set to the specimen geometry in terms of rolling or building direction (RD or BD), transverse direction (TD), and normal direction (ND). The density distribution of the crystallographic planes in the specimen can be related to the reference plane and its family planes. This statistical information allows us to know the degree of the texture in the material.

The PF map serves as a valuable complement to other maps or descriptors provided by EBSD. The term fiber texture is an additional note regarding PFs, and it refers to pole figure representations in the form of continuous band orientations, described by specifying the crystallographic direction ⟨uvw⟩ from materials that show rotational symmetry; such direction is parallel or nearly parallel to the axis deformation [140].

2.4.6 Inverse Pole Figures (IPF)

IPF represents the texture in relation to the crystal axes instead of the specimen geometry. The projection plane for an inverse pole figure only shows the distribution of the planes in a stereographic triangle Figure 2.20. These spherical triangles have different units representation for each crystal system. For instance, there are 48, 24, and 8 crystallographically equivalent stereographic unit triangles in the cubic, hexagonal, and orthorhombic systems, respectively. Even though this is a simple representation of the crystallographic plane density, its impact is more significant when combined with orientation maps.

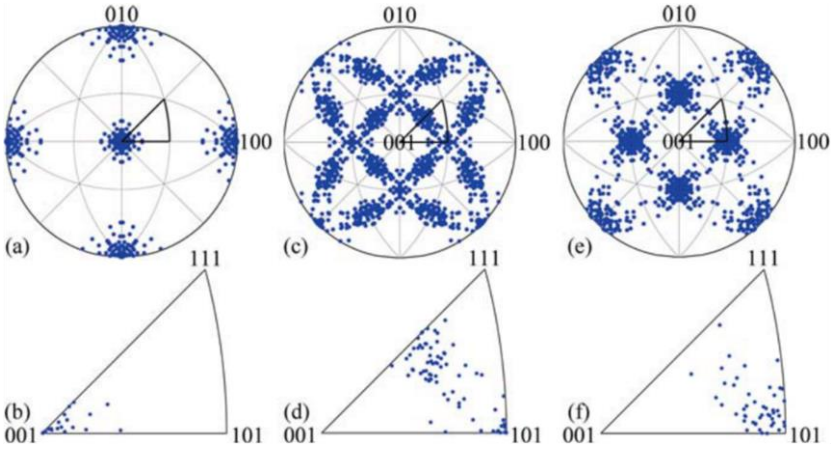

Figure 2.20. Normal-direction inverse pole figures for the three textures, Miller indices in the figure refer to directions in the local crystallographic frame. (a)A cube texture, and (b) the stereographic triangle. (c) A copper texture, and (d) the stereographic triangle. (e) A brass texture, and (f)the stereographic triangle [2, 5].

2.4.7 Image Orientation Mapping (IOM)

Orientation mapping is one of the most popular resources of the EBSD technique. Not only does a map have great visual appeal, but it also gives access to fully quantified orientation statistics. With this information, the user can correlate information spatially located point to point, such as individual grain orientation, misorientations, interfaces, perturbation/strains within the grain, and size/shape, as principal aspects.

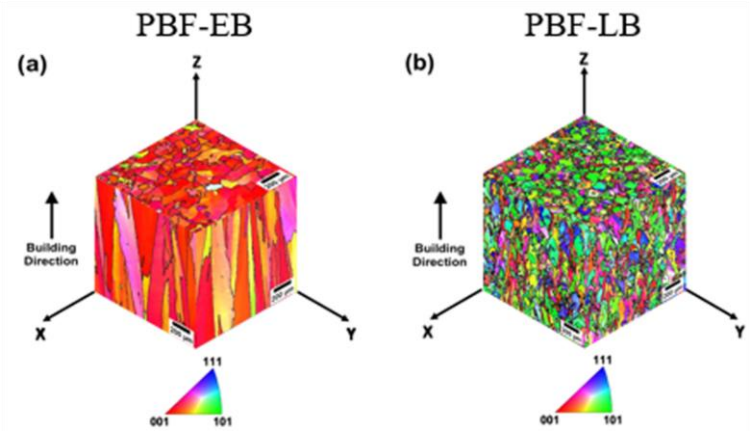

Figure 2.21. 3D reconstructed IPF maps of (a) PBF-EB and (b) PBF-LB specimens, and their orientation corresponding to each cartesian plane [24].

Briefly, the software endows each feature with a particularly distinctive, for example, color, grayscale, and even a tiny representation of the crystallographic system. With the aid of a color key or bar scale, it is possible to decode the spatial location of such characteristics into the map.

In the inverse pole figure (IPF) maps, it is possible to distinguish the shape of the grain, boundaries, and growth. By correlating the coordinate system with a reference frame external to the sample geometry, and subsequently linking this to the manufacturing orientation, the interpretation of grain behavior can be facilitated. In Figure 2.21 it is possible to visualize the three dimensions of the texture orientation of electron beam powder bed fusion (PBF-EB) and laser-based powder bed fusion (PBF-LB) samples.

It is worth noting that almost all descriptors, i.e., Euler angles and Rodrigues vector, can be represented by PF, IPF, and orientating maps.

2.4.8 Misorientations and interfaces

Even though interface boundaries could seem evident in an orientation map, due to the change of color between lattice orientations, it is possible to depict GBs showing different parameters. The relative orientation between two crystals is given by the necessary rotation of a crystal that brings it into the same orientation as the fixed-referenced crystal. The conventional description of the rotation of the angle/axis pair associated is the smallest misorientation, also known as disorientation.

The first classification of GB character is based on its simple degree of misorientation, high angle grain boundaries (HAGB) ≥ 10°~15°, and low angle grain boundaries (LAGB) ≤ 10°~15. Up to 10 to 15° of misorientation, the GB energy is known to grow linearly; the model that supports this threshold is related to the size of the Burgers vector $|b|$ and the dislocation spacing D by the expression:

$$\sin\frac{\theta}{2} = \frac{|b|}{2D}$$

Equation 2-6.

Elastic continuum theory describes the dislocation energy, since dislocations lose their character as θ increases, dislocation theory cannot be employed to further define GB structure beyond 13° to 15° [141], thereafter, the energy cusps appear at specific CSL misorientations essentially regardless of HAGB misorientation [126, 142-144].

Another characteristic that can be represented and quantified with the EBSD imaging data is the Coincidence Site Lattice (CSL). This attribute describes the point arrangement when two crystal lattices bring into a coincidence in one point, that in consequence, has the same coincidence point in a certain regularity (Figure 2.22). The notation to classify CSL is the reciprocal density of coincidence sites $\sum$. By convention, values greater than 29 are considered random, and values less than this are considered low sigma CSLs.

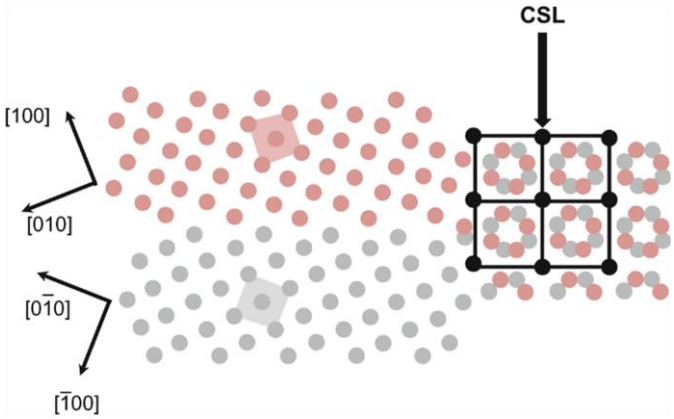

Figure 2.22. Structures within a lattice that coincide between two grains to evaluate the Coincidence Cite Lattice (CSL) [15].

These coincident arrangements have a significant effect on the interfacial energy. However, it is important to note that interfacial energy is a variable parameter that changes as the misorientation between two crystallographic orientations approaches a coincidence site lattice (CSL) condition (Figure 2.23) [15, 143, 145]. Moreover, segregation can also affect interfacial energy by flattening the peaks and valleys in its behavior [144].

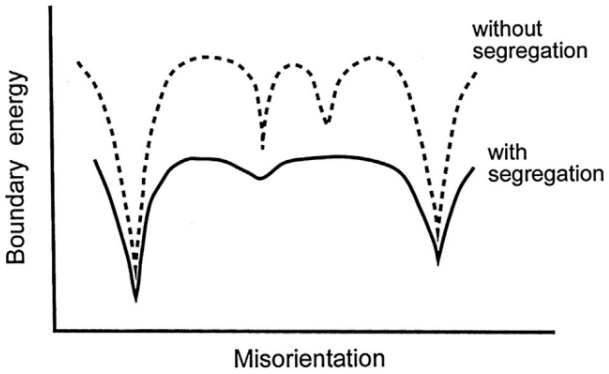

Figure 2.23 The schematic diagram illustrates the energy-misorientation relationship at GBs and the impact in the presence of segregation.

It is noteworthy that CSL and ∑ notation are useful if accompanied by other descriptors since there is no direct correlation between this kind of arrangement to any specific macroscopic property (Figure 2.24).

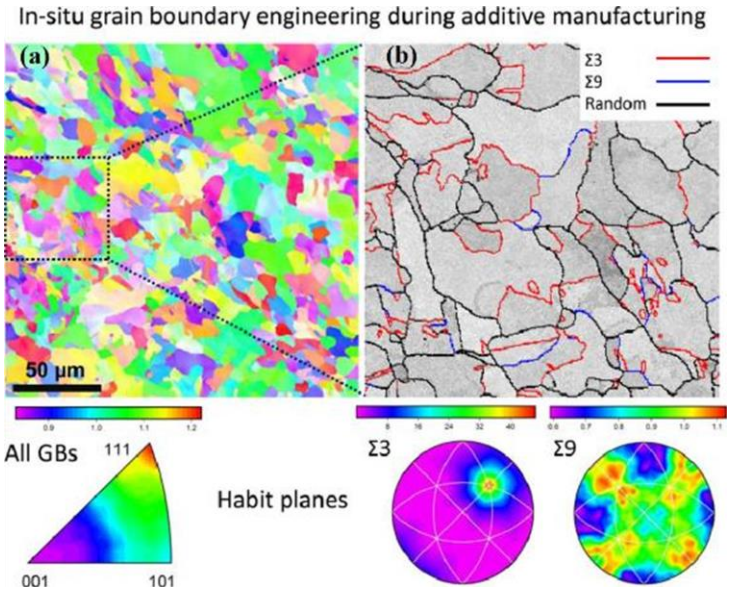

Figure 2.24. (a) IPF map and distribution of the GB planes irrespective of misorientation, expressed in the crystal lattice frames. (b) magnification of GB distribution map depicting specific boundaries, and GB character distribution [22].

Another effective method for visualizing the interconnection of GB in a network is through the representation proposed by S. Patala et al. [146, 147] for homophase misorientations. In this representation, a series of stereographic triangles are used to illustrate the misorientation angle and axis between two neighboring grains. The triangles are arranged in a sequence of increasing color shades, with darker shades representing larger misorientation angles.

The location of the misorientation axis is represented by a point on the stereographic triangle, and the orientation of the boundary plane at which the rotation axis is located is represented by a color key. The linkage between the stereographic representation and its location within the map is provided by the color tone and shading along the grain boundary which intuitively represents the gradient angle/axis pair [θ/⟨uvw⟩].

2.4.9 Intragranular misorientation

Typically, intragranular misorientation parameters are widely used for the failure analysis of metallic materials. The orientation gradient angle/axis pair [θ/⟨uvw⟩] is the most common descriptor for misorientations in EBSD analysis. A complete assessment of deformed

microstructure must be described in terms of misorientation since its variations are a good indicator of dislocation density and material distortion in metallic materials, in other words, the strain [22, 23, 119, 148].

The effects of the strain on the crystal lattice could be divided into two types, elastic strain (lattice imperfection) and plastic strain (lattice bending). Elastic strain is a non-permanent deformation, and its main effect on Kikuchi patterns is degradation in the form of blurring of the edges of the diffraction bands. This imperfection is a pretty small signal, resulting in only a pixel or two shifts in the zone axis positions, so high-resolution images are needed for the correct assessment.

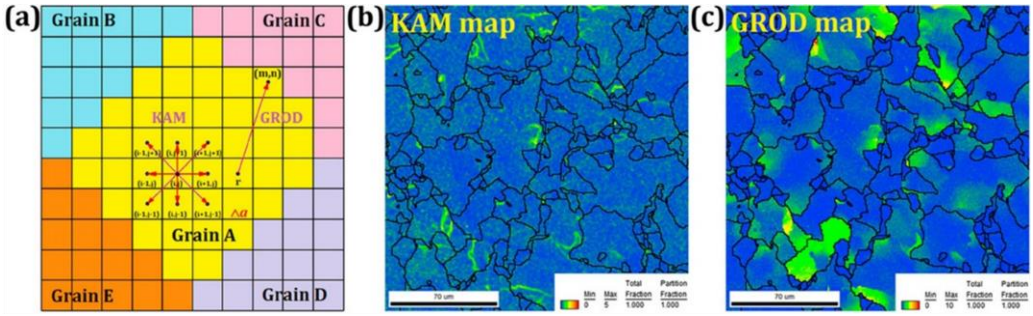

Figure 2.25. Definitions of KAM and GROD based on the square data structure, and examples of (b) KAM map and (c) GROD map [23].

In order to ensure consistent deformation within a polycrystalline material, voids and overlaps between individual grains are corrected by accommodating a portion of dislocations as geometrically necessary dislocations (GND). These dislocations are stored to compensate for the orientation-dependent anisotropy that would otherwise lead to their formation. [149].

Several methods characterize the strain distribution in the material, as previously stated. Residual strain manifests as local variations in lattice orientation, so some regions with high concentrations of low-angle boundaries indicate areas of concentrated GND density that may be described by local misorientation analysis. Different methods are generated from these studies for identifying certain aspects.

There are two basic types of local misorientation analysis: grain-based and kernel-based Figure 2.25*(a)*. The characteristics of the sample, including grain size, as well as the SEM settings such as step size and angle misorientation threshold/core size, will determine how the software algorithm clusters pixels.

Grain reference orientation deviation (GROD) is typically defined as the misorientation between an individual point and the intragranular reference point Figure 2.25 *a)* and *(c)* [60].

Kernel average misorientation (KAM) is defined as the average misorientation between a kernel point and its surrounding points, excluding those out of the GB Figure 2.25 *(a)* and *(b)*. it is usually regarded as a qualitative description of GND density distribution in both single-crystalline and polycrystalline metallic materials [148].

Also, these two descriptors can be divided into other descriptors depending on the reference point and the magnitude of the comparative measure with its neighbors. The information of descriptor and meaning of maps like *grain orientation spread* (GOS), *grain average misorientation* (GAM), *kernel orientation spread* (KOS), *kernel average neighbor misorientation* (KANM), and *kernel average center misorientation* (KACM), can be found elsewhere [60].

2.4.10 Band contrast or Image Quality map

BC or IQ is a metric that describes the quality of a diffraction pattern. An IQ map is constructed by mapping the IQ value measured for each diffraction pattern obtained to a gray or color scale during an OIM scan. Another is the sum of the peak sharpness of all detected peaks in the Hough transform. This parameter provides information related to local crystalline perfection, sample preparation, surface contamination, phase, and orientation information [1, 126, 140].

Image quality maps, also known as band contrast images, highlight details like grains, grain borders, and surface imperfections that are not evident in secondary electron images [126]. IQ_{HT} averages Hough transforms intensity peaks; Intensity mean of the pattern (IQ_M), intensity deviation (IQ_σ), and entropy (IQ_E), per S.I. Wright [1] are metrics that describe different aspects in a BC/IQ map. IQ_{HT}, provides the best description of GBs and strain, whereas the pattern intensity means, IQ_M, provides better phase and topographic contrast Figure 2.26.

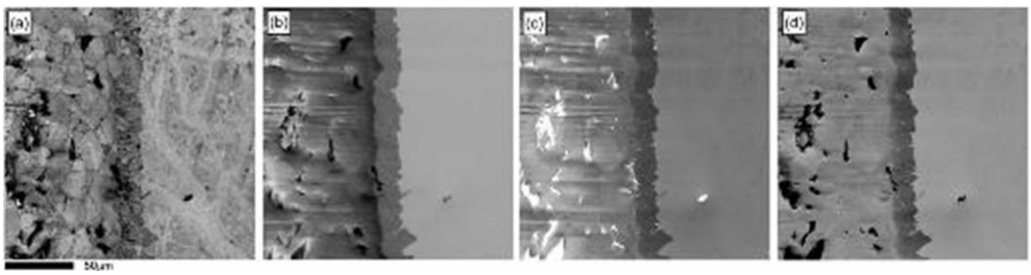

Figure 2.26. (a) IQ_{HT}, (b) IQ_M, (c) IQ_σ, and (d) IQE, maps of the Al-Cu reaction zone sample. [1, 2]

When working with EBSD, this descriptor is typically employed as a background; however, it possesses inherent value on its own.

2.4.11 Energy-Dispersive X-ray spectroscopy (EDS)

Through a simple Bohr model of the atom, it is possible to develop the theory of X-Ray emission, the model mentioned is not accurate in all of its aspects, but it fits well to describe the processes and behavior of the X-rays.

Essentially, two processes act in the emission of X-rays, i) the bremsstrahlung or continuous X-ray process and ii) the inner-shell ionization process, the latter provides the characteristic X-rays [127]. The Bohr atomic model suggests the presence of multiple electron shells surrounding the nucleus. Each of these shells accommodates a specific number of electrons, which is determined by their respective energy states. These electrons orbit around the nucleus composed of protons and neutrons. These shells are named with letters of the alphabet starting from the inner K-shell (the closest to the core) and so on outwards L, M, and N; there could be sub-shells from M forward.

The electrons positioned on each shell, have specific binding energies which maintain them orbiting, removing them from their place requires the energy of at least this binding energy. By removing the electron with another accelerated electron, the vacancy needs to be replaced by an outer-shell electron. The difference in the energy caused by the transition is released by one of two mechanisms, i) the Auger process and ii) photon electromagnetic radiation, the latter mechanism has a sharply defined energy, and it is possible to identify which shell the electron came from. The K_{α} X-ray arises from a transition from the L to the K shell, the K_{β} X-ray arises from a transition from M to K, the L_{α} from M to L, and so on [127, 130].

To detect the signals is required lithium-drifted silicon (or Si (Li)) or a high-purity germanium (HPGe) detector. The detector will register the total charge produced by each X-ray photon and convert it into a single voltage or digital pulse so that it can be read by software for post-processing or rendering purposes.

From the EDX/EDS signal, the user can obtain a map that colors each element, combining it with the morphology features, and it is possible to visualize the homogeneity and elemental distribution in the solid solution (metallurgy). In addition, a spectrum of functions can be represented that depicts the count of each shell of the type of atom. Where the *Y* axis is the number of counts, and the *X* axis is the distinctive energy of each shell of the element.

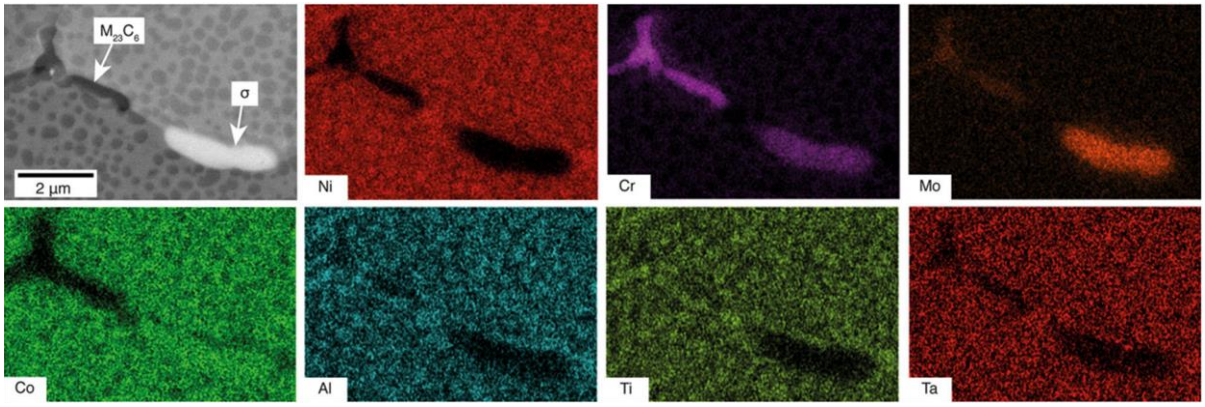

Figure 2.27 BSE SEM-based image and EDS elemental map of a GB of RR1000 Ni-superalloy, where two $M_{23}C_6$ and σ phases are identified [16].

The bigger the peak means the more of that element there was. The units can be in weight percentage or atomic percentage.

The major drawbacks are that this is a qualitative characterization technique, and it is not possible to get an exact stoichiometry. Furthermore, light elements like H or Li are not detectable.

2.5 Summary

This chapter provides general knowledge on AM technology, Ni-based superalloys, and characterization techniques to focus on the manufacture of HX-LPBF-AB parts, their evolution in solidification, driving forces, and aspects that affect their characteristics, as well as the main challenges to overcome, or how they are currently tackled.

Carbides located at GB have been extensively described in this work, as has been tried to set, there is a consensus among researchers on the fact that M_6C carbides play an important role in the formation and propagation of cracks, defects that have been stopping the progress of AM in a generalized use of Ni-superalloys in more critical applications.

With the aid of SEM-based characterization techniques described in subsection 2.4, the work done in the following chapters is based on the understanding of the interaction between the electron beam and its subsequent diffraction from the sample and knowing how each feature is represented in the final image. Therefore, this could give one an idea of whether the scanning was correctly done and if it is coherent with the phenomena or the contrary if there were deficiencies in sample preparation, SEM essential electron beam parameters selection, or post-processing.

Elaborating on the association of ideas stemming from the topics described in this text is of utmost importance to understand the effects of carbides located at GB, their occurrence, and the specific characteristics that promote cracking.

Chapter 3 Experimental Methodology

This chapter will discuss sample preparation, equipment for data acquisition, and post-processing methods used to characterize the density, morphology, and distribution of carbides located in GB.

3.1 Materials

The material used in this work was taken from crack-free HX-LPBF-AB samples manufactured by P^2[AM]^2 team, further details in [150]. The chemical composition of the powder used is shown in Table 3.1. The samples were processed in a Renishaw AM400 LPBF system equipped with an Nd: YAG laser operating at a maximum power output of 400 W with a beam diameter at a focus of ~ 70 µm, and an equivalent volumetric ED of 165 J/mm^3[150].

Table 3.1. HX powder chemical composition as certified by the manufacturer [150].Table 2.3

	Ni	**Cr**	**Fe**	**Mo**	**Co**	**W**	**Si**	**C**	**O**	**P**	**S**
This work	Bal.	21.2	17.6	8.8	2	0.7	0.2	0.06	0.02	0.002	0.002

3.1.1 Metallographic Specimen preparation

The original shape and size of the sample printed was a 50mm × 50mm ×10mm block from which a specimen of approximately 1mm × 4mm × 9.5mm, was extracted using a Buhler IsoMet™ slow-speed precision cutter (Figure 3.1 *a)*). These dimensions correspond to the coordinate system X, Y, and Z, where the Z-axis is the building direction (BD). The YZ plane was selected for analysis as the cracks tend to form along the intercellular and intergranular regions, which are parallel to the BD.

a) b)

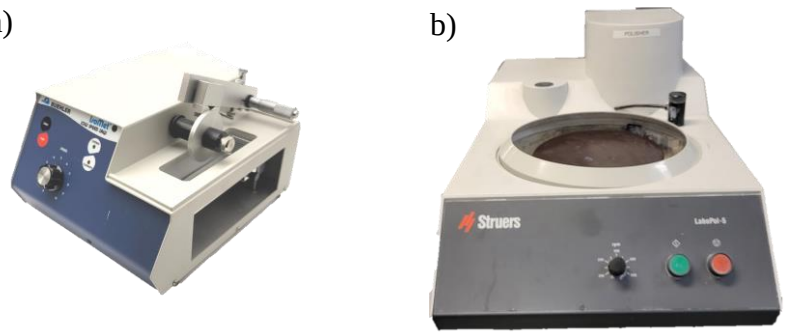

Figure 3.1 a) Low speed precision cutter, b) Polisher

The sample for SEM analysis was prepared by performing a standard metallographic procedure. The extracted sample was mounted on a cylindrical SEM mount, stuck with super

glue, mechanically ground up to a smoothness obtained by a 1200 grit silicon carbide paper, and polished using successively 9 µm, 3 µm, and 1 µm diamond suspension.

3.2 Electron microscopy characterization

Cold-Field Emission gun (CFEG) Scanning Electron Microscopes (CFEG-SEM) SU-8230 (Figure 3.2) and cold-field emission scanning (transmission) electron microscope (CFE-S(T)EM) SU-9000, were used to scan the sample described in Section 3.1. Their characteristics and performance such as high brightness and good quality in observations at low voltage, owing to their CFEG, make them ideal for the identification of small features at nanometric scales. Some technical features are free flashing operation for up to 12 hours, no change in beam focus or alignment, and an excellent signal to noise (S/N) ratio. The properties of the gun are cold cathode, energy spread 0.2 ~ 0.3 eV, brightness 2×10^9 A/cm^2 sr, and an average of 5 nm [151].

Figure 3.2. Cold Field Emission Gun Scanning Electron Microscope (FEG-SEM).

Spatial resolution is a crucial factor in the characterization of carbides. Although a previously reported average carbide size of approximately 55 nm was documented in Section 2.3.1, a preliminary scan revealed the presence of smaller particles, with an average size of around 10 nm.

When working with BSE and X-rays mode in SEM, the resolution will be limited by the diameter of the diffusion cloud of electrons within the sample. The smallest feature that can be resolved will be in the function of the specimen geometry; crystallographic orientation with respect to the electron beam; topographic accidents, homogeneity and distribution of the highest "Z" number; and accelerating voltage [152].

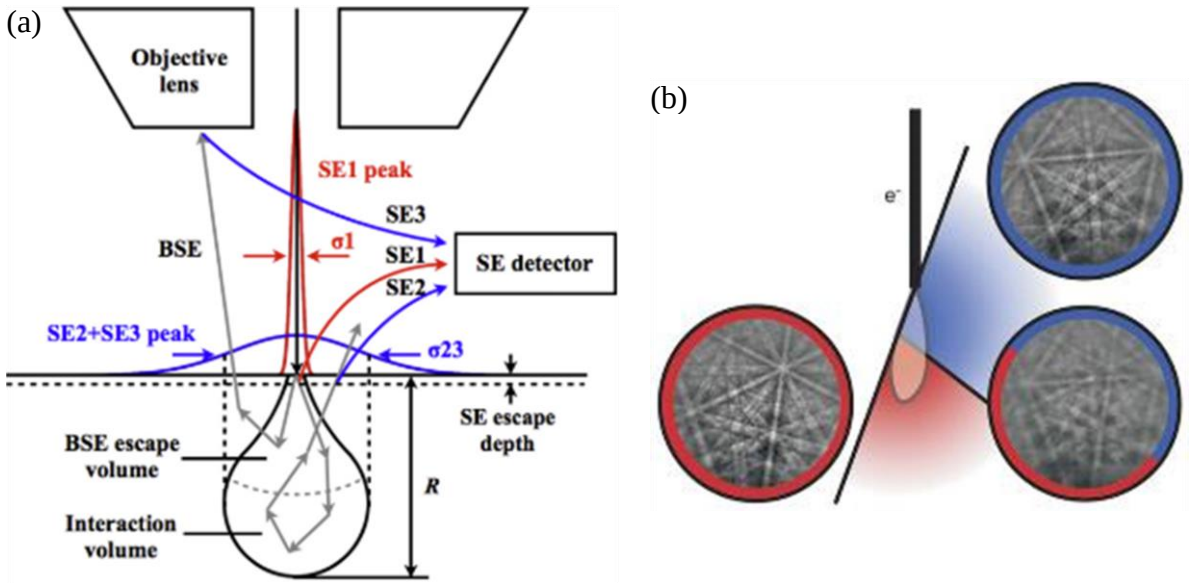

Figure 3.3 a) Diffusion and penetration of the pear-shaped cloud, as well as limits at which the BSE fraction interacts and escapes from the sample [3]. b) Change in shape of interaction in EBSD when tilted 70° [25]

There are various criteria to define resolution in ECCI and EBSD context, the resolvable feature size is determined in the sample plane and is referred to as spatial resolution [153], but so far there is no standard model to simulate or calculate it. On ideal conditions using ECCI has been reported lateral resolution of 10 – 20 nm, and an angular resolution from 5 to 10 mrad [20], with High-resolution electron backscatter diffraction (HR-EBSD), about 20 – 50 nm of spatial resolution [23] and 0.006° on the angular resolution [154]. Generally speaking, spatial resolution is the function of SEM capabilities while the angular resolution depends on the method used by the software to deconvolute the signals [152].

The ECCI resolution depends on the contrast relative to the signal background caused by the extended diffusion, and it is several orders greater than in the EBSD. The main reason that is thought for this phenomenon could be due to the differences between longitudinal resolution (Y-axis) and lateral resolution (X-axis), the former is approximately 2.5 worse than the latter. The difference arises because of the distortion of the spot size to an oval like-shape

which in turn is an effect of the tilt Figure 3.3 *b)*. In this work, the spatial resolution was measured using the SmartJ plug-in for ImageJ open-source software.

3.2.1 Electron Channeling Contrast Image (ECCI)

The photodiode BSE (PD-BSE) is a silicon detector based on ultra-shallow p^+n boron-layer photodiodes and with a segmented design. These features improve the performance of SEM systems increasing BSE signal gain at low voltages [155]. Different configurations allow filtering of a wide range of BSE energies, which can provide different information from the interaction between the electron beam and the specimen, such as topographic contrast, compositional contrast, and channeling contrast [28, 127, 155, 156]. For the ECCI scanning process, there are three possible configurations as described in the work of S. Kaboli et al. [28] as shown in Figure 3.4.

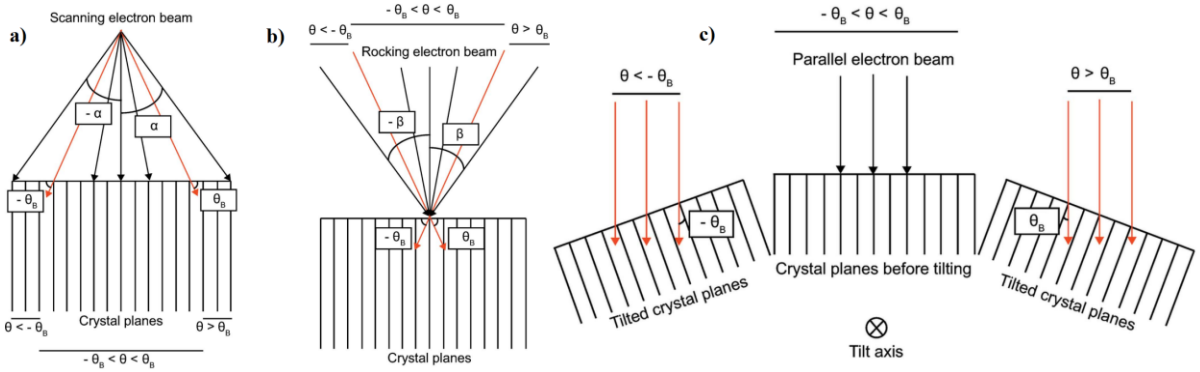

Figure 3.4. Schematics of three typical arrangements for the electron beam and crystal planes to create a channeling pattern. in a SEM using PD-BSE detector. a) A scanning electron beam at low magnifications across the specimen surface. b) A rocking electron beam at one point on the specimen surface. c) Tilted crystal planes

ECCI was performed with no tilt, which means the electron beam axis was perpendicular to the surface of interest, using the PD-BSE detector inserted below the polepiece (sample surface parallel to the detector). The channeling conditions in the current study were not under control, and the orientation of the ECCI and the alignment of the electron beam with respect to a particular lattice were not considered.

It is estimated that the BSE yield related to Electron Channeling Patterns (ECP) accounts for about 5% of the contrast in an image at 20 keV [156, 157]. Due to the dependence of the BSE emission on each of the contrast mentioned previously, the contrast shown in an image will always be accompanied by some degree of topographic contrast and compositional contrast. A BSE image (without ECC setup) could provide a better insight into compositional contrast to identify particles rich in certain elements, the higher the atomic (Z) number, the brighter it is.

The working parameters for SEM observations in the ECCI mode were PD-BSE detector for BSE images and an in-lens SE detector for SE images. Accelerating (Acc). Voltage=10 kV, and the working distance (WD) = 7mm.

3.2.2 Electron Backscattered Diffraction (EBSD)

Modern EBSD detectors typically comprise a phosphor screen, a planar scintillator, a high-sensitivity low-light level camera, detector sensors, and a lens positioned directly behind them. Additionally, forescatter detectors are often included in the setup. [7, 129, 158] (Figure 3.5). Some configurations of EBSD detectors can include CCD (charge-coupled device) chip inside the camera.

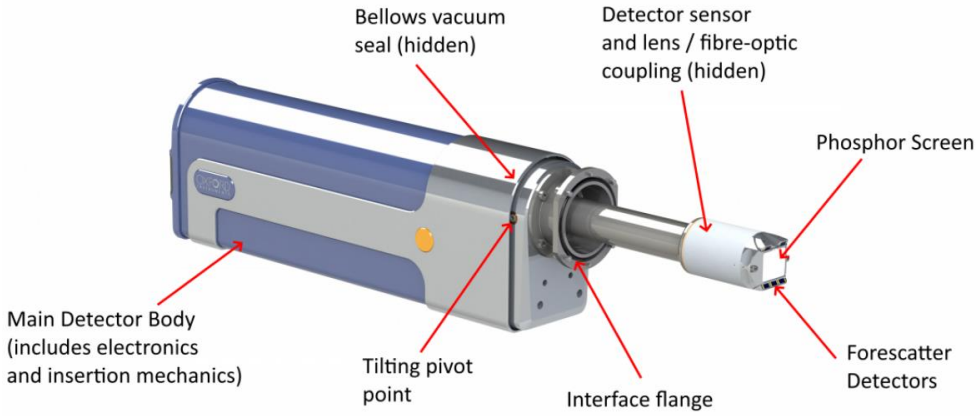

Figure 3.5. A typical EBSD detector arrowing the major components [7].

All these features are for the purpose to capture the diffracted patterns of the sample at the highest resolution, at the maximum speed, and with the highest possible fidelity, using the least amount of cache memory resources from software and hardware storage.

For EBSD mappings a Bruker eFlash EBSD camera with a CCD camera of 1600 x 1200 pixels binned at 320 x 240 for the EBSD map was used. Step size=36nm, map size=400 x 300 pixels. Acc. Voltage=20 kV, and the working distance (WD) =21mm. Imaging in color using an ARGUS detector. Indexed with Ni fcc, space group 225, a,b,c = 3.524 Å.

3.2.3 Energy Dispersive Spectroscopy (EDS)

The work to convert the energy of each photon of electromagnetic radiation characteristic of each element and transition shell into a voltage signal of proportional size is done by the EDS detector. It consists of a collimator that controls the X-ray passing to the detector, an electron trap that deflects any passing electron, the window is a barrier that keeps

the vacuum within the detector chamber, an SDD detector that converts X-rays into electrons, and FET that converts electrons into voltage output [10] (Figure 3.6).

The detector averages the number of electrons per incident X-Ray photon [10, 127]. The process in modern detectors starts when a silicon drift detector (SDD) converts each X-ray detected into an electron cloud with a charge that is proportional to the characteristic energy of that X-ray [10]. The same detector drives the formation of electron-hole pairs, and when a bias is applied, they convert into a charge pulse, then are converted to a voltage signal by the Field Effect Transistor (FET) preamplifier. Finally, the signal is further amplified and shaped to be interpreted by the software [127]. One advantage of the latest-generation EDS detectors is their ability to reduce noise, which is essential for distinguishing peak fluctuations and avoiding misinterpretations.

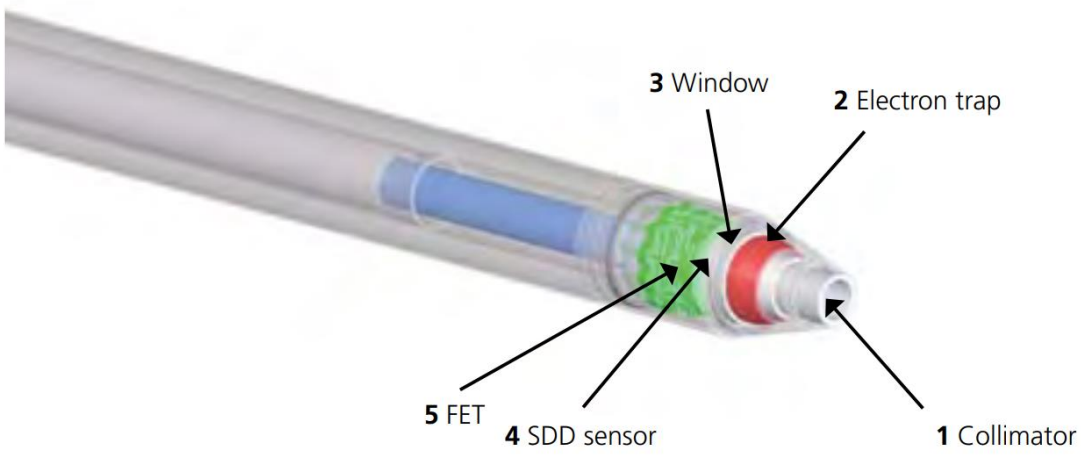

Figure 3.6 Schematic diagram of the principal parts of the EDS detector [10].

EDS map was carried out in Hitachi (CFE-S(T)EM) SU-9000. High angle in-lens BSE detector (HABSE, top detector) for BSE images, in-lens SE detector for SE images. Acc. Voltage=2 kV, the working distance (WD)=20mm. EDS detector was a windowless Oxford Instruments Extreme silicon drift detector (SDD) with a 100 mm^2 collection area.

3.2.4 Post-processing methodology

The analysis of the ECCI micrographs was made with ImageJ, open-source software for carbide identification and density measurements. The following procedure was followed [159]: i) First set scale [*Analyze → Set Scale*]; ii) Bandpass filter [*Process → FFT → Bandpass Filter*] to smooth the image and saturate particles with higher intensity for better visual contrast, and enable the software to recognize particle boundaries [160]; iii) Threshold [*Image →*

Adjust→ Threshold] to set segment the image into features of interest and background [161]; iv) Analyze particle [*Analyze → Analyze Particles*]; is a plug-in that identifies boundaries and calculates perimeter, and area (Outlines and Bare outlines); v) finally from image *(iv)* Bare outlines [*Edit → Selection → Create Selection, right click → Add to ROI manager*] and in the image *(i)* use the ROI in ROI manager for contouring the particles (Figure 3.7).

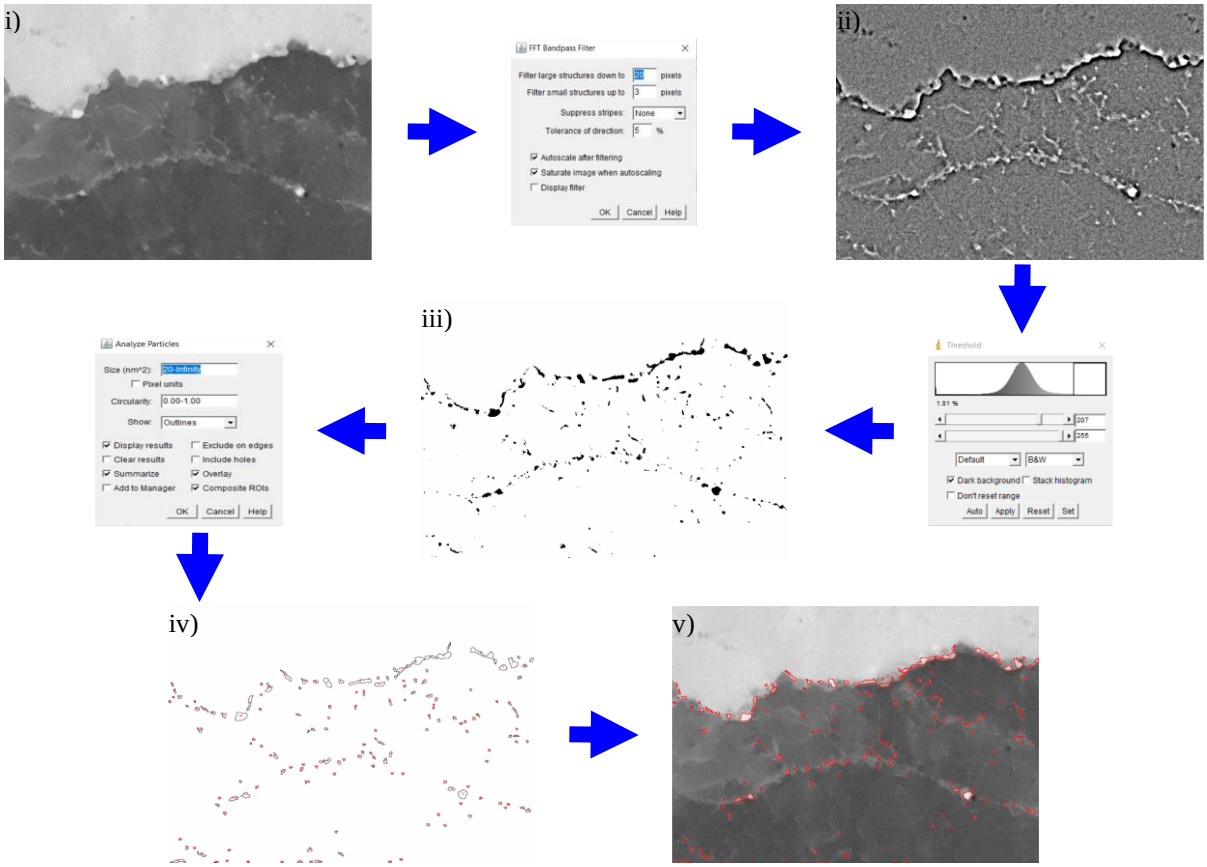

Figure 3.7 Image J process map for particles identification, from BSE-ECCI preliminary scanning.

Oxford HKL CHANNEL 5 software was used for processing Inverse Pole Figure Map (IPF), GB character map, Image Quality or Band Contrast (BC), Kernel Average Misorientation (KAM), and for taking misorientation profile lines in several points. The initial indexing rate was 92.8%, standard cleaning routine of "Noise reduction" was carried out, with a medium level of "Zero solution" and "Wild spikes" suppression, leaving only 0.29% unindexed pixels (Figure 3.8 *b)*).

Furthermore, the MTEX toolbox, an open-source code for MATLAB [162, 163], was utilized to validate certain measurements and descriptors, particularly for grain orientation analysis. Additionally, the code for processing S. Patala's GB misorientation map and its corresponding coloring scheme were employed in the analysis.

EDS post-processing was performed using Oxford's Aztec software for chemical composition spatial distribution, and element maps.

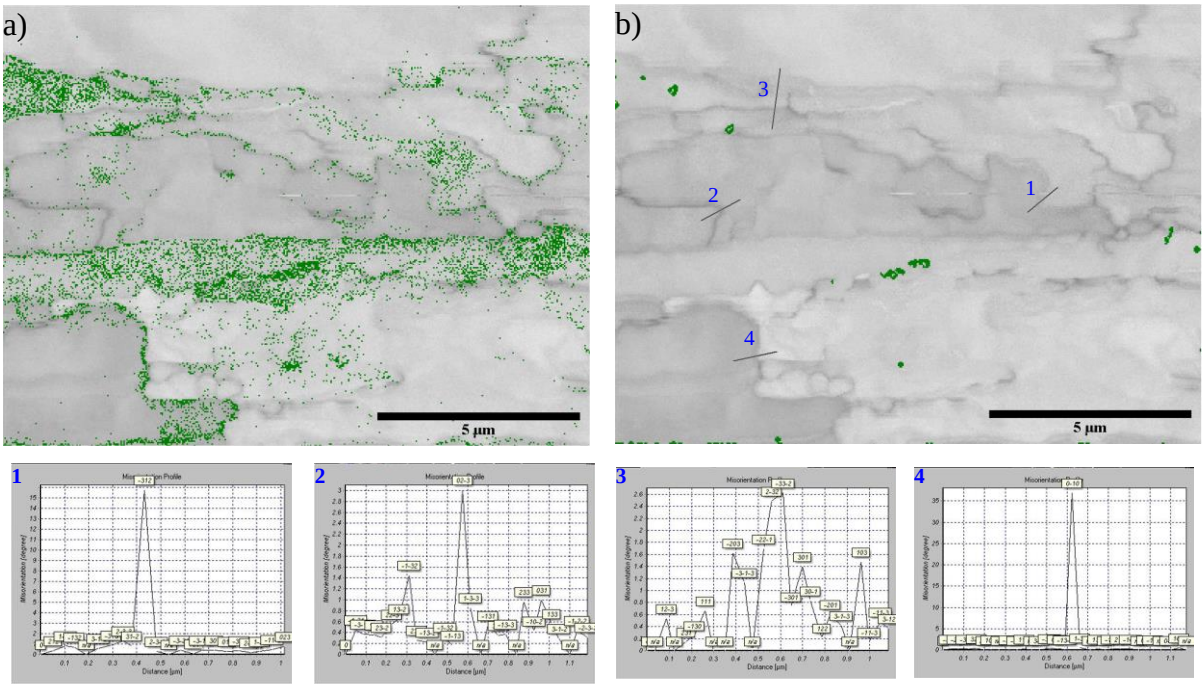

Figure 3.8 Ban contrast (BC) or Image Quality (IQ) sample measure, a) raw image green points mark unindexed pixels and b) after cleaning, with some misorientation profile lines and their respective histograms.

Chapter 4 Results and Discussion

This chapter presents the results of the characterization outlined in the previous Chapter 3 , which involved the comparison of micrographs obtained from ECCI, EBSD, EDS, and BSE-COMP - all SEM-based techniques.

In Section 4.1, the microstructure was analyzed by characterizing microstructure, GB character, elemental composition, and distribution, as well as secondary phase morphology, density, and distribution.

In this study, three regions of interest (ROI) were chosen for analysis using ECCI, EBSD, EDS, and BSE-COMP. The ROIs were named Region A (white frame), Region B (black frame), and Region C (yellow frame), and are shown in Figure 4.1, Figure 4.2, Figure 4.3, and Figure 4.5 Additionally, sub-regions A-A, B-B were magnified from ROI A and ROI B respectively, along with ROI C for a thorough analysis of carbides. Particles as small as ~10 nm were successfully detected and resolved.

In Section 4.2, the obtained results are compared and discussed in light of existing literature data, while also positing the potential relationship between preferential precipitation of carbides and cracking.

4.1 Microstructural characterization

One of the main challenges in this study was to correlate the different signals acquired from various characterization techniques. Specifically, integrating the different signals obtained from the same region was necessary to gain insight into the nature of carbides and their relationship/effect on the surrounding matrix.

To achieve this, meticulous work was conducted to identify the regions of interest (ROI) by marking reference points on the sample surface and correlating point-to-point features of interest. However, it is important to note that the physical position and orientation of the sample on each respective SEM used for scanning may result in slightly elongated or distorted features and motifs. Therefore, measurements were taken on each micrograph to obtain the most accurate data possible regarding the features under review. Figure 4.1 is the largest area taken from the sample in ECCI covering an area of 8.9 μm W × 12.7 μm L.

4.1.1 Grain morphology and crystallographic orientation.

To characterize the crystallographic orientation of the grains in the sample, the ECCI and EBSD techniques were used. Although ECCI does not provide a quantitative description

of the crystallographic texture, it is highly sensitive to small variations in the lattice orientation with respect to the normal incidence of the electron beam. As a result, ECCI offers a more accurate representation of the crystallographic orientation distribution within the sample.

Figure 4.1 displays the largest ECCI micrograph. Inside each grain, the grey level corresponds to the BSE intensity of the corresponding channeling pattern. This pattern has the same angular relationship between the electron beam and the crystal lattice orientation as the grain, resulting in crystallographic contrast. [164]

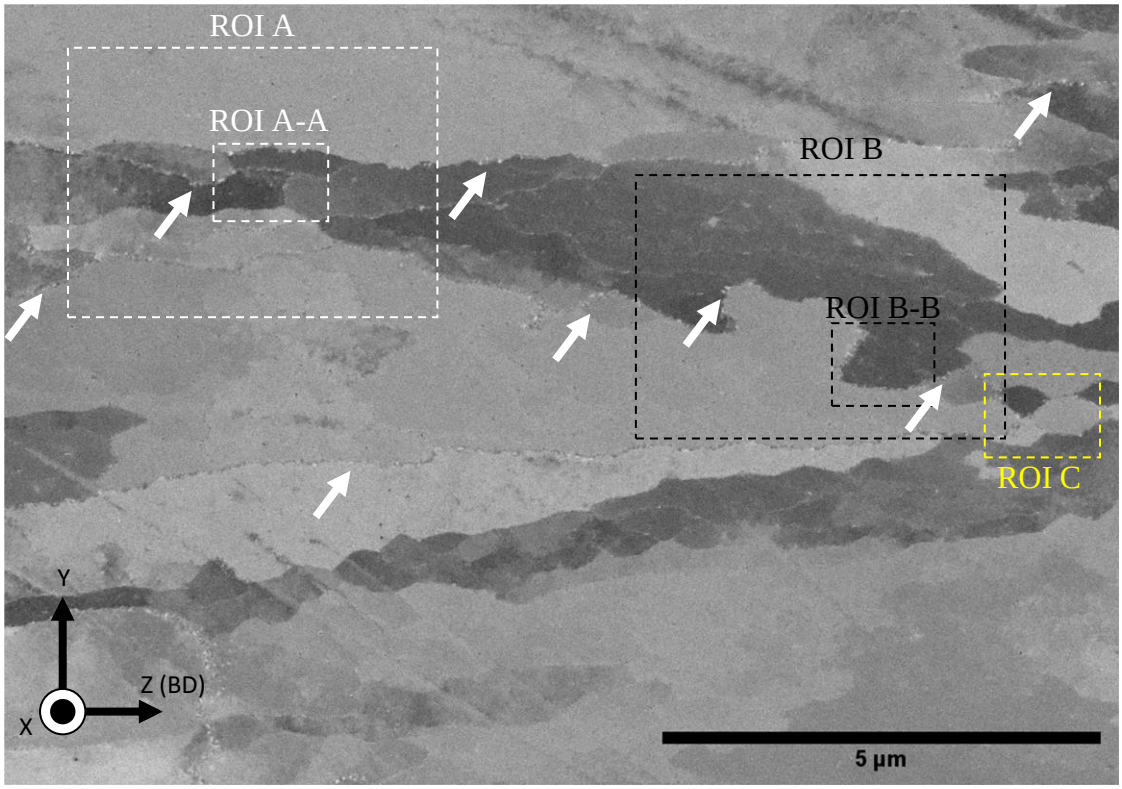

Figure 4.1 Electron channeling contrast image (ECCI), the white arrows point to chains of carbides along GBs, three regions of interest are framed.

The first notable aspect is the columnar grains with irregular shapes and with scarce fine equiaxed grains embedded within the matrix (the latter is best manifested in Figure 4.1, ROI C). The growth of the columnar grains is parallel to the building direction (BD), i.e., toward the Z direction. Similar grain morphology and growing direction have been reported in other works where LPBF Ni-based alloys were analyzed [24, 47, 53, 85, 107]. The observed variations in morphology can be attributed to the differences in the thermal gradient along the melt pool shape, which results in alterations in the solidification conditions during the AM process [80]. As a result, there is a continuous variation of G/R in the transition zone from columnar to equiaxed structure and vice versa (refer to Figure 2.5 *a)* and Figure 2.12) [86].

To corroborate the interpretation made from the ECCI micrograph, the EBSD coloring map from the same region was processed. Figure 4.2 shows crystal orientation maps with respect to the coordinated system reference frame of the sample, the *a)* IPF Y-orientation as-scanned, *b)* IPF Z-orientation as-scanned, and *d)* tilted IPF map Z-orientation. The Y direction is mostly aligned to ⟨1 0 0⟩ crystallographic direction and Z(BD) direction to ⟨1 1 0⟩ (Figure 4.2, *a)* and *b)* respectively), and this also denotes almost no crystallographic variation in epitaxial growth. Regarding this point, the scanned area is not significant enough to provide statistical information about the crystal texture, however, these data are found in the work of O. Sanchez-Mata et al. [150].

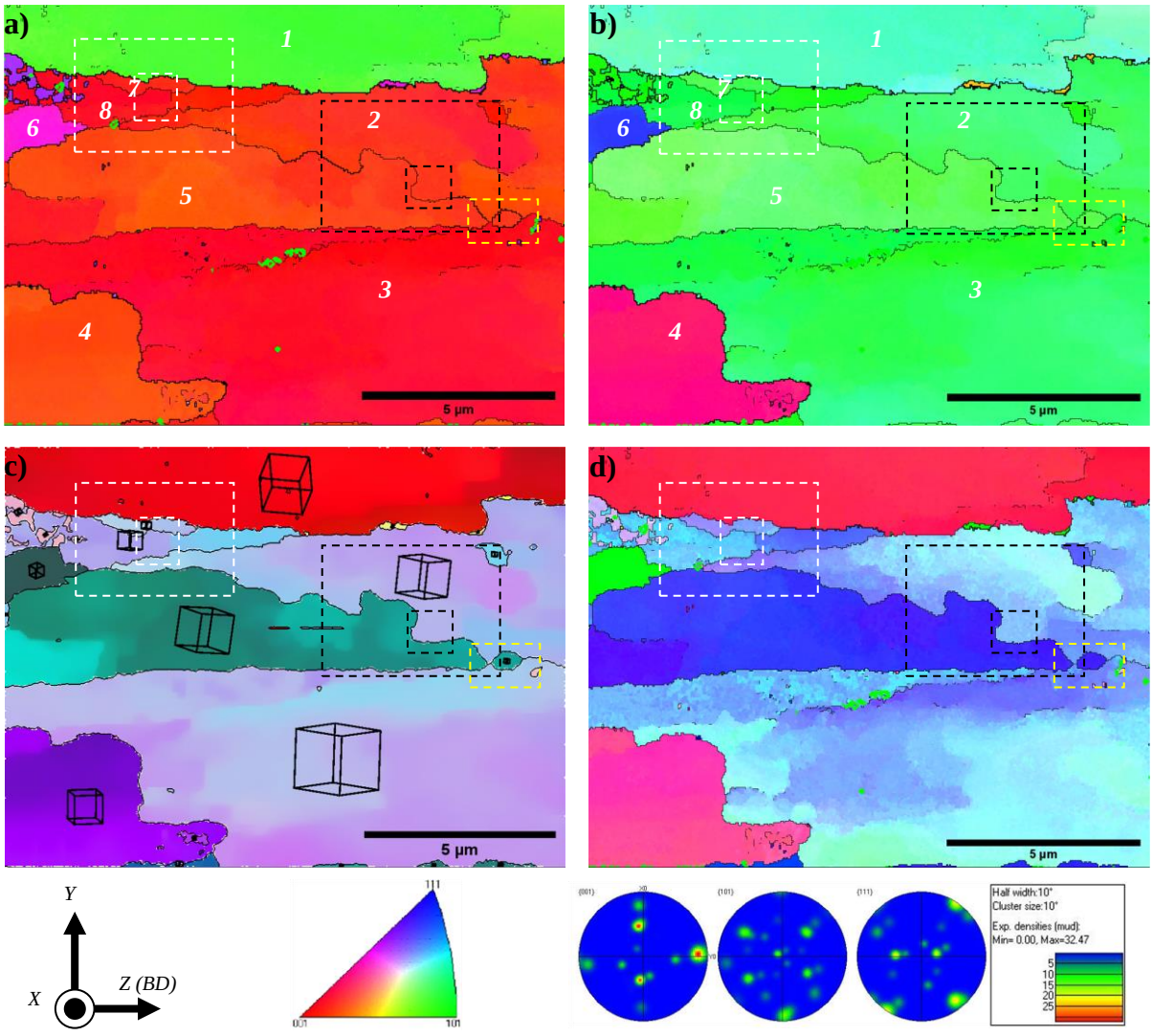

Figure 4.2. Inverse Pole Figure maps, a) IPF-Y orientation map as-scanned, b) IPF-Z orientation map as-scanned, c) sharpened IPF map with oriented crystal representation, d) IPF orientation map tilted. IPF color key triangle, and the corresponding pole figures as scanned of figures a) and b).

The highly textured systems come from the fact that each grain contains clusters of sub-grain cells with nearly the same crystallographic orientation growing through several layers of

the deposited material and in the opposite direction to the heat flux (thermal gradient direction), confirming the cumulative effect of the repetitive melting, solidifying, and reheating of the process caused by the melt pool [165].

With the color contrast orientation relative to the frame of the sample coordinate system, the morphologies of the elongated grains are not totally recognizable, since the crystal orientation distribution shows little change in the shades of color. It was necessary to delineate the GBs to correlate, to some extent, point-to-point the ECCI (Figure 4.1) and IPF maps (Figure 4.2), making the shapes and motifs of interest more distinguishable.

Although the grain morphologies in the EBSD maps resemble those in the ECCI micrograph, the crystallographic orientation is not consistent between these two signals. To further analyze small deviations in orientations, MTEX toolbox open-source code for MATLAB [162, 163] and the Oxford HKL Channel 5 software were used. In Figure 4.2 *c)* the MTEX routine is shown, which sharpens the contrast between small deviations in orientation with random colors. For larger grains with the average orientation, an extra visual help of the crystal orientation depiction is also offered.

In Figure 4.2 *d)* the HKL Channel 5 software matched the crystallographic planes identified by ECCI with respect to the incident beam. This map will be used later to perform a line for misorientation profile scan. As depicted in both maps, the enhanced hue contrast between neighboring grains confirms the variation in crystal orientation among them. These results are consistent with the observations obtained from the ECCI.

4.1.2 GB characteristics and local misorientation

The character of the GBs is dictated by the competitive growth interaction between the grains [166]. When grains of the same phase impinge with each other, the interface generated by the mismatch between the crystal orientation creates a transition region that gives characteristics that differ from the bulk crystal affecting the final properties of the solidified system [141]. The post-processing of EBSD signals enables the characterization of GB misorientation, spatial distribution, network, and density.

In Figure 4.3 *a)*, the GB misorientation and interconnected network are visible and easily identifiable from the EBSD-processed image. Graph *b)* further quantifies the GB misorientation density within the scanned area. The criteria for establishing the GB character were based on the concepts outlined in Section 2.4.8, with an additional criterion being included due to small misorientations and dislocation arrays often being associated with sub-

grains or low-angle cellular and columnar boundaries (ranging from ~2° to ~5°). As such, the criteria were defined as follows: $LAGB_1 = 2° < \theta < 5°$; $LAGB_2 = 5° < \theta < 15°$, HAGB = $\theta >$ 15° [83, 120, 156, 167-170].

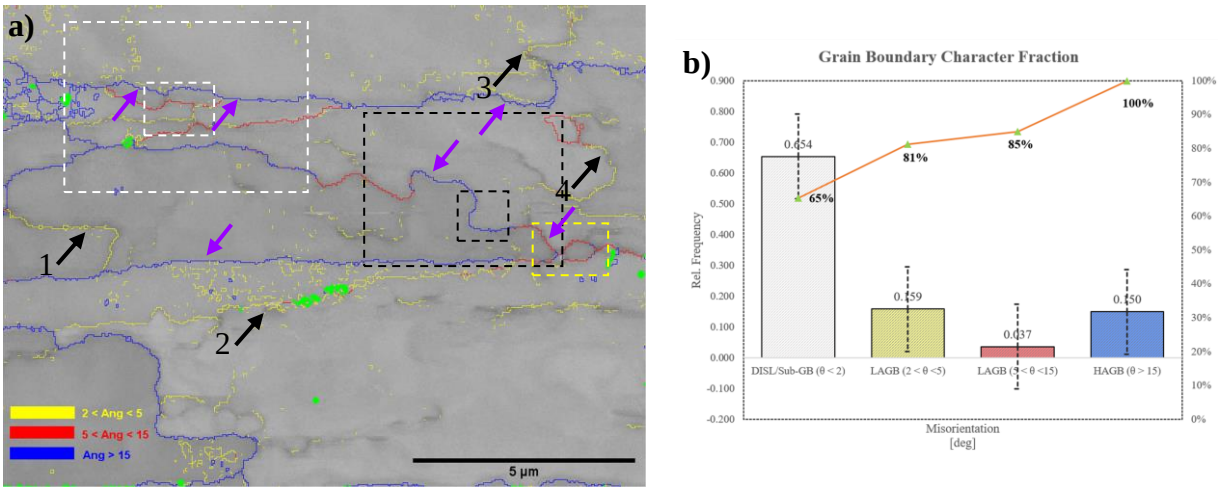

Figure 4.3. a) GB character map, b) Volume fraction graph of GB character density.

Figure 4.2 *a)* and *b)* and Figure 4.3 *a)* show labeled grains numbered 1 through 8. The color contrast in the images allows us to deduce that the misorientation interface between grains with a marked change in color hue contains a twist (***o*||*n***, rotation with respect to a common axis ***o***) component. Figure 4.3 *a)* the blue contour highlights the HAGB character, which evidenced the misorientation between grains 1 & 2, 1 & 7, 3 & 4, and 5 & 6.

An image quality (IQ) or band contrast (BC) plot is used as background in Figure 4.3, which captures perturbations caused by strain and provides small contrast variations [1]. In some instances, these regions are delineated by yellow contours implying *tilt* rotations (***o*⊥*n***) between grains, indicating the presence of sub-grain walls (pointed with black arrows), that usually are arrays of dislocations [47, 60, 83, 171].

Figure 4.4 shows GB representation proposed by S. Patala et al. (Section 2.4.8). This method is not yet widely adopted, but in conjunction with the GB character map, which provides exact ranges of GB angle misorientations, offers a comprehensive picture of the GB character. To further enhance this visualization, the MTEX toolbox provides an additional map with thicker and colored GBs.

Two important points insights can be gleaned from Figure 4.4. First, it is evident that high-angle grain boundaries (HAGBs) within the range of 35° are predominantly aligned with

three specific crystal orientations, namely [0 0 1], [1 0 1], and [1 1 2]. Second, it is worth noting that a special GB with a CSL Σ5 (36.86° / [1 0 0]) is located between grains 3 and 4.

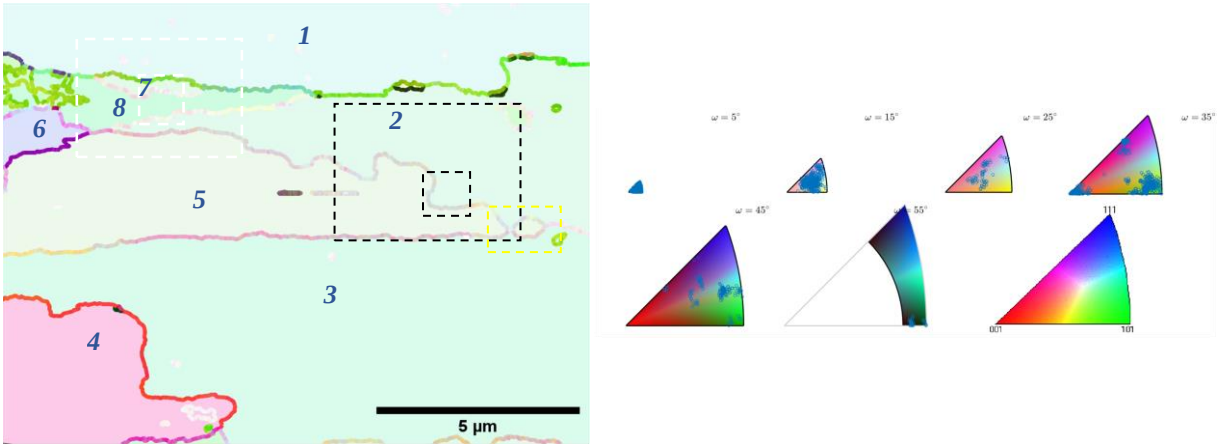

Figure 4.4 S. Patala GB misorientation map, and its respective coloring scheme for GB misorientations.

The concentrated GND found by the BC background in Figure 4.3 are believed to form due to the high thermal stress triggered by the rapid laser heating and cooling, as indicated by Minglin et al. [83]. These structures differ from those found in conventional processes since they show solute atoms and small precipitates at their walls [83]. The GBs with a misorientation of no more than 2° constitute the largest fraction of relative frequency in the system.

Utilizing KAM maps to characterize the local misorientation makes the strain induced by dislocations more apparent. Existing literature typically highlights LAGBs as regions with high dislocation concentration [60, 171]. Upon comparing Figure 4.3 *a)* and Figure 4.5 *a)*, it is evident that there is a correlation between the LAGB path and misorientation accumulation. Notably, some examples within the image are indicated by black arrows and numbered from 1 to 4 in both images.

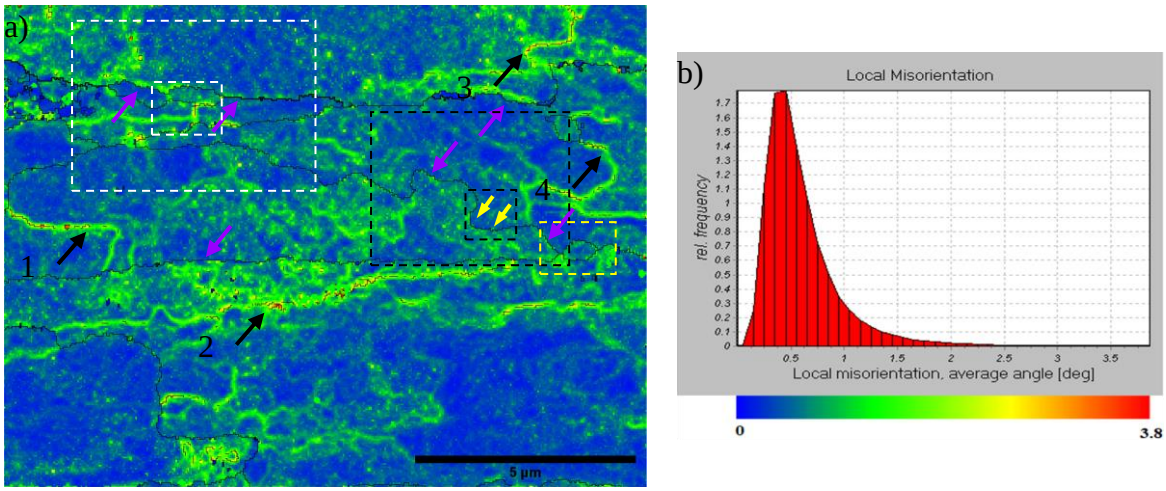

Figure 4.5. a) Local misorientation map, with a 5x5 grid pixel kernel b) corresponding histogram

In certain scenarios, the strain is asymmetrically distributed across the GB interface, indicating that dislocation accommodation is influenced by the crystal orientation, with stress being more pronounced in the direction of carbide growth. This phenomenon is illustrated in Figure 4.5 *a)*, where the purple arrows highlight such a situation.

Previous studies have examined the correlation between the special character of HAGBs and their impact on phenomena such as segregation [95], precipitation of secondary phases [58, 142, 172], and precipitate morphology [173]. In the area scanned in this work, only the GB between grains 3 and 4 (Figure 4.3 *a)*) was identified as CSL Σ5 (36.86° / [1 0 0]), indicating the absence of strain along the GB path.

One final aspect regarding GBs is their morphology. GBs with a serrated shape, depending on their energy, can affect carbide morphology and enhance the appearance of $M_{23}C_6$ carbides [174, 175]. This thus denotes a crystallographic orientation relationship (OR) between the γ matrix and the second phase [176, 177], which in turn helps to grow the carbide towards the grain of the matrix where it is incoherent.

4.1.3 Microsegregation of minor solutes

Nickel-based superalloys typically contain up to 15 alloying elements, each exhibiting distinct behavior during solidification. Moreover, the interaction between these elements leads to various outcomes that significantly impact the final properties of the solidified components. [13, 94, 178].

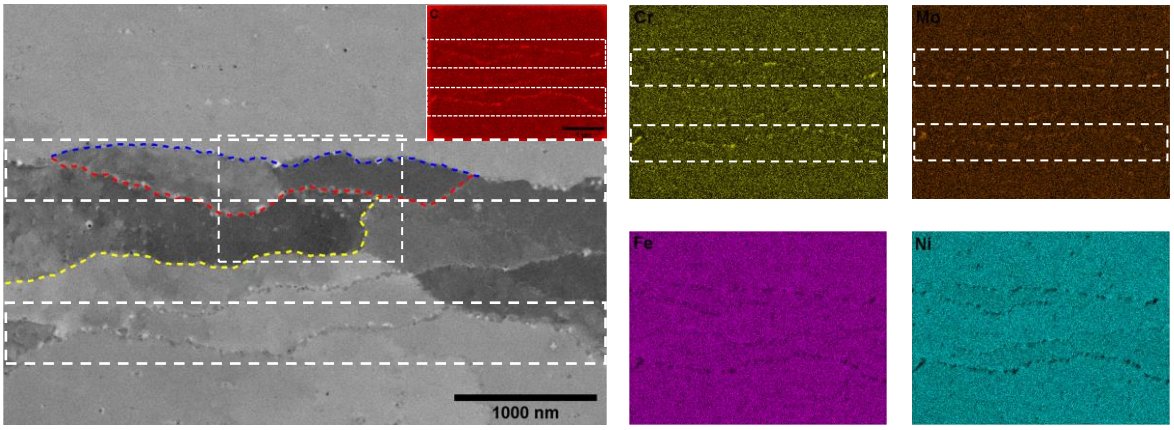

Figure 4.6 ECCI magnification of the ROI A and its correspondence EDS mapping showing C, Cr & Mo elements distribution in the area scanned, evidencing microsegregation, and a depletion of Fe and Ni. Three GBs are outlined with their respective misorientation colors according to Figure 4.3 a).

Segregation at the macroscale and microscale are phenomena that occur during solidification and are driven by different events and forces, due to the scale length at which the

events occur in AM, microsegregation is more common due to rapid cooling rates. Interestingly, the solute concentration profile only changes when solidified structure changes, if there is a reduction in the arm spacing in a dendrite structure, the profile does not change [179].

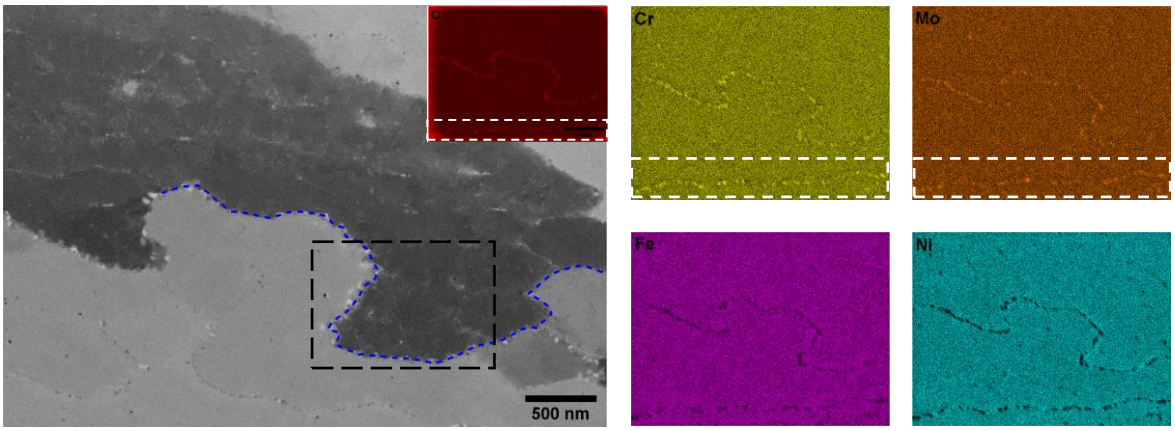

Figure 4.7 ECCI magnification of the ROI B. The correspondence EDS map shows the elemental segregation of C, Cr, & Mo, and depletion of Fe and Ni.

Figure 4.6 displays the non-uniform spatial distribution of C, Cr, Fe, Ni, and Mo. It is evident that there is a distinct elemental partitioning of C, Cr, and Mo towards the liquid zones during solidification. This is indicated by the higher concentration of these elements at GBs and interdendritic regions. These findings align with previous research in the field. [35, 46, 47, 86, 107, 180].

Correspondingly, there is a depletion of Ni and Fe at the GB. In the representative ROI A (Figure 4.6), where three different types of GB orientations are present, no clear pattern of the microsegregation of Cr and Mo in the function of the GB misorientation can be observed.

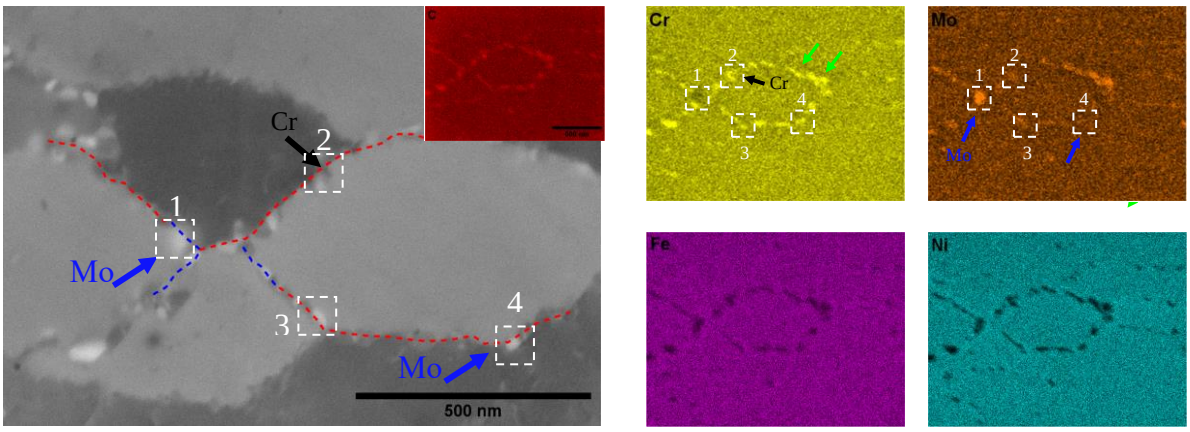

Figure 4.8 ROI C micrograph and its elemental EDS mapping. Additionally, some particles are framed, and squares 1, 2 and 4, show correspondence with the enrichment of the element of each particle.

Upon further analysis of ROI B and C (as illustrated in Figure 4.7 and Figure 4.8), it becomes apparent that both Cr and Mo exhibit a similar tendency to segregate, as observed in ROI A. The high sensitivity achieved by the EDS detection enables the identification of small variations, with the most noticeable occurring in ROI C, specifically in the area labeled as 1 (Figure 4.9 BSE-COMP micrograph of a) ROI A, b) ROI B and c) ROI C. Figure 4.9). The precipitation of a secondary phase rich in Mo leads to a depletion of Cr.

4.1.4 Characterization of carbides

Chemical composition inhomogeneities, especially at supersaturated concentrations, lead to the precipitation of secondary phases [72, 181]. Particularly for HX, in any manufacturing process, it has been found that the main secondary phases formed, just after solidification, are Mo-rich and Cr-rich carbides. These carbides frequently have the stoichiometry of M_6C and $M_{23}C_6$ respectively. In the case of AM, the rapid cooling rate in solidification produces non-equilibrium phases with a wider variety of compositions [124]. Several forms of complex carbides have been reported, and even contradicting outcomes depending on the parameters used [35], atypical configurations of $M_{12}C$ and M_nC_m have been reported [107].

Table 4.1. Sizes of carbides in Hastelloy X were reported in different investigations.

Process	Type	Location	Avg Size (nm)	Source
SLM+HIP/HT	MC-type carbide	GB	< 100	D. Tomus et al. [122]
LPBF-AB	MC-type carbide	Dendrite core	< 100	G. Marchese et al. [107]
		interdendritic region	100 - 500	
LPBF-AB	Mo-rich carbides	Cell boundary	~ 50	O. Sanchez-Mata et al. [42]
SLM-AB	Mo-rich carbides	Cell boundary (sub-GB)	75	D. Kong et al. [182]
SLM-AB	Al-Ti-O-rich Al-Cr-O-rich	Dislocation walls (<2°)	20 - 50	S. Pourbabak et al. [47]
SLM-AB	Mo-rich carbides	Cell boundary (sub-GB)	80	X. Ni et al. [124]
LPBF-AB	MC-type carbide	GB	< 500	A. S. Karapuzha et al. [24]

Figure 4.1, depicts fine, discrete bright carbides along the GBs, pointed with white arrows. This image supports the observation that these secondary phases have sub-micron dimensions [46]. LPBF technology has been shown to produce finer microstructures in

comparison to conventional processes when processing HX. Table 4.1 summarizes the key findings reported in other studies. Additional information on carbides in Ni-based superalloys is also found in Appendix A.

The size of carbides is primarily influenced by the cooling rates, which can range from 10^5 to 10^8 K/s [30, 35]. As a result, finer structural morphologies, such as cellular and columnar structures, are formed, which tend to reduce segregation [183][184]. As the cooling rate increases, a segregation-free planar structure is obtained (refer to Figure 2.12), increasing solute trapping [30].

Overall, the observations from Figure 4.1 and the literature review suggest that LPBF technology is capable of producing finer microstructures in HX Ni-based superalloys, which are characterized by a lower degree of segregation. The size of carbides in these alloys is closely related to the cooling rates during the LPBF process, which can be controlled to achieve desirable microstructures.

The ECCI micrograph does not allow for establishing the composition of the carbides, since the purpose of this technique is to filter the BSEs that contain energy related to channeling behavior. For an assessment that indicates the brightness as a function of increasing Z number, a backscattered electron compositional (BSE-COMP) characterization is helpful.

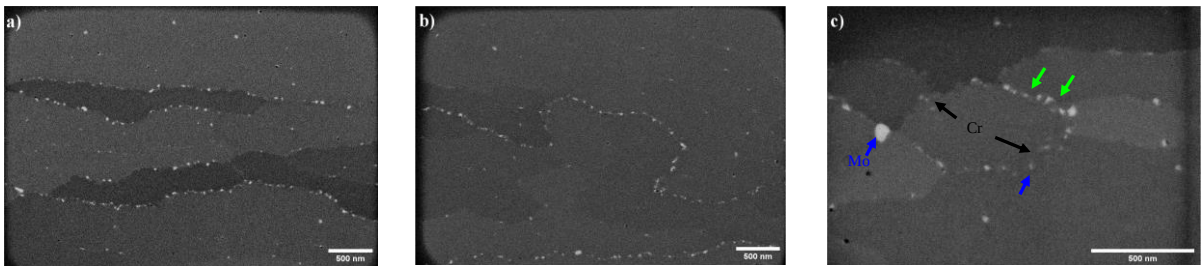

Figure 4.9 BSE-COMP micrograph of a) ROI A, b) ROI B and c) ROI C.

BSE-COMP exhibits a compositional contrast that enables the qualitative analysis of carbide composition. This feature has been utilized in previous studies to establish that brighter particles contain a significant concentration of higher atomic number elements, while darker particles are rich in lighter atomic number elements. When used in conjunction with other characterization techniques, BSE-COMP can provide valuable insights into the composition of carbides in materials. [16, 185]. Figure 4.9 shows a high number of bright particles, which can be assumed to be Mo-rich M_6C carbides. Similar findings have been reported in [124, 182].

Due to the limited magnification resolution in Figure 4.9 *a)* and *b)* , the elemental composition of the carbides cannot be determined accurately. Therefore, a detailed analysis of

these regions is necessary. Figure 4.9 *c)* offers a clearer understanding of the composition of the carbides based on their brightness in Region of Interest (ROI) C. Mo-rich carbides are brighter than Cr-rich carbides, which confirms the concentration of the elements shown in Figure 4.8. An interesting particularity is the chain of carbides that intercalates Cr-rich and Mo-rich carbides in Figure 4.9 *c)* (green arrows). In this case, the conditions used in the EDS characterization were not able to deconvolute correctly the overlapping signals of both elements.

Table 4.2 Quantification of precipitates Cr-rich and Mo-rich from BSE-COMP images in Figure 4.9.

	GB Character	No. Part	Distance (nm)	Σ Diam eq. (nm)	Avg. size (nm)	Part. Density (No. Part*nm-1)	Linear Density (nm*nm-1)
ROI A	HAGB	28	3,079	556	19.86	0.0091	0.181
	$LAGB_2$	27	3,226	743	28.56	0.0084	0.230
	$LAGB_1$	9	2,845	145	16.14	0.0032	0.051
ROI B	HAGB	49	5,937	1,503	30.67	0.0083	0.253
ROI C	$LAGB_2$	18	1,514	339	18.86	0.0119	0.224

With the information obtained from Figure 4.9, the densities of carbides at GB were calculated, regardless of their composition, using the approach that has been set out by R. G. Byrne et al. [159] to detect precipitates in an image. A summary of the findings is presented in Table 4.2. The most striking observation is the lower density of precipitates at angles below 5°.

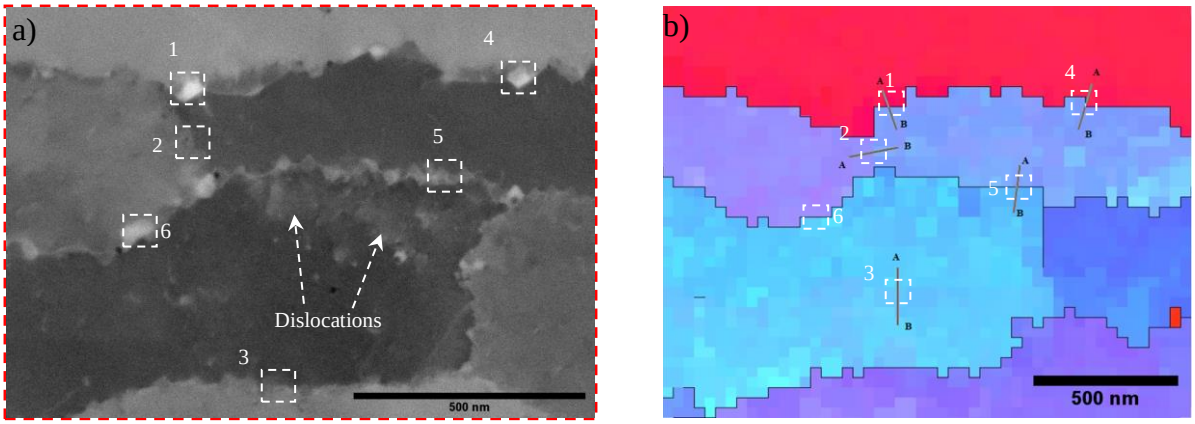

Figure 4.10 a) ×100k magnification ROI A-A and its respective b) IPF Z map, with profile misorientation lines.

Figure 4.10 *a)* shows a magnified view of ROI A-A, where the carbides exhibit a more defined morphology. Specifically, carbides 1 and 4 have a blocky shape with a faceted side, suggesting the possibility of a special crystallographic OR between the γ matrix and the carbide [176]. Further analysis with TEM will be helpful to identify this relationship.

When comparing micrograph Figure 4.10 *a)* with Figure 4.9 *a)*, it is plausible to notice that some Mo-rich carbides are hidden in the ECCI image, this is because their crystal orientation does not match with the Bragg condition with respect to the electron beam.

A misorientation profile was carried out for sites from 1 to 6 (Figure 4.10 *b)*) and the results are shown in Table 4.3. Correlating the results obtained from EDS elemental map (Figure 4.6) and the BSE-COMP (Figure 4.9 *a)*), the largest carbides labeled 1 and 4 present characteristics of Mo-rich carbides, the additional features that the misorientation profile provides is that HAGBs facilitate the formation of these carbides [142, 176].

In the case of sites 2 and 3, no precipitation is observed. Site 5, on the other hand, shows a concentration of dislocations, which is revealed by a subtle contrast in the channeling image [134]. The EDS map confirms the presence of Mo solutes, while the BSE-COMP image (Figure 4.9 *a)*) depicts carbides that were not completely revealed by ECCI.

Table 4.3 Boundary misorientation profiles from points marked in ROI A-A (Figure 4.10), ROI B-B (Figure 4.11), and ROI C (Figure 4.12)

	Point	**Misorientation (°)**	**Mis. Axis**
ROI A-A	1	38.96	⟨3 2 0⟩
	2	2.50	⟨0 3 1⟩
	3	2.73	⟨2 -2 3⟩
	4	39.69	⟨3 3 -1⟩
	5	6.59	⟨-1 3 -2⟩
	6	8.64	⟨-1 3 -1⟩
ROI B-B	1	16.45	⟨-3 1 2⟩
	2	16.12	⟨-3 1 2⟩
	3	12.55	⟨-3 1 2⟩
ROI C	1	15.17	⟨1 3 -2⟩
	2	14.02	⟨1 3 -2⟩
	3	15.43	⟨2 4 -1⟩
	4	13.94	⟨2 4 -1⟩

It is also noteworthy that there is a serrated shape along the GB between carbides 1 and 4. Although the appearance of this shape is typically associated with a controlled cooling (0.68 and 3.53 °Cs^{-1}) after solvus solution HT (~1100 °C) [175, 186-188], it has also been observed that serration occurs at HAGBs [187, 189], which is consistent with this observation.

Carbides 1 and 4 exhibit a prominent growth direction towards one side of the GB, which supports two aspects previously established. First, the facet sides have an OR with the grain where they are located, which results in the growth towards the grain without the OR. This growth behavior is confirmed by Figure 4.5 *a)* in ROI A-A, which shows the local misorientation concentrated at the grain where the carbide grows, thus corroborating the strain induced by the carbide growth.

ROI B-B is depicted in Figure 4.11 *a)*, revealing a GB mainly with a high-angle misorientation between two grains. The GB is decorated with entangled particles of different gray scales, as indicated by the black arrows. Additionally, particles of different shades of gray are noticeable (green arrows), with the brighter ones assumed to be M_6C Mo-rich carbides and the darker ones presumably $M_{23}C_6$ Cr-rich carbides. The BSE-COMP image (Figure 4.9 *b)*), supports the inference that the bright particles are Mo-rich carbides since they are dispersed and discrete. On the other hand, it has been reported that Cr-rich carbides appear contiguously to Mo-rich carbides in Ni-based superalloys [17, 46, 105], regardless of the manufacturing process.

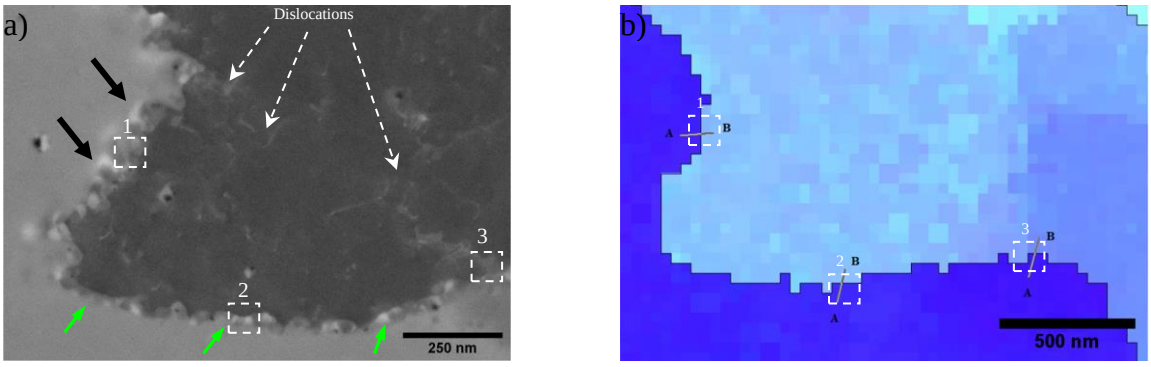

Figure 4.11 a) Magnification of Sub-ROI B, ×100k magnification over GB with coarse carbides visible. Magnification from the EBSD characterization b) local misorientation map.

In Figure 4.11 *a)*, dislocations can be observed on the core of the darker grain, which is in harmony with the strain detected by the KAM map (Figure 4.5 *a)*). Further evidence that the various grayscale patterns are unrelated to strain perturbations is provided by the yellow arrows in the KAM map, which show that there are no dislocations along the path of GB.

In a similar manner to ROI A-A, line scans were conducted in Figure 4.11 *b)*, to obtain the misorientation profile of some random points, and the measures obtained were included in Table 4.3 The HAGB measurements in ROI B-B show similarities with $LAGB_2$ of ROI A-A, suggesting that the precipitation is to some extent dependent on the GB character and the preferential appearance starts about 8°-12°. One additional point to highlight is the presence of irregular shapes, indicated with black arrows, that are probably clusters of Mo-rich solutes, rather than precipitates.

The presence of C, Cr, and Mo in the area of interest was confirmed by the corresponding EDS maps (Figure 4.7). Similar to ROI A-A, a co-segregation of these solutes can be observed, providing further evidence that small Mo-rich and Cr-rich carbides are roughly alternated along the GB. This observation is supported by the ECCI micrograph shown in (Figure 4.11 *a)*), which also reveals the presence of fine carbides in different shades of gray along the GB.

ROI C was previously analyzed from the point of view of the ECCI and EDS, which in turn have the best resolution achieved in this study on both techniques. Figure 4.12 and Table 4.3 provide additional information from the misorientation profile. The misorientation profile shows that the region contains a mixture of $LAGB_2$ and HAGBs, indicating that precipitation occurs in both types of boundaries.

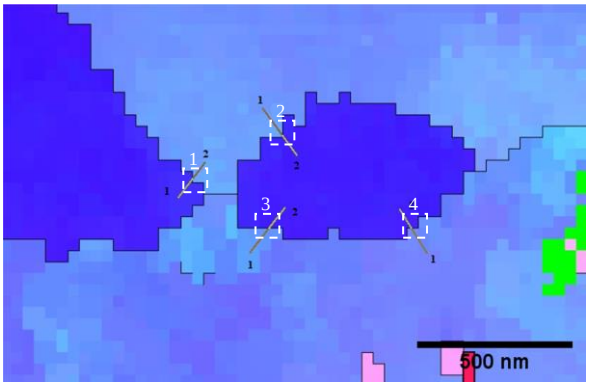

Figure 4.12 a) IPF Z map, with profile misorientation lines ROI C. Same area as Figure 4.8.

In Figure 4.8, the dotted frames 1, 3, and 4 identify clusters rich in Mo, with the additional evidence from Figure 4.9 *c)*, the assumption of Mo-rich carbides is corroborated. Nevertheless, the EDS map cannot deconvolute some element signals, and in frame 4, the Mo-rich carbide seems to be surrounded by Cr, for that reason the colored elemental is stronger

than the Mo signal. On the other hand, dotted frame 2 shows particles rich in Cr, in the BSE-COMP image it is possible to visualize a small dot surrounded by a darker halo.

By returning to frame 1, and comparing EDS maps for Cr and Mo, it is possible to corroborate a higher concentration of Mo, with a depletion in Cr. M.M. Tavakkoli et.al [100] have suggested that up to 6.7 wt. % of Mo in as-cast Ni-superalloys, a reduction in the segregation behavior of Cr and Si is occurring and can even change the direction of segregation. Another possible implication of the large size of carbides in GBs that are barely above 15° is their proximity to triple junctions. This has been reported as a factor that leads to preferential nucleation due to the high energy of the triple junction compared to that of a single GB [58, 187].

Local misorientation (Figure 4.5 *a)*) seems to develop in the direction of cluster segregation or carbides growth. Another feature is the planar GB shape compared to other GBs.

4.2 Discussion

The purpose of this study is to comprehensively investigate the characteristics of carbides from multiple perspectives. The formation of secondary phases at interdendritic and intergranular regions is a multi-factorial phenomenon. Therefore, this research aims to understand the underlying mechanisms that drive the formation of these carbides during the early stages of solidification and their subsequent interactions with the alloy system.

4.2.1 Microsegregation in the LPBF and its dependency on crystal orientation

Microsegregation is a common form of small-scale segregation that occurs during the solidification of metallic alloys. It arises from the partitioning of solute atoms in different proportions between the solid and liquid phases, resulting in compositional inhomogeneities at the interdendritic regions that solidify last [179].

Microsegregation can have a beneficial or detrimental effect on alloys. B. Lezzar et al. [95], indicate, that in FCC polycrystal materials, the solute atoms with larger atomic diameters than the matrix atoms stabilize the GB interfaces by reducing the free energy. On the other side M. A. Gibson and A. Schuh [190], developed a model to explain that deleterious elements, when segregated, reduce the GB cohesion, causing a chain detachment.

Certain elements, such as Mo, W, C, and Si, have a high tendency to segregate [107, 191]. However, microsegregation behavior is influenced by a multitude of factors including manufacturing process parameters [181, 183]; raw material chemical composition [44, 192]; heat treatment history [193, 194]; the morphology and direction of liquid channels [195]; interface energy [196, 197]; and interplay with other alloys within the system [75, 100, 178], among others.

In addition to the aforementioned factors, solute accommodation in metallic alloys during conventional manufacturing processes is also influenced by crystal orientation and the distance from the core center of the grain cell. The latter implies that as the material solidifies around the center of a columnar grain cross-section, the surrounding bulk experiences changes in elemental composition as it moves away from this center. These observations have been reported in several studies. [77, 198-200]. Indeed, constitutional cooling due to solute segregation plays a significant role in shaping the cruciform morphology of the transverse section of dendrites.

One of the unique characteristics of LPBF is the tendency to align cellular structures with nearly the same crystallographic orientation. Furthermore, some events and driving forces

are amplified due to the operating conditions of the AM processes [76]. As a result, it is natural to expect that microsegregation as the function of crystal orientation is present in LPBF, and it has a significant preponderance on the final properties of the solidified component.

Figure 4.2 *b)* shows that the IPF maps are primarily dominated by a crystallographic direction ⟨1 1 0⟩ aligned along the Z-axis (BD), with a {1 1 0} plane also roughly oriented along the Z-axis. Additionally, Figure 4.2 *a*), indicates that the ⟨1 0 0⟩ direction is aligned with the Y-axis, which is orthogonal to the Z-axis. This crystal configuration indicates that the segregation direction for grains labeled 2, 3, and 5 are roughly aligned with [0 0 1] and [0 0 -1].

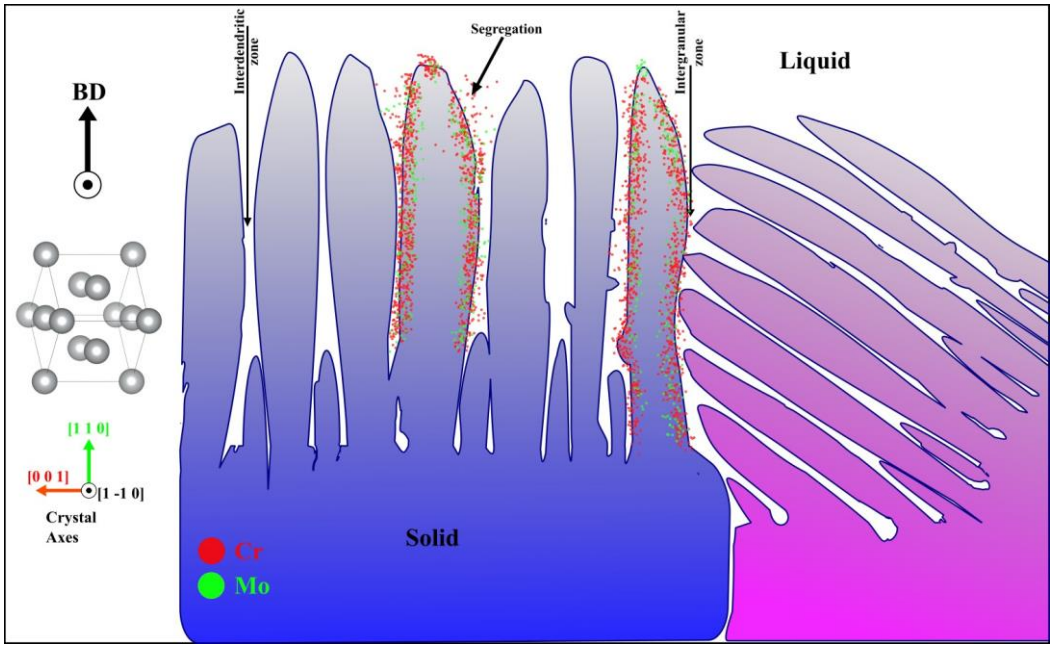

Figure 4.13 Schematic representation of preferential segregation of Cr and Mo as a function of crystal orientation. Columnar growth with a high degree of texture is a common phenomenon in LPBF due to the rapid cooling rates, which leads to microsegregation occurring at interdendritic and intergranular regions[4]

In section 4.1.3 it was noted that segregation did not appear to follow a clear pattern in relation to GB character as has been reported in other studies [58, 95, 176]. However, a clear segregation trend is observed in the micrographs presented in Figure 4.6, and Figure 4.7, where some boundaries are nearly parallel to the BD direction. Figure 4.13 shows the schema of segregation behavior of Cr and Mo. Grain blue represents the crystal orientation ⟨1 1 0⟩ aligned to the BD direction.

This microsegregation makes more sense when viewed from a crystallographic perspective. F. Wang et al. [77] have documented a preference of Cr and Mo to distribute uniformly in the periphery of dendrites along the [1 0 0] orientation, but an inhomogeneous distribution along the [1 1 0] orientation in cast Ni-based superalloys.

Although the dendritic structure is replaced by a columnar structure in LPBF due to the high cooling rates, the elemental distribution is anticipated to remain unchanged. In contrast to the work of F. Wang, the evidence presented in this study clearly shows segregation at GBs and cellular boundaries. This indicates that there may be other factors at play that influence the partition coefficients of Cr and Mo, leading to different distribution patterns [196].

4.2.2 Effects of GBs on carbide precipitation in LPBF

The impact of GBs on segregation and precipitation has been the subject of numerous investigations, largely due to the correlation between GB misorientation and interfacial energy. In this context, it is necessary to view GBs as zones that facilitate the thermodynamic kinetics of carbides. This approach has been proposed by Trillo et al. [191], who emphasized that the GB interfacial energy plays a critical role in the preferential development of carbides, rather than the mere disorientation of the GBs.

By characterizing GB misorientation, it is possible to obtain an indicator of the interfacial energy between grains. Based on the information provided in Table 4.2, it is possible to make assumptions about the interfacial energy at which carbides precipitate preferentially, taking into account their average size, particle, and linear density. The results indicate the misorientation related to the interfacial energy threshold at which carbides preferentially precipitate is above 5°.

However, the conventional approach of dividing the range of misorientations into discrete and finite categories, such as LAGB, HAGB, and CSL, which are used to encompass and average disorientation, may not provide a complete description of GB misorientation character. Therefore, individual line scans were conducted, and a GB misorientation map with a continuous variation representation was processed to gain a better understanding of the misorientation behavior.

After conducting individual line scans (Table 4.3), two important findings emerged. Firstly, it was observed that a misorientation of around 40° provides a favorable site for carbide development, as shown in Table 4.3, which is consistent with the observations made by B. Tang et al. [172]. Secondly, the precipitation of intergranular carbides is inhibited or delayed at LAGB angles below 5°, which is also supported by existing literature [142, 201].

Nevertheless, the GB continuous misorientation representation of the S.Patala map (Figure 4.4) hints that the degree of interfacial elemental saturation is more closely related to the proportion of high-energy atomic sites in a GB rather than its average energy, which in turn

influences the precipitation, as noted by A. Gupta et al. [196]. This observation derives from the continuous change in color tone and shading, coupled with the distribution of carbides.

One more highlight is the GB morphology; B. Tang et al. [172], observed dependence in the formation of GB serration shape, accompanied by intergranular $M_{23}C_6$ carbides in Ni-Cr-W superalloys. Previously, it was believed that nucleation and subsequent carbide growth were the primary factors responsible for this morphology. However, more recent studies have revealed that the formation of this morphology is actually influenced by thermal conditions [187]. According to experiments carried out by H.U. Hong et al. [174] on Nimonic 263, after some HTs, the shape was found to precede the precipitation.

The serrated GB morphology is frequently observed in Ni-based superalloys and is due to the anisotropic elastic properties of nickel (coherency strains between both γ and γ' phases, the latter when present), this morphology has been found to contain large quantities of Mo and Cr [202]. The importance of the serrated shape is its association with a lower rate of crack propagation through the modification of carbide characteristics and resistant to intergranular damage mechanisms.

4.2.3 Effects of the GB carbide characteristics on the matrix

Precipitation, like microsegregation, is a phenomenon that depends on multiple events. It starts with the fact that precipitation is a direct consequence of microsegregation. However, the mechanism of preferential nucleation of a specific type of MC carbide is not yet clear. Since M_6C carbides have been identified as a factor in cracking nucleation, this study analyzes the elements that facilitate their appearance.

Based on the HX-TTT diagram (Figure 2.10), it can be inferred that M_6C carbides have a greater tendency to form at medium-high temperatures, within the designed range, and during the final stages of solidification, compared to $M_{23}C_6$ carbides. This suggests that the kinetics of precipitation for M_6C are faster than those of $M_{23}C_6$ under such conditions. It is worth noting that in some studies involving additive manufacturing of HX, no Cr-rich carbides were detected [115, 203].

The above is relevant since the coarsening, stabilization, and dissolution of carbides in HX are controlled by heat treatments. In the case of LPBF is particularly crucial, as the continuous thermal cycles that the component undergoes until its completion can promote the appearance and growth of carbides in the solid-state of the deposited layers. This observation has been raised by Marchese et al. [107].

L. R. Liu et al. [197], have identified two types of M_6C carbides in Ni-based superalloys, namely $(M_6C)_1$ and $(M_6C)_2$. The former decomposes from MC carbides during high temperatures (t > 871 °C), while the latter segregates directly from the matrix. The former is detrimental to the solidified system due to irregular ORs with the matrix, which reduce the bonding force between the matrix and $(M_6C)_1$. It is important to note that no cracks were found in the sample studied, which suggests that either no decomposed M_6C carbides nucleated, or the matrix/carbide OR is not present in this alloy/process.

It has also been discovered that M_6C can decompose into $M_{23}C_6$ in Ni-based alloys, as observed by G. Bai et al. [105]. This decomposition occurs at temperatures ranging from 650 to 1000 °C, particularly when there is a high concentration of Cr present surrounding the M6C carbide during the decomposition of Mo-rich carbides. In the current study decomposition from M_6C to $M_{23}C_6$ may not have taken place or occurred at a low scale due to insufficient time. Nevertheless, another important observation from the work of G. Bai is the crucial role that Cr plays in the stability of M_6C carbides. Given the evidence from ECCI, EDS, and BSE-COMP, where is shown the M_6C carbides surrounded by Cr, and a few $M_{23}C_6$ in some cases, is more likely to this mechanism is acting here.

Another aspect, also related to temperature, is the carbide morphology. The morphology of carbides is also linked to thermal regimes. For instance, the development of low-melting C-rich and Mo-rich liquid films is associated with a significant increase in the solidification interval ΔT [203]. The formation of carbide films can be particularly harmful to the stress-rupture resistance of the material [175]. The parameters used in this printing demonstrate to be adequate to avoid the formation of film-like carbides, as BSE-COMP and ECCI images show discrete and dispersed carbides.

Based on previous observations, it can be inferred that the GB character provides the energy and supersaturated environment for the secondary phase to precipitate. The crystallographic orientation of channels, on the other hand, expels solutes in a preferred direction from the core into liquid channels and provides an anchoring point for stable precipitates to form.

The analysis of previous investigations (Appendix A) has revealed that several precipitate/matrix ORs have a crystal direction relationship with the matrix grain of ⟨1 0 0⟩, for both M_6C and $M_{23}C_6$. This implies that there is directional accommodation between the secondary phase and the matrix.

Furthermore, the interaction between carbides and segregation plays a crucial role in enhancing the cohesion of grain boundaries. The effective pinning of GB by stable and fine Mo-rich particles distributed throughout the GBs results in higher GB strength [204].

Chapter 5 Conclusions and summary

A comprehensive study of the crack-free HX-LPBF-AB sample was carried out using ECCI, EBSD, BSE-COMP, and EDS characterization, the findings allow the author to elaborate on the nature of the segregation and precipitation in GB, and what is their role in terms of failure in form of cracking within the HX solid system. The following key points can be extracted from the findings presented in this thesis:

- ECCI and EBSD have shown effectiveness in characterizing nanoparticles at GB, overcoming technical issues.
- There is a correlation between the preferred microsegregation of solutes (Cr, and Mo) and the ⟨1 0 0⟩ crystallographic direction.
- Carbide precipitation is faster in GB with a misorientation between adjoining grains of more than 5°, and it is confirmed that precipitation of carbides is inhibited on GB misorientation below 5°.
- The kinetics of M_6C are faster than $M_{23}C_6$ carbides during the solidification stage.
- The presence of discrete and finite Mo-rich carbides dispersed along grain boundaries suggests either suppression or low-scale activation of the carbide decomposition mechanism.
- Microsegregation, GB morphology and carbide interaction play a crucial role in GB stabilization and cohesion, thereby inhibiting cracking, irrespective of the presence of M_6C carbides.

Chapter 6 References

[1] S. I. Wright and M. M. Nowell, "EBSD Image Quality Mapping," *Microscopy and Microanalysis*, vol. 12, no. 1, pp. 72-84, 2006, doi: 10.1017/S1431927606060090.

[2] K. Momma and F. Izumi, "VESTA 3 for three-dimensional visualization of crystal, volumetric and morphology data," *Journal of Applied Crystallography*, vol. 44, no. 6, pp. 1272-1276, 2011, doi: doi:10.1107/S0021889811038970.

[3] M. Suga *et al.*, "Recent progress in scanning electron microscopy for the characterization of fine structural details of nano materials," *Progress in Solid State Chemistry*, vol. 42, no. 1, pp. 1-21, 2014/05/01/ 2014, doi: https://doi.org/10.1016/j.progsolidstchem.2014.02.001.

[4] *Inkscape*. (2022). [Online]. Available: https://inkscape.org/?about-screen=1

[5] J. F. Nye, *Physical properties of crystals : their representation by tensors and matrices*, Repr. with corrections and new material. ed. (Oxford science publications). Oxford: Clarendon (in Inglés), 1985.

[6] W. D. Callister, *Fundamentals of materials science and engineering*. Wiley London, 2000.

[7] M. C. Ltd. "Electron Backscatter Diffraction (EBSD) Detectors." Oxford Instruments. https://www.ebsd.com/ebsd-techniques/ebsd-detectors (accessed.

[8] R. Hielscher. "Kernel Average Misorientation (KAM)." https://mtex-toolbox.github.io/EBSDKAM.html (accessed 01/03, 2022).

[9] L. HANLOO CO. "Effect of solidification parameters on Microstructure of cast chromium alloy." https://www.zhycasting.com/effect-of-solidification-parameters-on-microstructure-of-cast-chromium-alloy/ (accessed.

[10] Oxford Instruments plc. *Silicon Drift Detectors Explained*, OINA/SDDExplained/0212, 2012. [Online]. Available: https://nano.oxinst.com/assets/uploads/products/nanoanalysis/documents/Brochures/SDD%20Explained.pdf.

[11] H. Oxford Instruments, "Channel 5," *Oxford Instruments HKL, Majsmarken*, vol. 1, p. 9500, 2007.

[12] S. Suwas and R. J. Vikram, "Texture Evolution in Metallic Materials During Additive Manufacturing: A Review," *Transactions of the Indian National Academy of Engineering*, vol. 6, 10/18 2021, doi: 10.1007/s41403-021-00271-6.

[13] J. R. Davis and A. S. M. I. H. Committee, *Nickel, cobalt, and their alloys* (ASM specialty handbook). Materials Park, OH: ASM International (in Inglés), 2000.

[14] A. J. Wilkinson and T. B. Britton, "Strains, planes, and EBSD in materials science," *Materials Today*, vol. 15, no. 9, pp. 366-376, 2012/09/01/ 2012, doi: https://doi.org/10.1016/S1369-7021(12)70163-3.

[15] M. Trempa, G. Müller, J. Friedrich, and C. Reimann, "Grain Boundaries in Multicrystalline Silicon," in *Handbook of Photovoltaic Silicon*, D. Yang Ed. Berlin, Heidelberg: Springer Berlin Heidelberg, 2018, pp. 1-48.

[16] A. S. Wilson, K. A. Christofidou, A. Evans, M. C. Hardy, and H. J. Stone, "Comparison of Methods for Quantification of Topologically Close-Packed Phases in Ni-Based Superalloys," *Metallurgical and Materials Transactions A*, vol. 50, no. 12, pp. 5925-5934, 2019/12/01 2019, doi: 10.1007/s11661-019-05442-3.

[17] J. C. Zhao, M. Larsen, and V. Ravikumar, "Phase precipitation and time–temperature-transformation diagram of Hastelloy X," *Materials Science and Engineering: A*, vol. 293, no. 1, pp. 112-119, 2000/11/30/ 2000, doi: https://doi.org/10.1016/S0921-5093(00)01049-2.

[18] W. E. King *et al.*, "Laser powder bed fusion additive manufacturing of metals; physics, computational, and materials challenges," *Applied Physics Reviews*, vol. 2, no. 4, p. 041304, 2015, doi: 10.1063/1.4937809.

[19] S. Kou, *Welding metallurgy*, 2nd ed. Hoboken, N.J.: Wiley-Interscience (in Inglés), 2003.

[20] S. Zaefferer and N.-N. Elhami, "Theory and application of electron channelling contrast imaging under controlled diffraction conditions," *Acta Materialia*, vol. 75, pp. 20-50, 2014/08/15/ 2014, doi: https://doi.org/10.1016/j.actamat.2014.04.018.

[21] X. Dong, X. Zhang, K. Du, Y. Zhou, T. Jin, and H. Ye, "Microstructure of Carbides at Grain Boundaries in Nickel Based Superalloys," *Journal of Materials Science & Technology*, vol. 28, no. 11, pp. 1031-1038, 2012/11/01/ 2012, doi: https://doi.org/10.1016/S1005-0302(12)60169-8.

[22] M. Laleh, A. E. Hughes, M. Y. Tan, G. S. Rohrer, S. Primig, and N. Haghdadi, "Grain boundary character distribution in an additively manufactured austenitic stainless steel," *Scripta Materialia*, vol. 192, pp. 115-119, 2021/02/01/ 2021, doi: https://doi.org/10.1016/j.scriptamat.2020.10.018.

[23] M. Gintalas and P. E. J. Rivera-Diaz-del-Castillo, "Advanced Electron Microscopy: Progress and Application of Electron Backscatter Diffraction," in *Encyclopedia of Materials: Metals and Alloys*, F. G. Caballero Ed. Oxford: Elsevier, 2022, pp. 648-661.

[24] A. Shaji Karapuzha *et al.*, "Microstructure, mechanical behaviour and strengthening mechanisms in Hastelloy X manufactured by electron beam and laser beam powder bed fusion," *Journal of Alloys and Compounds*, vol. 862, p. 158034, 2021/05/05/ 2021, doi: https://doi.org/10.1016/j.jallcom.2020.158034.
[25] S. I. Wright, M. M. Nowell, R. de Kloe, and L. Chan, "Orientation precision of electron backscatter diffraction measurements near grain boundaries," (in eng), *Microsc Microanal*, vol. 20, no. 3, pp. 852-63, Jun 2014, doi: 10.1017/s143192761400035x.
[26] B. Blakey-Milner *et al.*, "Metal additive manufacturing in aerospace: A review," *Materials & Design*, vol. 209, p. 110008, 2021/11/01/ 2021, doi: https://doi.org/10.1016/j.matdes.2021.110008.
[27] M. Froend, V. Ventzke, F. Dorn, N. Kashaev, B. Klusemann, and J. Enz, "Microstructure by design: An approach of grain refinement and isotropy improvement in multi-layer wire-based laser metal deposition," *Materials Science and Engineering: A*, vol. 772, p. 138635, 2020/01/20/ 2020, doi: https://doi.org/10.1016/j.msea.2019.138635.
[28] S. Kaboli, H. Demers, N. Brodusch, and R. Gauvin, "Rotation contour contrast reconstruction using electron backscatter diffraction in a scanning electron microscope," *Journal of Applied Crystallography*, vol. 48, no. 3, pp. 776-785, 2015, doi: doi:10.1107/S1600576715005658.
[29] Q. Han *et al.*, "Laser powder bed fusion of Hastelloy X: Effects of hot isostatic pressing and the hot cracking mechanism," *Materials Science and Engineering: A*, vol. 732, pp. 228-239, 2018/08/08/ 2018, doi: https://doi.org/10.1016/j.msea.2018.07.008.
[30] K. Karayagiz *et al.*, "Finite interface dissipation phase field modeling of Ni–Nb under additive manufacturing conditions," *Acta Materialia*, vol. 185, pp. 320-339, 2020/02/15/ 2020, doi: https://doi.org/10.1016/j.actamat.2019.11.057.
[31] D. J. Dingley, G. Meaden, D. J. Dingley, and A. P. Day, "A review of EBSD: from rudimentary on line orientation measurements to high resolution elastic strain measurements over the past 30 years," *IOP Conference Series: Materials Science and Engineering*, vol. 375, p. 012003, 2018/06 2018, doi: 10.1088/1757-899x/375/1/012003.
[32] L. GmbH. "TUBE BUNDLE HEAT EXCHANGERS." https://lob-gmbh.de/en/produkt/heat-exchangers/ (accessed.
[33] S. Sanchez *et al.*, "Powder Bed Fusion of nickel-based superalloys: A review," *International Journal of Machine Tools and Manufacture*, vol. 165, p. 103729, 2021/06/01/ 2021, doi: https://doi.org/10.1016/j.ijmachtools.2021.103729.
[34] H. INTERNATIONAL. "HASTELLOY® X alloy." https://haynesintl.com/alloys/alloy-portfolio_/High-temperature-Alloys/HASTELLOY-X-alloy (accessed.
[35] M. P. Haines, V. V. Rielli, S. Primig, and N. Haghdadi, "Powder bed fusion additive manufacturing of Ni-based superalloys: a review of the main microstructural constituents and characterization techniques," *Journal of Materials Science*, 2022/07/27 2022, doi: 10.1007/s10853-022-07501-4.
[36] Y. Matsukawa, "Crystallography of Precipitates in Metals and Alloys: (1) Analysis of Crystallography," *IntechOpen*, 2019, doi: 10.5772/intechopen.82693.
[37] E. N. Borodin and A. E. Mayer, "Influence of structure of grain boundaries and size distribution of grains on the yield strength at quasistatic and dynamical loading," *Materials Research Express*, vol. 4, no. 8, p. 085040, 2017/08/29 2017, doi: 10.1088/2053-1591/aa8514.
[38] Y. X. Xu, J. T. Lu, W. Y. Li, and X. W. Yang, "Oxidation behaviour of Nb-rich Ni-Cr-Fe alloys: Role and effect of carbides precipitates," *Corrosion Science*, vol. 140, pp. 252-259, 2018, doi: 10.1016/j.corsci.2018.05.040.
[39] S. Waqar, K. Guo, and J. Sun, "Evolution of residual stress behavior in selective laser melting (SLM) of 316L stainless steel through preheating and in-situ re-scanning techniques," *Optics & Laser Technology*, vol. 149, p. 107806, 2022/05/01/ 2022, doi: https://doi.org/10.1016/j.optlastec.2021.107806.
[40] M. S. Wang, E. W. Liu, Y. L. Du, T. T. Liu, and W. H. Liao, "Cracking mechanism and a novel strategy to eliminate cracks in TiAl alloy additively manufactured by selective laser melting," *Scripta Materialia*, vol. 204, p. 114151, 2021/11/01/ 2021, doi: https://doi.org/10.1016/j.scriptamat.2021.114151.
[41] A. Jena, S. E. Atabay, and M. Brochu, "Microstructure and mechanical properties of crack-free Inconel 738 fabricated by laser powder bed fusion," *Materials Science and Engineering: A*, vol. 850, p. 143524, 2022/08/11/ 2022, doi: https://doi.org/10.1016/j.msea.2022.143524.
[42] O. Sanchez-Mata, X. Wang, J. A. Muñiz-Lerma, M. Attarian Shandiz, R. Gauvin, and M. Brochu, "Fabrication of Crack-Free Nickel-Based Superalloy Considered Non-Weldable during Laser Powder Bed Fusion," *Materials*, vol. 11, no. 8, 2018, doi: 10.3390/ma11081288.
[43] S. E. Atabay, O. Sanchez-Mata, J. A. Muñiz-Lerma, and M. Brochu, "Microstructure and mechanical properties of difficult to weld Rene 77 superalloy produced by laser powder bed fusion," *Materials Science and Engineering: A*, vol. 827, p. 142053, 2021/10/19/ 2021, doi: https://doi.org/10.1016/j.msea.2021.142053.

[44] D. Tomus, P. A. Rometsch, M. Heilmaier, and X. Wu, "Effect of minor alloying elements on crack-formation characteristics of Hastelloy-X manufactured by selective laser melting," *Additive Manufacturing*, vol. 16, pp. 65-72, 2017/08/01/ 2017, doi: https://doi.org/10.1016/j.addma.2017.05.006.

[45] K. Kempen, B. Vrancken, S. Buls, L. Thijs, J. Humbeeck, and J.-P. Kruth, "Selective Laser Melting of Crack-Free High Density M2 High Speed Steel Parts by Baseplate Preheating," *Journal of Manufacturing Science and Engineering*, vol. 136, 12/01 2014, doi: 10.1115/1.4028513.

[46] G. Marchese *et al.*, "Microstructural Evolution of Post-Processed Hastelloy X Alloy Fabricated by Laser Powder Bed Fusion," *Materials*, vol. 12, no. 3, p. 486, 2019. [Online]. Available: https://www.mdpi.com/1996-1944/12/3/486.

[47] S. Pourbabak, M. L. Montero-Sistiaga, D. Schryvers, J. Van Humbeeck, and K. Vanmeensel, "Microscopic investigation of as built and hot isostatic pressed Hastelloy X processed by Selective Laser Melting," *Materials Characterization*, vol. 153, pp. 366-371, 2019/07/01/ 2019, doi: https://doi.org/10.1016/j.matchar.2019.05.024.

[48] J. Wang *et al.*, "Improvement of densification and microstructure of ASTM A131 EH36 steel samples additively manufactured via selective laser melting with varying laser scanning speed and hatch spacing," *Materials Science and Engineering: A*, vol. 746, pp. 300-313, 2019/02/11/ 2019, doi: https://doi.org/10.1016/j.msea.2019.01.019.

[49] J. Liu, G. Li, Q. Sun, H. Li, J. Sun, and X. Wang, "Understanding the effect of scanning strategies on the microstructure and crystallographic texture of Ti-6Al-4V alloy manufactured by laser powder bed fusion," *Journal of Materials Processing Technology*, vol. 299, p. 117366, 2022/01/01/ 2022, doi: https://doi.org/10.1016/j.jmatprotec.2021.117366.

[50] M. S. Moyle, N. Haghdadi, X. Z. Liao, S. P. Ringer, and S. Primig, "On the microstructure and texture evolution in 17-4 PH stainless steel during laser powder bed fusion: Towards textural design," *Journal of Materials Science & Technology*, vol. 117, pp. 183-195, 2022/08/01/ 2022, doi: https://doi.org/10.1016/j.jmst.2021.12.015.

[51] J. Robinson, I. Ashton, P. Fox, E. Jones, and C. Sutcliffe, "Determination of the effect of scan strategy on residual stress in laser powder bed fusion additive manufacturing," *Additive Manufacturing*, vol. 23, pp. 13-24, 2018/10/01/ 2018, doi: https://doi.org/10.1016/j.addma.2018.07.001.

[52] W. Zhang, M. Tong, and N. M. Harrison, "Scanning strategies effect on temperature, residual stress and deformation by multi-laser beam powder bed fusion manufacturing," *Additive Manufacturing*, vol. 36, p. 101507, 2020/12/01/ 2020, doi: https://doi.org/10.1016/j.addma.2020.101507.

[53] X. Zhang *et al.*, "Effect of the scanning strategy on microstructure and mechanical anisotropy of Hastelloy X superalloy produced by Laser Powder Bed Fusion," *Materials Characterization*, vol. 173, p. 110951, 2021/03/01/ 2021, doi: https://doi.org/10.1016/j.matchar.2021.110951.

[54] O. Sanchez-Mata, J. A. Muñiz-Lerma, X. Wang, S. E. Atabay, M. Attarian Shandiz, and M. Brochu, "Microstructure and mechanical properties at room and elevated temperature of crack-free Hastelloy X fabricated by laser powder bed fusion," *Materials Science and Engineering: A*, vol. 780, p. 139177, 2020/04/07/ 2020, doi: https://doi.org/10.1016/j.msea.2020.139177.

[55] F. Haguenau, P. W. Hawkes, J. L. Hutchison, B. Satiat–Jeunemaître, G. T. Simon, and D. B. Williams, "Key Events in the History of Electron Microscopy," *Microscopy and Microanalysis*, vol. 9, no. 2, pp. 96-138, 2003, doi: 10.1017/S1431927603030113.

[56] D. Dingley, "Progressive steps in the development of electron backscatter diffraction and orientation imaging microscopy," *Journal of Microscopy*, vol. 213, no. 3, pp. 214-224, 2004, doi: https://doi.org/10.1111/j.0022-2720.2004.01321.x.

[57] N. C. Krieger Lassen, "Automatic localisation of electron backscattering pattern bands from Hough transform," *Materials Science and Technology*, vol. 12, no. 10, pp. 837-843, 1996/10/01 1996, doi: 10.1179/mst.1996.12.10.837.

[58] X. Wang *et al.*, "Control of precipitation behaviour of Hastelloy-X through grain boundary engineering," *Materials Science and Technology*, vol. 33, no. 17, pp. 2078-2085, 2017/11/22 2017, doi: 10.1080/02670836.2017.1345823.

[59] F. Wang, "Mechanical property study on rapid additive layer manufacture Hastelloy® X alloy by selective laser melting technology," *The International Journal of Advanced Manufacturing Technology*, vol. 58, no. 5, pp. 545-551, 2012/01/01 2012, doi: 10.1007/s00170-011-3423-2.

[60] S. I. Wright, M. M. Nowell, and D. P. Field, "A Review of Strain Analysis Using Electron Backscatter Diffraction," *Microscopy and Microanalysis*, vol. 17, no. 3, pp. 316-329, 2011, doi: 10.1017/S1431927611000055.

[61] S. Gorsse, C. Hutchinson, M. Goune, and R. Banerjee, "Additive manufacturing of metals: a brief review of the characteristic microstructures and properties of steels, Ti-6Al-4V and high-entropy alloys," (in English), *Sci Technol Adv Mat*, vol. 18, no. 1, pp. 584-610, Aug 25 2017, doi: 10.1080/14686996.2017.1361305.

[62] *ASTM 5900:2021 Additive manufacturing — General principles — Fundamentals and vocabulary*, I. O. f. S. A. S. f. T. a. Materials, 2021.
[63] M. Li, W. Du, A. Elwany, Z. Pei, and C. Ma, "Metal Binder Jetting Additive Manufacturing: A Literature Review," *Journal of Manufacturing Science and Engineering*, vol. 142, no. 9, 2020, doi: 10.1115/1.4047430.
[64] T. DebRoy *et al.*, "Additive manufacturing of metallic components – Process, structure and properties," *Progress in Materials Science*, vol. 92, pp. 112-224, 2018/03/01/ 2018, doi: https://doi.org/10.1016/j.pmatsci.2017.10.001.
[65] J. A. Gonzalez, J. Mireles, S. W. Stafford, M. A. Perez, C. A. Terrazas, and R. B. Wicker, "Characterization of Inconel 625 fabricated using powder-bed-based additive manufacturing technologies," *Journal of Materials Processing Technology*, vol. 264, pp. 200-210, 2019/02/01/ 2019, doi: https://doi.org/10.1016/j.jmatprotec.2018.08.031.
[66] K. Moeinfar, F. Khodabakhshi, S. F. Kashani-bozorg, M. Mohammadi, and A. P. Gerlich, "A review on metallurgical aspects of laser additive manufacturing (LAM): Stainless steels, nickel superalloys, and titanium alloys," *Journal of Materials Research and Technology*, vol. 16, pp. 1029-1068, 2022/01/01/ 2022, doi: https://doi.org/10.1016/j.jmrt.2021.12.039.
[67] Y. Zhang, S. Yang, and Y. F. Zhao, "Manufacturability analysis of metal laser-based powder bed fusion additive manufacturing—a survey," *The International Journal of Advanced Manufacturing Technology*, vol. 110, no. 1, pp. 57-78, 2020/09/01 2020, doi: 10.1007/s00170-020-05825-6.
[68] W. C. Winegard, "FUNDAMENTALS OF THE SOLIDIFICATION OF METALS," *Metallurgical Reviews*, vol. 6, no. 1, pp. 57-100, 1961/01/01 1961, doi: 10.1179/mtlr.1961.6.1.57.
[69] W. Kurz and D. J. Fisher, *Fundamentals of solidification*, 3rd [rev.] ed. Aedermannsdorf, Switzerland ;: Trans Tech Publications (in Inglés), 1992.
[70] T. Pinomaa, A. Laukkanen, and N. Provatas, "Solute trapping in rapid solidification," *MRS Bulletin*, vol. 45, no. 11, pp. 910-915, 2020, doi: 10.1557/mrs.2020.274.
[71] L. Nastac and D. M. Stefanescu, "An Analytical Model for Solute Redistribution during Solidification of Planar, Columnar, or Equiaxed Morphology," *Metallurgical and Materials Transactions A*, vol. 24, no. 9, pp. 2107-2118, 1993/09/01 1993, doi: 10.1007/BF02666344.
[72] D. H. Kirkwood, "Microsegregation," *Materials Science and Engineering*, vol. 65, no. 1, pp. 101-109, 1984/07/01/ 1984, doi: https://doi.org/10.1016/0025-5416(84)90204-0.
[73] S. Dépinoy, M. Sennour, L. Ferhat, and C. Colin, "Experimental determination of solute redistribution behavior during solidification of additively manufactured 316L," *Scripta Materialia*, vol. 194, p. 113663, 2021/03/15/ 2021, doi: https://doi.org/10.1016/j.scriptamat.2020.113663.
[74] W. Jie, "Solute redistribution and segregation in solidification processes," *Sci Technol Adv Mat*, vol. 2, no. 1, pp. 29-35, 2001/01/01 2001, doi: 10.1016/S1468-6996(01)00022-5.
[75] A. Kreitcberg and V. Brailovski, "Effect of Fe and C Contents on the Microstructure and High-Temperature Mechanical Properties of IN625 Alloy Processed by Laser Powder Bed Fusion," *Materials*, vol. 15, no. 19, p. 6606, 2022. [Online]. Available: https://www.mdpi.com/1996-1944/15/19/6606.
[76] Z. R. Khayat and T. A. Palmer, "Impact of iron composition on the properties of an additively manufactured solid solution strengthened nickel base alloy," *Materials Science and Engineering: A*, vol. 718, pp. 123-134, 2018/03/07/ 2018, doi: https://doi.org/10.1016/j.msea.2018.01.112.
[77] F. Wang, D. Ma, and A. Bührig-Polaczek, "Microsegregation behavior of alloying elements in single-crystal nickel-based superalloys with emphasis on dendritic structure," *Materials Characterization*, vol. 127, pp. 311-316, 2017/05/01/ 2017, doi: https://doi.org/10.1016/j.matchar.2017.02.030.
[78] "Solidification Structures of Pure Metals," in *Metallography and Microstructures*, vol. 9, G. F. Vander Voort Ed.: ASM International, 2004, p. 0.
[79] P. K. Sung and D. R. Poirier, "Liquid-solid partition ratios in nickel-base alloys," *Metallurgical and Materials Transactions A*, vol. 30, no. 8, pp. 2173-2181, 1999/08/01 1999, doi: 10.1007/s11661-999-0029-5.
[80] N. Kwabena Adomako, N. Haghdadi, and S. Primig, "Electron and laser-based additive manufacturing of Ni-based superalloys: A review of heterogeneities in microstructure and mechanical properties," *Materials & Design*, vol. 223, p. 111245, 2022/11/01/ 2022, doi: https://doi.org/10.1016/j.matdes.2022.111245.
[81] L. N. Carter *et al.*, "Process optimisation of selective laser melting using energy density model for nickel based superalloys," *Materials Science and Technology*, vol. 32, no. 7, pp. 657-661, 2016/05/02 2016, doi: 10.1179/1743284715Y.0000000108.
[82] H. L. Wei, J. Mazumder, and T. DebRoy, "Evolution of solidification texture during additive manufacturing," *Sci Rep-Uk*, vol. 5, no. 1, p. 16446, 2015/11/10 2015, doi: 10.1038/srep16446.

[83] M. He, H. Cao, Q. Liu, J. Yi, Y. Ni, and S. Wang, "Evolution of dislocation cellular pattern in Inconel 718 alloy fabricated by laser powder-bed fusion," *Additive Manufacturing*, vol. 55, p. 102839, 2022/07/01/ 2022, doi: https://doi.org/10.1016/j.addma.2022.102839.

[84] H. Fredriksson and U. Akerlind, *Solidification and Crystallization Processing in Metals and Alloys*, Hoboken: Wiley, 2012. [Online]. Available: http://www.books24x7.com/marc.asp?bookid=49739.

[85] D. Deng, R. L. Peng, H. Brodin, and J. Moverare, "Microstructure and mechanical properties of Inconel 718 produced by selective laser melting: Sample orientation dependence and effects of post heat treatments," *Materials Science and Engineering: A*, vol. 713, pp. 294-306, 2018/01/24/ 2018, doi: https://doi.org/10.1016/j.msea.2017.12.043.

[86] Z. Liu *et al.*, "Additive manufacturing of metals: Microstructure evolution and multistage control," *Journal of Materials Science & Technology*, vol. 100, pp. 224-236, 2022/02/20/ 2022, doi: https://doi.org/10.1016/j.jmst.2021.06.011.

[87] M. Strantza *et al.*, "Effect of the scanning strategy on the formation of residual stresses in additively manufactured Ti-6Al-4V," *Additive Manufacturing*, vol. 45, p. 102003, 2021/09/01/ 2021, doi: https://doi.org/10.1016/j.addma.2021.102003.

[88] "1 - Introduction to aerospace materials," in *Introduction to Aerospace Materials*, A. P. Mouritz Ed.: Woodhead Publishing, 2012, pp. 1-14.

[89] H. Long, S. Mao, Y. Liu, Z. Zhang, and X. Han, "Microstructural and compositional design of Ni-based single crystalline superalloys — A review," *Journal of Alloys and Compounds*, vol. 743, pp. 203-220, 2018/04/30/ 2018, doi: https://doi.org/10.1016/j.jallcom.2018.01.224.

[90] "Introduction," in *The Superalloys: Fundamentals and Applications*, R. C. Reed Ed. Cambridge: Cambridge University Press, 2006, pp. 1-32.

[91] J. C. L. John N. DuPont, Samuel D. Kiser, "Introduction," in *Welding Metallurgy and Weldability of Nickel-Base Alloys*, 2009, pp. 1-14.

[92] "The physical metallurgy of nickel and its alloys," in *The Superalloys: Fundamentals and Applications*, R. C. Reed Ed. Cambridge: Cambridge University Press, 2006, pp. 33-120.

[93] B. Graybill, M. Li, D. Malawey, C. Ma, J.-M. Alvarado-Orozco, and E. Martinez-Franco, "Additive Manufacturing of Nickel-Based Superalloys," in *ASME 2018 13th International Manufacturing Science and Engineering Conference*, 2018, vol. Volume 1: Additive Manufacturing; Bio and Sustainable Manufacturing, V001T01A015, doi: 10.1115/msec2018-6666. [Online]. Available: https://doi.org/10.1115/MSEC2018-6666

[94] J. C. L. John N. DuPont, Samuel D. Kiser, "Alloying Additions, Phase Diagrams, and Phase Stability," in *Welding Metallurgy and Weldability of Nickel-Base Alloys*, 2009, pp. 15-45.

[95] B. Lezzar, O. Khalfallah, A. Larere, V. Paidar, and O. Hardouin Duparc, "Detailed analysis of the segregation driving forces for Ni(Ag) and Ag(Ni) in the Σ=11 {113} and Σ=11 {332} grain boundaries," *Acta Materialia*, vol. 52, no. 9, pp. 2809-2818, 2004/05/17/ 2004, doi: https://doi.org/10.1016/j.actamat.2004.02.027.

[96] L. Yuan, R. Hu, T. Zhang, Y. Han, X. Xue, and J. Li, "Precipitation Behavior of Pt2Mo-Type Superlattices in Hastelloy C-2000 Superalloy with Low Mo/Cr Ratio," *Journal of Materials Engineering and Performance*, vol. 23, no. 9, pp. 3314-3320, 2014/09/01 2014, doi: 10.1007/s11665-014-1126-1.

[97] R. Kirchheim, "Reducing grain boundary, dislocation line and vacancy formation energies by solute segregationII. Experimental evidence and consequences," *Acta Materialia*, vol. 55, no. 15, pp. 5139-5148, 2007, doi: 10.1016/j.actamat.2007.05.033.

[98] P. Lejček, "Grain Boundary Segregation and Related Phenomena," in *Grain Boundary Segregation in Metals*, P. Lejcek Ed. Berlin, Heidelberg: Springer Berlin Heidelberg, 2010, pp. 173-201.

[99] P. Lejček, "Approaches to Study Grain Boundary Segregation," in *Grain Boundary Segregation in Metals*, P. Lejcek Ed. Berlin, Heidelberg: Springer Berlin Heidelberg, 2010, pp. 25-49.

[100] M. M. Tavakkoli and S. M. Abbasi, "Effect of molybdenum on grain boundary segregation in Incoloy 901 superalloy," *Materials & Design*, vol. 46, pp. 573-578, 2013/04/01/ 2013, doi: https://doi.org/10.1016/j.matdes.2012.11.002.

[101] M. Nastar, L. T. Belkacemi, E. Meslin, and M. Loyer-Prost, "Thermodynamic model for lattice point defect-mediated semi-coherent precipitation in alloys," *Communications Materials*, vol. 2, no. 1, p. 32, 2021/03/23 2021, doi: 10.1038/s43246-021-00136-z.

[102] R. Kirchheim, "Grain coarsening inhibited by solute segregation," *Acta Materialia*, vol. 50, no. 2, pp. 413-419, 2002/01/22/ 2002, doi: https://doi.org/10.1016/S1359-6454(01)00338-X.

[103] T. J. Garosshen and G. P. McCarthy, "Low temperature carbide precipitation in a nickel base superalloy," *Metallurgical Transactions A*, vol. 16, no. 7, pp. 1213-1223, 1985/07/01 1985, doi: 10.1007/BF02670326.

[104] A. K. Jena and M. C. Chaturvedi, "The role of alloying elements in the design of nickel-base superalloys," *Journal of Materials Science*, vol. 19, no. 10, pp. 3121-3139, 1984/10/01 1984, doi: 10.1007/BF00549796.
[105] G. Bai, J. Li, R. Hu, T. Zhang, H. Kou, and H. Fu, "Effect of thermal exposure on the stability of carbides in Ni–Cr–W based superalloy," *Materials Science and Engineering: A*, vol. 528, no. 6, pp. 2339-2344, 2011/03/15/ 2011, doi: https://doi.org/10.1016/j.msea.2010.11.088.
[106] H. M. Tawancy, "Long-term ageing characteristics of Hastelloy alloy X," *Journal of Materials Science*, vol. 18, no. 10, pp. 2976-2986, 1983/10/01 1983, doi: 10.1007/BF00700780.
[107] G. Marchese *et al.*, "Study of the Microstructure and Cracking Mechanisms of Hastelloy X Produced by Laser Powder Bed Fusion," *Materials*, vol. 11, no. 1, p. 106, 2018. [Online]. Available: https://www.mdpi.com/1996-1944/11/1/106.
[108] A. Verma, J. B. Singh, S. D. Kaushik, and V. Siruguri, "Lattice parameter variation and its effect on precipitation behaviour of ordered Ni2(Cr,Mo) phase in Ni-Cr-Mo alloys," *Journal of Alloys and Compounds*, vol. 813, p. 152195, 2020/01/15/ 2020, doi: https://doi.org/10.1016/j.jallcom.2019.152195.
[109] R. V. Miner and M. G. Castelli, "Hardening mechanisms in a dynamic strain aging alloy, HASTELLOY X, during isothermal and thermomechanical cyclic deformation," *Metallurgical Transactions A*, vol. 23, no. 2, pp. 551-561, 1992/02/01 1992, doi: 10.1007/BF02801173.
[110] Y. Han, X. Xue, T. Zhang, R. Hu, and J. Li, "Grain boundary character correlated carbide precipitation and mechanical properties of Ni-20Cr-18W-1Mo superalloy," *Materials Science and Engineering: A*, vol. 667, pp. 391-401, 2016/06/14/ 2016, doi: https://doi.org/10.1016/j.msea.2016.05.028.
[111] H. International, "HASTELLOY® X alloy," ed, 2019.
[112] A. International, "ASM B 572 06, Standard Specification for UNS N06002, UNS N06230, UNS N12160, and UNS R30556 Rod," ed, 2016.
[113] P. Bajaj, A. Hariharan, A. Kini, P. Kürnsteiner, D. Raabe, and E. A. Jägle, "Steels in additive manufacturing: A review of their microstructure and properties," *Materials Science and Engineering: A*, vol. 772, p. 138633, 2020/01/20/ 2020, doi: https://doi.org/10.1016/j.msea.2019.138633.
[114] N. J. Harrison, I. Todd, and K. Mumtaz, "Reduction of micro-cracking in nickel superalloys processed by Selective Laser Melting: A fundamental alloy design approach," *Acta Materialia*, vol. 94, pp. 59-68, 2015/08/01/ 2015, doi: https://doi.org/10.1016/j.actamat.2015.04.035.
[115] Q. Han, Y. Gu, S. Soe, F. Lacan, and R. Setchi, "Effect of hot cracking on the mechanical properties of Hastelloy X superalloy fabricated by laser powder bed fusion additive manufacturing," *Optics & Laser Technology*, vol. 124, p. 105984, 2020/04/01/ 2020, doi: https://doi.org/10.1016/j.optlastec.2019.105984.
[116] D. A. Porter, K. E. Easterling, and M. Y. Sherif, *Phase transformations in metals and alloys*, Third edition / ed. Boca Raton, FL: CRC Press (in Inglés), 2009.
[117] Z. Sun, X. P. Tan, M. Descoins, D. Mangelinck, S. B. Tor, and C. S. Lim, "Revealing hot tearing mechanism for an additively manufactured high-entropy alloy via selective laser melting," *Scripta Materialia*, vol. 168, pp. 129-133, 2019/07/15/ 2019, doi: https://doi.org/10.1016/j.scriptamat.2019.04.036.
[118] T. A. Book and M. D. Sangid, "Strain localization in Ti-6Al-4V Widmanstätten microstructures produced by additive manufacturing," *Materials Characterization*, vol. 122, pp. 104-112, 2016/12/01/ 2016, doi: https://doi.org/10.1016/j.matchar.2016.10.018.
[119] Z. Sun *et al.*, "Reducing hot tearing by grain boundary segregation engineering in additive manufacturing: example of an AlxCoCrFeNi high-entropy alloy," *Acta Materialia*, vol. 204, p. 116505, 2021/02/01/ 2021, doi: https://doi.org/10.1016/j.actamat.2020.116505.
[120] F. Abdi *et al.*, "Grain boundary engineering of new additive manufactured polycrystalline alloys," *Forces in Mechanics*, vol. 4, p. 100033, 2021/10/01/ 2021, doi: https://doi.org/10.1016/j.finmec.2021.100033.
[121] M. Muhammad *et al.*, "Additively Manufactured Hastelloy-X: Effect of Post-Process Heat Treatment on Microstructure and Mechanical Properties," in *2021 International Solid Freeform Fabrication Symposium*, 2021: University of Texas at Austin.
[122] D. Tomus, Y. Tian, P. A. Rometsch, M. Heilmaier, and X. Wu, "Influence of post heat treatments on anisotropy of mechanical behaviour and microstructure of Hastelloy-X parts produced by selective laser melting," *Materials Science and Engineering: A*, vol. 667, pp. 42-53, 2016/06/14/ 2016, doi: https://doi.org/10.1016/j.msea.2016.04.086.
[123] H. Wang *et al.*, "Micro-cracking, microstructure and mechanical properties of Hastelloy-X alloy printed by laser powder bed fusion: As-built, annealed and hot-isostatic pressed," *Additive Manufacturing*, vol. 39, p. 101853, 2021/03/01/ 2021, doi: https://doi.org/10.1016/j.addma.2021.101853.
[124] X. Ni, D. Kong, L. Zhang, C. Dong, J. Song, and W. Wu, "Effect of Process Parameters on the Mechanical Properties of Hastelloy X Alloy Fabricated by Selective Laser Melting," *Journal of Materials*

Engineering and Performance, vol. 28, no. 9, pp. 5533-5540, 2019/09/01 2019, doi: 10.1007/s11665-019-04275-w.

[125] J. Pistor and C. Korner, "A novel mechanism to generate metallic single crystals," (in English), *Sci Rep-Uk*, vol. 11, no. 1, Dec 29 2021, doi: ARTN 24482

10.1038/s41598-021-04235-2.

[126] V. Randle and O. Engler, *Introduction to texture analysis : macrotexture, microtexture and orientation mapping*. Amsterdam, The Netherlands: Gordon & Breach (in Inglés), 2000.

[127] J. I. Goldstein, D. E. Newbury, A. D. Romig, C. Fiori, and E. Lifshin, *Scanning Electron Microscopy and X-Ray Microanalysis : a Text for Biologists, Materials Scientists, and Geologists*, N. ed. Boston: Springer US, 1992. [Online]. Available: http://public.ebookcentral.proquest.com/choice/publicfullrecord.aspx?p=3077317.

[128] T. J. Ruggles, J. I. Deitz, A. A. Allerman, C. B. Carter, and J. R. Michael, "Identification of Star Defects in Gallium Nitride with HREBSD and ECCI," *Microscopy and Microanalysis*, vol. 27, no. 2, pp. 257-265, 2021, doi: 10.1017/S143192762100009X.

[129] A. J. Schwartz, M. Kumar, B. L. Adams, and D. P. Field, *Electron backscatter diffraction in materials science*, Second edition ed. New York, NY: Springer, 2009. [Online]. Available: https://link.springer.com/book/10.1007/978-0-387-88136-2.

[130] A. J. Garratt-Reed and D. C. Bell, *Energy-dispersive X-ray analysis in the electron microscope*, Oxford: BIOS, 2003. [Online]. Available: http://public.ebookcentral.proquest.com/choice/publicfullrecord.aspx?p=4634368.

[131] R. Kamaladasa and Y. Picard, "Basic Principles and Application of Electron Channeling in a Scanning Electron Microscope for Dislocation Analysis," *Microscopy: Science, Technology, Applications and Education*, vol. 3, 01/01 2010.

[132] I. Gutierrez-Urrutia, S. Zaefferer, and D. Raabe, "Coupling of Electron Channeling with EBSD: Toward the Quantitative Characterization of Deformation Structures in the SEM," *JOM*, vol. 65, no. 9, pp. 1229-1236, 2013/09/01 2013, doi: 10.1007/s11837-013-0678-0.

[133] O. Instruments. "Electron Channelling Contrast Imaging." https://www.ebsd.com/ebsd-techniques/channeling-contrast-imaging (accessed 29/04, 2022).

[134] M. Koyama, H. Springer, S. V. Merzlikin, K. Tsuzaki, E. Akiyama, and D. Raabe, "Hydrogen embrittlement associated with strain localization in a precipitation-hardened Fe–Mn–Al–C light weight austenitic steel," *International Journal of Hydrogen Energy*, vol. 39, no. 9, pp. 4634-4646, 2014/03/18/ 2014, doi: https://doi.org/10.1016/j.ijhydene.2013.12.171.

[135] Y.-K. Kim, J.-H. Yu, H. S. Kim, and K.-A. Lee, "In-situ carbide-reinforced CoCrFeMnNi high-entropy alloy matrix nanocomposites manufactured by selective laser melting: Carbon content effects on microstructure, mechanical properties, and deformation mechanism," *Composites Part B: Engineering*, vol. 210, p. 108638, 2021/04/01/ 2021, doi: https://doi.org/10.1016/j.compositesb.2021.108638.

[136] Z. Hou, R. P. Babu, P. Hedström, and J. Odqvist, "Microstructure evolution during tempering of martensitic Fe–C–Cr alloys at 700 °C," *Journal of Materials Science*, vol. 53, no. 9, pp. 6939-6950, 2018/05/01 2018, doi: 10.1007/s10853-018-2036-7.

[137] J. Cocle, "Development of the EBSD intensity response for quantitative strain analyses of materials," 2008. [Online]. Available: http://gateway.proquest.com/openurl?url_ver=Z39.88-2004&rft_val_fmt=info:ofi/fmt:kev:mtx:dissertation&res_dat=xri:pqm&rft_dat=xri:pqdiss:MR66949

[138] V. Randle, "Electron backscatter diffraction: Strategies for reliable data acquisition and processing," *Materials Characterization*, vol. 60, no. 9, pp. 913-922, 2009/09/01/ 2009, doi: https://doi.org/10.1016/j.matchar.2009.05.011.

[139] J.-H. Cho, A. D. Rollett, and K. H. Oh, "Determination of a mean orientation in electron backscatter diffraction measurements," *Metallurgical and Materials Transactions A*, vol. 36, no. 12, pp. 3427-3438, 2005/12/01 2005, doi: 10.1007/s11661-005-0016-4.

[140] S. Suwas and R. K. Ray, *Crystallographic texture of materials*, London: Springer, 2014. [Online]. Available: https://public.ebookcentral.proquest.com/choice/publicfullrecord.aspx?p=1802791.

[141] P. Lejček, "Grain Boundaries: Description, Structure and Thermodynamics," in *Grain Boundary Segregation in Metals*, P. Lejcek Ed. Berlin, Heidelberg: Springer Berlin Heidelberg, 2010, pp. 5-24.

[142] Y. S. Lim, J. H. Han, H. D. Cho, and J. S. Kim, "Precipitation Morphologies of Grain Boundary Chromium Carbides in Alloy 690TT," 2001.

[143] V. Randle, "The coincidence site lattice and the 'sigma enigma'," *Materials Characterization*, vol. 47, no. 5, pp. 411-416, 2001/12/01/ 2001, doi: https://doi.org/10.1016/S1044-5803(02)00193-6.

[144] J. Humphreys, G. S. Rohrer, and A. Rollett, "Chapter 4 - The Structure and Energy of Grain Boundaries," in *Recrystallization and Related Annealing Phenomena (Third Edition)*, J. Humphreys, G. S. Rohrer, and A. Rollett Eds. Oxford: Elsevier, 2017, pp. 109-143.

[145] F. Yazdandoost and R. Mirzaeifar, "Tilt grain boundaries energy and structure in NiTi alloys," *Computational Materials Science*, vol. 131, pp. 108-119, 2017, doi: 10.1016/j.commatsci.2017.01.027.
[146] S. Patala and C. A. Schuh, "A continuous and one-to-one coloring scheme for misorientations," *Acta Materialia*, vol. 59, no. 2, pp. 554-562, 2011/01/01/ 2011, doi: https://doi.org/10.1016/j.actamat.2010.09.058.
[147] S. Patala, J. K. Mason, and C. A. Schuh, "Improved representations of misorientation information for grain boundary science and engineering," *Progress in Materials Science*, vol. 57, no. 8, pp. 1383-1425, 2012/11/01/ 2012, doi: https://doi.org/10.1016/j.pmatsci.2012.04.002.
[148] S.-S. Rui, L.-S. Niu, H.-J. Shi, S. Wei, and C. C. Tasan, "Diffraction-based misorientation mapping: A continuum mechanics description," *Journal of the Mechanics and Physics of Solids*, vol. 133, p. 103709, 2019/12/01/ 2019, doi: https://doi.org/10.1016/j.jmps.2019.103709.
[149] O. Muránsky, L. Balogh, M. Tran, C. J. Hamelin, J. S. Park, and M. R. Daymond, "On the measurement of dislocations and dislocation substructures using EBSD and HRSD techniques," *Acta Materialia*, vol. 175, pp. 297-313, 2019/08/15/ 2019, doi: https://doi.org/10.1016/j.actamat.2019.05.036.
[150] O. Sanchez-Mata, X. Wang, J. A. Muñiz-Lerma, S. E. Atabay, M. Attarian Shandiz, and M. Brochu, "Dependence of mechanical properties on crystallographic orientation in nickel-based superalloy Hastelloy X fabricated by laser powder bed fusion," *Journal of Alloys and Compounds*, vol. 865, p. 158868, 2021/06/05/ 2021, doi: https://doi.org/10.1016/j.jallcom.2021.158868.
[151] *Ultra-high Resolution Scanning Electron Microscope SU8200 series*, 24-14 Nishi-shimbashi 1-chome, Minato-ku Tokyo 105-8717,Japan, HTD-E210 2013.6, 2013. [Online]. Available: https://www.hitachi-hightech.com/file/us/pdf/library/literature/SU8200-CFE-SEM-HTD-E210.pdf. Accessed: 02/11/2022.
[152] A. Tripathi and S. Zaefferer, "On the resolution of EBSD across atomic density and accelerating voltage with a particular focus on the light metal magnesium," *Ultramicroscopy*, vol. 207, p. 112828, 2019/12/01/ 2019, doi: https://doi.org/10.1016/j.ultramic.2019.112828.
[153] A. L. Marshall, J. Holzer, P. Stejskal, C. J. Stephens, T. Vystavěl, and M. J. Whiting, "The EBSD spatial resolution of a Timepix-based detector in a tilt-free geometry," *Ultramicroscopy*, vol. 226, p. 113294, 2021/07/01/ 2021, doi: https://doi.org/10.1016/j.ultramic.2021.113294.
[154] T. J. Ruggles, Y. S. J. Yoo, B. E. Dunlap, M. A. Crimp, and J. Kacher, "Correlating results from high resolution EBSD with TEM- and ECCI-based dislocation microscopy: Approaching single dislocation sensitivity via noise reduction," *Ultramicroscopy*, vol. 210, p. 112927, 2020/03/01/ 2020, doi: https://doi.org/10.1016/j.ultramic.2019.112927.
[155] A. Šakić *et al.*, "Versatile silicon photodiode detector technology for scanning electron microscopy with high-efficiency sub-5 keV electron detection," in *2010 International Electron Devices Meeting*, 6-8 Dec. 2010 2010, pp. 31.4.1-31.4.4, doi: 10.1109/IEDM.2010.5703458.
[156] D. C. Joy, D. E. Newbury, and D. L. Davidson, "Electron channeling patterns in the scanning electron microscope," *Journal of Applied Physics*, vol. 53, no. 8, pp. R81-R122, 1982, doi: 10.1063/1.331668.
[157] A. J. Wilkinson and P. B. Hirsch, "Electron diffraction based techniques in scanning electron microscopy of bulk materials," *Micron*, vol. 28, no. 4, pp. 279-308, 1997/08/01/ 1997, doi: https://doi.org/10.1016/S0968-4328(97)00032-2.
[158] B. N. GmbH. *QUANTAX EBSD*, Germany, DOC-B82-EXS002, Rev. 5, 2017. [Online]. Available: https://www.bruker.com/en/products-and-solutions/elemental-analyzers/eds-wds-ebsd-SEM-Micro-XRF/detectors/eflash-hd.html.
[159] R. G. Byrne, R. J. McGladdery, Z. Zhou, R. C. Thomson, S. S. Doak, and M. A. E. Jepson, "Detection and quantification of precipitates in 11–12 wt% Cr steels using in-column secondary electron detectors," *Materials Characterization*, vol. 165, p. 110356, 2020/07/01/ 2020, doi: https://doi.org/10.1016/j.matchar.2020.110356.
[160] *ImageJ FFT Filter-Plug in*. (2007). [Online]. Available: https://imagej.nih.gov/ij/plugins/fft-filter.html
[161] *ImageJ* (1997-2018). U. S. National Institutes of Health, Bethesda, Maryland, USA. [Online]. Available: https://imagej.nih.gov/ij/docs/guide/146.html
[162] G. Nolze and R. Hielscher, "Orientations - perfectly colored," *Journal of Applied Crystallography*, vol. 49, no. 5, pp. 1786-1802, 2016, doi: 10.1107/S1600576716012942.
[163] R. Hielscher and H. Schaeben, "A novel pole figure inversion method: specification of the MTEX algorithm," *Journal of Applied Crystallography*, vol. 41, no. 6, pp. 1024-1037, 2008, doi: 10.1107/S0021889808030112.
[164] S. Kaboli, "Deformation analysis of hot-compressed magnesium alloys with a field emission scanning electron microscope," McGill University Libraries, [Montreal], 2015. [Online]. Available: https://central.bac-lac.gc.ca/.item?id=TC-QMM-132676&op=pdf&app=Library
[165] P. Tao, H. Li, B. Huang, Q. Hu, S. Gong, and Q. Xu, "The crystal growth, intercellular spacing and microsegregation of selective laser melted Inconel 718 superalloy," *Vacuum*, vol. 159, pp. 382-390, 2019/01/01/ 2019, doi: https://doi.org/10.1016/j.vacuum.2018.10.074.

[166] J. C. L. John N. DuPont, Samuel D. Kiser, "Solid-Solution Strengthened Ni-base Alloys," in *Welding Metallurgy and Weldability of Nickel-Base Alloys*, 2009, pp. 47-156.
[167] R. B. Rebak, and Lou, Xiaoyuan, "Environmental Cracking and Irradiation Resistant Stainless Steels by Additive Manufacturing," GE Global Research Structural Materials Technologies, Schenectady, NY 12309 USA, 2018. [Online]. Available: https://www.osti.gov/servlets/purl/1431212
[168] B. SADEGHI, P. CAVALIERE, M. NOSKO, V. TREMBOŠOVÁ, and Š. NAGY, "Hot deformation behaviour of bimodal sized Al2O3/Al nanocomposites fabricated by spark plasma sintering," *Journal of Microscopy*, vol. 281, no. 1, pp. 28-45, 2021, doi: https://doi.org/10.1111/jmi.12947.
[169] R. E. Smallman and A. H. W. Ngan, "Chapter 2 - Phase equilibria and structure," in *Physical Metallurgy and Advanced Materials Engineering (Seventh Edition)*, R. E. Smallman and A. H. W. Ngan Eds. Oxford: Butterworth-Heinemann, 2007, pp. 37-94.
[170] J.-P. Choi *et al.*, "Densification and microstructural investigation of Inconel 718 parts fabricated by selective laser melting," *Powder Technology*, vol. 310, pp. 60-66, 2017/04/01/ 2017, doi: https://doi.org/10.1016/j.powtec.2017.01.030.
[171] Z. Wang, J. Gu, D. An, Y. Liu, and M. Song, "Characterization of the microstructure and deformation substructure evolution in a hierarchal high-entropy alloy by correlative EBSD and ECCI," *Intermetallics*, vol. 121, p. 106788, 2020/06/01/ 2020, doi: https://doi.org/10.1016/j.intermet.2020.106788.
[172] B. Tang, L. Jiang, R. Hu, and Q. Li, "Correlation between grain boundary misorientation and M23C6 precipitation behaviors in a wrought Ni-based superalloy," *Materials Characterization*, vol. 78, pp. 144-150, 2013/04/01/ 2013, doi: https://doi.org/10.1016/j.matchar.2013.02.006.
[173] A. Du *et al.*, "The dependence of precipitate morphology on the grain boundary types in an aged Al–Cu binary alloy," *Journal of Materials Science*, vol. 56, no. 1, pp. 781-791, 2021/01/01 2021, doi: 10.1007/s10853-020-05239-5.
[174] H. U. Hong, I. S. Kim, B. G. Choi, M. Y. Kim, and C. Y. Jo, "The effect of grain boundary serration on creep resistance in a wrought nickel-based superalloy," *Materials Science and Engineering: A*, vol. 517, no. 1, pp. 125-131, 2009/08/20/ 2009, doi: https://doi.org/10.1016/j.msea.2009.03.071.
[175] C. Joseph, C. Persson, and M. Hörnqvist Colliander, "Precipitation Kinetics and Morphology of Grain Boundary Carbides in Ni-Base Superalloy Haynes 282," *Metallurgical and Materials Transactions A*, vol. 51, no. 12, pp. 6136-6141, 2020/12/01 2020, doi: 10.1007/s11661-020-06019-1.
[176] R. Dong, J. Li, T. Zhang, R. Hu, and H. Kou, "Elements segregation and phase precipitation behavior at grain boundary in a Ni-Cr-W based superalloy," *Materials Characterization*, vol. 122, pp. 189-196, 2016/12/01/ 2016, doi: https://doi.org/10.1016/j.matchar.2016.11.002.
[177] H. Wen, B. Zhao, X. Dong, F. Sun, and L. Zhang, "Preferential growth of coherent precipitates at grain boundary," *Materials Letters*, vol. 261, p. 126984, 2020/02/15/ 2020, doi: https://doi.org/10.1016/j.matlet.2019.126984.
[178] E. C. Caldwell, F. J. Fela, and G. E. Fuchs, "The Segregation of Elements in High-Refractory-Content Single-Crystal Nickel-Based Superalloys," (in English), *JOM*, vol. 56, no. 9, p. 44, Sep 2004 2004. [Online]. Available: https://doi.org/10.1007/s11837-004-0200-9.
[179] J. Sarkar, "Chapter 4 - Sputtering Target Manufacturing," in *Sputtering Materials for VLSI and Thin Film Devices*, J. Sarkar Ed. Boston: William Andrew Publishing, 2014, pp. 197-289.
[180] A. Després *et al.*, "On the variety and formation sequence of second-phase particles in nickel-based superalloys fabricated by laser powder bed fusion," *Materialia*, vol. 15, p. 101037, 2021/03/01/ 2021, doi: https://doi.org/10.1016/j.mtla.2021.101037.
[181] T. Froeliger *et al.*, "Interplay between solidification microsegregation and complex precipitation in a γ/γ' cobalt-based superalloy elaborated by directed energy deposition," *Materials Characterization*, vol. 194, p. 112376, 2022/12/01/ 2022, doi: https://doi.org/10.1016/j.matchar.2022.112376.
[182] D. Kong *et al.*, "Anisotropic response in mechanical and corrosion properties of hastelloy X fabricated by selective laser melting," *Construction and Building Materials*, vol. 221, pp. 720-729, 2019/10/10/ 2019, doi: https://doi.org/10.1016/j.conbuildmat.2019.06.132.
[183] Y. Wang and J. Shi, "Influence of laser scan speed on micro-segregation in selective laser melting of an iron-carbon alloy: A multi-scale simulation study," *Procedia Manufacturing*, vol. 26, pp. 941-951, 2018/01/01/ 2018, doi: https://doi.org/10.1016/j.promfg.2018.07.121.
[184] M. L. Montero-Sistiaga, S. Pourbabak, J. Van Humbeeck, D. Schryvers, and K. Vanmeensel, "Microstructure and mechanical properties of Hastelloy X produced by HP-SLM (high power selective laser melting)," *Materials & Design*, vol. 165, p. 107598, 2019/03/05/ 2019, doi: https://doi.org/10.1016/j.matdes.2019.107598.
[185] B. Guo *et al.*, "Origins of the mechanical property heterogeneity in a hybrid additive manufactured Hastelloy X," *Materials Science and Engineering: A*, vol. 823, p. 141716, 2021/08/17/ 2021, doi: https://doi.org/10.1016/j.msea.2021.141716.

[186] Y. S. Lim, D. J. Kim, S. S. Hwang, H. P. Kim, and S. W. Kim, "M23C6 precipitation behavior and grain boundary serration in Ni-based Alloy 690," *Materials Characterization*, vol. 96, pp. 28-39, 2014, doi: 10.1016/j.matchar.2014.07.008.
[187] Y. T. Tang, P. Karamched, J. Liu, J. C. Haley, R. C. Reed, and A. J. Wilkinson, "Grain boundary serration in nickel alloy inconel 600: Quantification and mechanisms," *Acta Materialia*, vol. 181, pp. 352-366, 2019/12/01/ 2019, doi: https://doi.org/10.1016/j.actamat.2019.09.037.
[188] R. J. Mitchell, H. Y. Li, and Z. W. Huang, "On the formation of serrated grain boundaries and fan type structures in an advanced polycrystalline nickel-base superalloy," *Journal of Materials Processing Technology*, vol. 209, no. 2, pp. 1011-1017, 2009, doi: 10.1016/j.jmatprotec.2008.03.008.
[189] A. Wisniewski and J. Beddoes, "Influence of grain-boundary morphology on creep of a wrought Ni-base superalloy," *Materials Science and Engineering: A*, vol. 510-511, pp. 266-272, 2009/06/15/ 2009, doi: https://doi.org/10.1016/j.msea.2008.04.130.
[190] M. A. Gibson and C. A. Schuh, "Segregation-induced changes in grain boundary cohesion and embrittlement in binary alloys," *Acta Materialia*, vol. 95, pp. 145-155, 2015, doi: 10.1016/j.actamat.2015.05.004.
[191] P. Lejček, "Models of Equilibrium Grain Boundary Segregation," in *Grain Boundary Segregation in Metals*, P. Lejcek Ed. Berlin, Heidelberg: Springer Berlin Heidelberg, 2010, pp. 51-102.
[192] D. Blavette, E. Cadel, C. Pareige, B. Deconihout, and P. Caron, "Phase Transformation and Segregation to Lattice Defects in Ni-Base Superalloys," *Microscopy and Microanalysis*, vol. 13, no. 6, pp. 464-483, 2007, doi: 10.1017/S143192760707078X.
[193] V. C. I. Strutt, B. M. Jenkins, J. M. Woolrich, M. Appleton, M. P. Moody, and P. A. J. Bagot, "Effect of microsegregation and heat treatment on localised γ and γ' compositions in single crystal Ni-based superalloys," *Journal of Alloys and Compounds*, vol. 949, 2023, doi: 10.1016/j.jallcom.2023.169861.
[194] A. S. Ebner *et al.*, "Grain boundary segregation in Ni-base alloys: A combined atom probe tomography and first principles study," *Acta Materialia*, vol. 221, 2021, doi: 10.1016/j.actamat.2021.117354.
[195] L. Wang, N. Wang, and N. Provatas, "Liquid channel segregation and morphology and their relation with hot cracking susceptibility during columnar growth in binary alloys," *Acta Materialia*, vol. 126, pp. 302-312, 2017/03/01/ 2017, doi: https://doi.org/10.1016/j.actamat.2016.11.058.
[196] A. Gupta, X. Zhou, G. B. Thompson, and G. J. Tucker, "Role of grain boundary character and its evolution on interfacial solute segregation behavior in nanocrystalline Ni-P," *Acta Materialia*, vol. 190, pp. 113-123, 2020/05/15/ 2020, doi: https://doi.org/10.1016/j.actamat.2020.03.012.
[197] P. Lejček, "Effect of Variables on Equilibrium Grain Boundary Segregation," in *Grain Boundary Segregation in Metals*, P. Lejcek Ed. Berlin, Heidelberg: Springer Berlin Heidelberg, 2010, pp. 103-152.
[198] F. Wang, D. Ma, and A. Bührig-Polaczek, "Preferred growth orientation and microsegregation behaviors of eutectic in a nickel-based single-crystal superalloy," *Sci Technol Adv Mat*, vol. 16, no. 2, p. 025004, 2015/04/28 2015, doi: 10.1088/1468-6996/16/2/025004.
[199] D. Ma and U. Grafe, "Microsegregation in directionally solidified dendritic-cellular structure of superalloy CMSX-4," *Materials Science and Engineering: A*, vol. 270, no. 2, pp. 339-342, 1999/09/30/ 1999, doi: https://doi.org/10.1016/S0921-5093(99)00208-7.
[200] X. Zhao, L. Liu, W. Zhang, G. Liu, J. Zhang, and H. Fu, "Segregation behavior of alloying elements in different oriented single crystal nickel based superalloys," *Materials Letters*, vol. 63, no. 30, pp. 2635-2638, 2009/12/31/ 2009, doi: https://doi.org/10.1016/j.matlet.2009.09.035.
[201] R. Yong-Hua, G. Yong-Xiang, and H. G. Xiang, "Characterization of M23C6 carbide precipitated at grain boundaries in a superalloy," *Metallography*, vol. 22, no. 1, pp. 47-55, 1989/01/01/ 1989, doi: https://doi.org/10.1016/0026-0800(89)90021-9.
[202] L. Letellier, S. Chambreland, P. Duval, and D. Blavette, "Grain boundary segregation in nickel base superalloys Astroloy: an atom-probe study," *Applied Surface Science*, vol. 67, no. 1, pp. 305-310, 1993/04/02/ 1993, doi: https://doi.org/10.1016/0169-4332(93)90330-E.
[203] B. Guo *et al.*, "Cracking mechanism of Hastelloy X superalloy during directed energy deposition additive manufacturing," *Additive Manufacturing*, vol. 55, p. 102792, 2022/07/01/ 2022, doi: https://doi.org/10.1016/j.addma.2022.102792.
[204] F. Theska *et al.*, "Review of Microstructure–Mechanical Property Relationships in Cast and Wrought Ni-Based Superalloys with Boron, Carbon, and Zirconium Microalloying Additions," *Advanced Engineering Materials*, vol. 25, no. 8, 2022, doi: 10.1002/adem.202201514.
[205] L. R. Liu, T. Jin, N. R. Zhao, X. F. Sun, H. R. Guan, and Z. Q. Hu, "Formation of carbides and their effects on stress rupture of a Ni-base single crystal superalloy," *Materials Science and Engineering: A*, vol. 361, no. 1, pp. 191-197, 2003/11/25/ 2003, doi: https://doi.org/10.1016/S0921-5093(03)00517-3.

Appendix A

Alloy	Manufacturing Process	Type of phenomena and secondary phases precipitate found	Type of interface	Analytical Method		Main findings	Source
				Method	Assessment		
Hastelloy X	Rolled + Annealed @1175 °C	M_6C (Mo-rich) $M_{23}C_6$ (Cr-rich)	GB	XRD TEM OM	The lattice parameter, composition Dislocations, carbide-matrix relationship Microstructure	Investigation into the impact of different long-term ageing at different temperatures. Evolution of carbides and ς-phase and μ-phase. Detriment to mechanical properties. Primary carbides, $\{1\ 0\ 0\}_{precipitate}$ // $\{1\ 0\ 0\}_{matrix}$; $\langle 1\ 0\ 0\rangle_{precipitate}$ //$\langle 1\ 0\ 0\rangle_{matrix}$[3]	H. M. Tawancy [106]
Ni-20Cr-2.STi-0.8AI-0.050-0.6B	Rolled + ST + Aged	$M_{23}C_6$	GB	HR-TEM	Orientation relationship Structure	$M_{23}C_6$ carbides are nucleated separately on both sides of the grain boundaries. Carbides have a coherency with the matrix, and grow to the opposite grain. $\{1\ 0\ 0\}_{M23C6}$ //$\{1\ 0\ 0\}_{\gamma}$; $(1\ 0\ 0)_{M23C6}$ //$(1\ 0\ 0)_{\gamma}$	R. Yong-Hua et al. [201]
Astrology	Powder metallurgy	Segregation at GB	Serrated GB	TEM AP	GB morphology (HAADF) GB vicinities composition.	GB geometry upon segregation effects, and GB geometry in the function of HT. Mo enrichment was observed with localized depletion of Ni and Co, in γ /γ interfaces.	L. Letellier et al. [202]
Alloy 690TT	Extrusion	$M_{23}C_6$ (Cr-rich)	CSL LAGB HAGB	SEM TEM	GB character, carbide morphology, density, and distribution (SAED) OR between carbide and matrix	Intergranular chromium carbides are retarded on the LAGB while coarse and discrete $M_{23}C_6$ carbides were mainly found in random HAGB. Density and distribution on GB could have a particular OR and GB structure. In this work was found a cube-cube OR $\{100\}_{M_{23}C_6} \parallel \{100\}_{\gamma}$; $\langle 100\rangle_{M_{23}C_6} \parallel \langle 100\rangle_{\gamma}$.	Y. S. Lim et al. [142]
Ni–Cr–Co-W	Casting directional solidification	MC (Ti, Ta-rich) M6C (Cr, Mo, W-rich)	Interdendritic	SEM EDS TEM	Microstructure, directional coarsening., carbides morphology. Elemental analysis Carbides/matrix OR, dislocations	Identifies two types of carbides $(M_6C)_2$ precipitated and $(M_6C)_1$ decomposed from a MC, (t > 871 °C), the latter is detrimental to the system, as it has an irregular OR with the matrix, and bonding the force is weak.$\{1\ 0\ 0\}_{(M6C)2}$ // $\{1\ 0\ 0\}_{matrix}$, $\langle 1\ 0\ 0\rangle_{(M6C)2}$ // $\langle 1\ 0\ 0\rangle_{matrix}$; $\{0\ 0\ 1\}_{M23C6}$ // $\{0\ 0\ 1\}_{matrix}$, $\langle 0\ 0\ 1\rangle_{M23C6}$ // $\langle 0\ 0\ 1\rangle_{matrix}$	L. R. Liu et al. [205]
Waspaloy	Powder extrusion	N/S	Serrated	SEM	GB identification	Influence of GB morphology, modified by different HT, on creep resistance,	A. Wisniewski [189]
Nimonic 263	Hot rolled-WQ	$M_{23}C_6$ at GB	Serrated GB	SEM HR-TEM	Morphology and GB identification Crystallographic analysis	GB serrations affect different aspects of the $M_{23}C_6$ carbides, such as morphology. After the serration occurred, carbides precipitated and grew along the serrated GB. After the serration occurred, carbides precipitated and grew along the serrated GB	H.U. Hong et al. [174]
SRR99	Casting (Seeding technique)	GB character MC (Ti, Ta-rich) at GB M_6C (W-rich) at GB $M_{23}C_6$ (Cr-rich) at GB	4° 8° 13°	SEM TEM S-TEM XRD	(EBSD) GB misorientation angle. (HAADF) Microstructure Z-contrast, OR Microstructure of the sample Lattice parameters	Evolution of carbides through different HT, correlates misorientation angle with carbide-type formation, based on the relationship of the different types of carbides with the γ/γ' matrix, also attributes M_6C and $M_{23}C_6$ carbides formation to concentrations of different rations of Cr/W caused by MC carbides.	X. Dong et al. [21]

[3] Assumed M_6C and $M_{23}C_6$ have same oreintation relationship, but they clarify that these are features of $M_{23}C_6$ carbides

Ni–Cr–W superalloy	Wrought	$M_{23}C_6$ (Cr-rich) at GB	Serrated CSL LAGB HAGB	SEM	GB and carbides identification (EBSD) GB misorientation angle/plane	Observed dependence in the formation of GB serration shape, accompanied by intergranular $M_{23}C_6$ carbides. A higher fraction of $M_{23}C_6$ carbides appearance is confined in the range of angle misorientation from 20° to 40°	B. Tang et al. [172]
Ni–Cr–W superalloy	Forge and hot rolled	M_6C (W-rich) at bulk and GB $M_{23}C_6$ (Cr-rich) at bulk and GB	LAGB HAGB CSL	SEM SEM TEM	(EBSD) types and distribution of GBs, crystallographic orientation morphology characteristics of GB carbides (EDS) elements segregation at GBs (SAED)	During GB segregation progress, $M_{23}C_6$, carbides nucleate with one of the adjacent grains with a coherent OR $(1\ 1\ 1)_{M_{23}C_6} \parallel (1\ 1\ 1)_{matrix}$; $[0\ 1\ 1]_{M_{23}C_6} \parallel [0\ 1\ 1]_{matrix}$ to minimize the activation energy for nucleation. There is a clear tendency of $M_{23}C_6$ carbides to grow towards the incoherent grain, where there is no OR between crystal lattices carbide	R. Dong [176]
Hastelloy X	Cast, rolled, and thermomechanical treated	Control of precipitation μ phase ($Fe_{7.9}Mo_{5.1}$) Hex M_6C (Mo-rich)	RGB CSL Σ3 and Σ9	SEM SEM TEM XRD	(EBSD) GB misorientation angle. Microstructure (SEDP) carbide morphology The lattice parameter, composition	M_6C carbides strengthen the matrix, and the harmful particle is μ phase, both show a dependence on GB misorientation, being RGB more prone to develop μ phase, but in the vicinity of CSL Σ3. Mo prefers to segregate to RGB through CSL Σ3 boundaries. Small M_6C carbides were detected at CSL Σ3 boundaries	X. Wang et al. [58]
Hastelloy X	LPBF	Cracking M_6C (Mo-rich) at GB $M_{12}C$ (Mo-rich) at GB M_nC_m (Mo-rich) at GB	N/A	FE-SEM SEM SEM XRD	BSE Melt pools, cells, and carbides Melt pools and carbides EDS Line scan profiles Carbides stoichiometry and lattice parameters (Anodically extracted).	Intergranular Mo-rich carbides provided weaker zones and combined with high thermal residual stresses resulted in hot cracks along the GBs and cell boundaries.	Marchese et al. [107]
Hastelloy X	SLM		Sub-GB < 2°	SEM TEM SEM	(EBSD) GB misorientation angle, texture. (HAADF) Microstructure Z-contrast, OR EDS element colored map	The study is centered on hierarchical structure rather than on carbides located at GB, it only states some highlights related to sub-grain boundaries. 50–100 nm large precipitates enriched in Cr, Al, Ti, Mo, Si, and O, are located within the cell boundaries in the case of the AB sample.	S. Pourbabak et al. [47]
Haynes 282	Sheet	MC (Mo, Ti) at GB M_6C (Mo-rich) at GB $M_{23}C_6$ (Cr-rich) at GB	Serrated GB	SEM SEM	GB Morphology EDS element colored map	The kinetics of $M_{23}C_6$ was significantly faster than that of M_6C, under different HTs. Carbide morphology changes due to different HTs. Small M_6C carbides can be explained by the smaller time steps, which allow more precise identification of the onset of precipitation.	C. Joseph et al. [175]